Title
Computational Investigation of Nanoporous Materials for Clean Energy Applications

Author
Deeg, Kathryn Suzanne

Publication Date
2019

Computational Investigation of Nanoporous Materials for Clean Energy Applications

by

Kathryn S. Deeg

A dissertation submitted in partial satisfaction of the

requirements for the degree of

Doctor of Philosophy

in

Chemistry

in the

Graduate Division

of the

University of California, Berkeley

Committee in charge:

Professor Berend Smit, Chair
Professor Martin Head-Gordon
Professor Stephen Leone
Professor Jeffrey Neaton

Summer 2019

Computational Investigation of Nanoporous Materials for Clean Energy Applications

Abstract

Computational Investigation of Nanoporous Materials for Clean Energy Applications

by

Kathryn S. Deeg

Doctor of Philosophy in Chemistry

University of California, Berkeley

Professor Berend Smit, Chair

Nanoporous materials such as metal-organic frameworks (MOFs) are promising for applications in clean energy thanks to their diverse and extraordinary gas adsorption properties. Additionally, these materials' high degree of tunability means that nearly infinite distinct materials can be envisioned with different combinations of compositions, topologies, and surface properties. Each combination could yield a material with its own unique gas adsorption phenomena and resulting real-world applications. While many materials with outstanding properties have been studied, it remains a challenge to find or design an optimal material for a given application and to understand the complex molecular-level interactions that give rise to macroscopic behavior.

In this dissertation, we take three different computational approaches towards advancing the discovery and understanding of nanoporous materials for various clean energy applications.

In Chapters 2 and 3, we screen large databases of materials for carbon capture and hydrogen storage, using molecular simulations. We develop accurate atomistic models for the relevant adsorption phenomena and identify appropriate criteria for predicting performance. In this way, we identify optimal materials for carbon capture and hydrogen storage, as well as characteristics common among top performers. Ultimately, such findings can help guide the design of optimal materials for these applications.

In Chapter 4, we study in depth a novel biporous MOF for natural gas processing, using molecular simulations in conjunction with experiments. This MOF's rare feature of biporosity, or coexistence of two chemically distinct pores within the same MOF, gives rise to unique stepwise activation that can be controlled to consequently tune the MOF's CO_2/CH_4 separation performance. This phenomenon is explained in terms of CO_2's and CH_4's differing interactions with the pore surfaces. In this way, we contribute to the understanding of complex behavior in biporous materials that affects their gas separation performance.

Finally, in Chapter 5, we investigate the assembly process of MOFs using a statistical mechanical lattice model. In particular, we map out the thermodynamic assembly pathway of MOF-74 and explore the effect of surface tension energies on the shapes of nucleating

clusters. With this study we work towards understanding the assembly pathway of MOFs with the ultimate goal of being able to control the synthesis process and obtain crystals of the desired morphology.

Contents

Acknowledgments

I am deeply grateful for everyone who supported me during my PhD. I would first like to thank my advisors, Berend Smit and Steve Whitelam, for their expert research guidance, for encouraging me to pursue my interests, and for sticking with me for the entirety of my PhD.

I have also been fortunate to work with wonderful labmates. To my Berkeley labmates Bess Vlaisavljevich, Cory Simon, Efrem Braun, Greg Mann, Johanna Huck, Kaili Ordiz, Kyuho Lee, Lennart Joos, Li-Chiang Lin, Matt Witman, Michelle Liu, Nakul Rampal, Rocio Mercado, Shachi Katira, Sondre Schnell, and Sudi Jawahery; LBL labmates Anthony Frachioni, John Edison, Joyjit Kundu, Katie Klymko, Ranjan Mannige, Tom Haxton, and Zdenek Preisler; and EPFL labmates Aliaksandr Yakutovich, Amber Mace, Andrés Ortega Guerrero, Andrzej Gładysiak, Daiane Damasceno Borges, Daniele Ongari, Davide Tiana, Gloria Capano, Henglu Xu, Kyriakos Stylianou, Leopold Talirz, Mohamad Moosavi, Olga Syzgantseva, Özge Kadioglu, Peter Boyd, Senja Barthel, Yongjin Lee, and Zhi Li: thank you all for quality scientific discussions, generosity with your time, and your camaraderie. The supportive community you've helped create has been important in making it possible for me to do my best work, and I hope I've helped you do the same. Special thanks to Daiane for helping me to grow as an independent researcher; to Kyriakos and Andrzej for a rewarding long-term, interdisciplinary collaboration; and to Michelle, Rocio, and Sudi for being some of the best friends I could ask for.

I am also grateful for my fellow Berkeley Chemistry PhD friends who have gone through this marathon with me: Andreana Rosnik, Ashley Truxal, Erika Warrick, Josh Laughner, Katherine Evans, Meghan Hauser, Pratima Satish, and Sumana Raj. Thank you for working together on problem sets for hours on end, checking in continually, and helping navigate grad school. I would also like to extend thanks to Marjorie Went for being a kind listener and helping me build the confidence to finish my PhD strong.

Thank you also to the team of people who provided the administrative support during my PhD that made possible all the computer usage, all the travel between Berkeley and Switzerland, and everything else "under the hood": Cezar Ramiro, Constance Visser Witman, Evelyn Ludi, Kelley McDonald, Kim Eastman, Kristin Stangl, Laure Dayer, and Lynn Keithlin.

My work would not have been possible without generous funding from the National Science Foundation Graduate Research Fellowship Program under Grant No. DGE 1106400 and from the Center for Gas Separations Relevant to Clean Energy Technologies, an Energy Frontier Research Center funded by the U.S. Department of Energy, Office of Science, Basic Energy Sciences, under Award No. DE-SC0001015.

Finally, I owe special thanks to the big network of people I'm lucky to call family and friends. To Nora, Riz, Carl, Lily, Nicole, Jen, Devney, and everyone else I can't possibly list all of here: thank you all for your encouragement and patience during my PhD. In particular, thank you to my parents, Mark and Susan, for having always instilled in me the conviction that I could achieve anything I set my mind to, and to my husband Ricardo not only for his unconditional support, but also for pushing me to do my best.

Chapter 1

Introduction

1.1 Nanoporous materials

Nanoporous materials are a diverse class of crystalline solids that have received much recent interest for their potential applications in gas storage and separation, among other uses [1, 2]. These materials' strong performance in these areas stems from their accessible pores, high internal surface area, and structural stability. In this study, we consider materials with pore sizes of similar magnitude to the size of gas molecules that can be adsorbed. In such materials, gas molecules interact with the internal pore surface, with thermodynamic properties depending strongly on the pore topology and composition [3]. This phenomenon directly influences these materials' varied uses in gas storage and gas separations, the applications upon which this work focuses.

Major classes of nanoporous materials considered in this work include zeolites, covalent-organic frameworks (COFs), and metal-organic frameworks (MOFs), which are constructed from inorganic building units, organic building units, or a mix of the two, respectively.

Zeolites

Zeolites are aluminosilicate frameworks composed of TO_4 tetrahedra (T is usually Si or Al, with more Si than Al) as primary building units (Figure 1.1). The charge imbalance caused by each framework Al atom is balanced by a non-framework cation, usually K, Na, or Ca, or, less frequently, Li, Mg, Sr, or Ba [4]. Zeolites occur commonly in nature, with about 40 different types identified. Natural zeolites are used on a large scale worldwide for low-value applications including in construction materials and animal feed [5]. The first synthetic zeolites were developed beginning around 1950 for use as catalysts in fluid catalytic cracking of heavy petroleum distillates [6], taking advantage of zeolites' high chemical and thermal stabilities. Today, synthetic zeolites are widely used as catalysts in the petrochemical industry and also as water softeners, representing a global market of \$350 billion per year [7]. Zeolites' molecular-sized pores and range of pore topologies also make them promising for gas separations based on molecule size and polarity [8]. As a result, zeolites have been studied more recently for gas separations and storage [3, 9, 10].

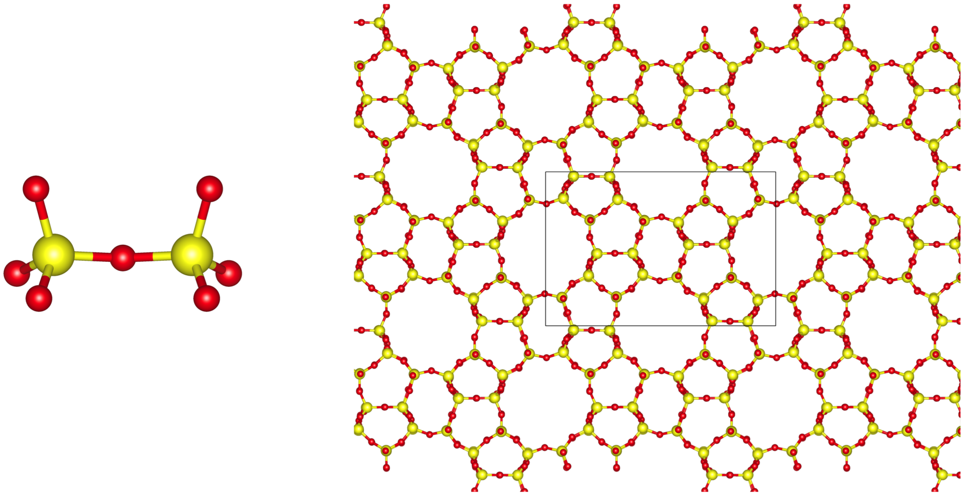

Figure 1.1: One of the most-studied zeolites is MFI, also known as ZSM-5 [8]. The all-silica version of MFI, called silicalite, is shown here, along with example SiO_4 tetrahedra that make up the structure. The black lines on the crystal structure indicate the unit cell, which has dimensions 20.022 Å × 13.383 Å in the plane shown. Color scheme: Si: yellow; O: red.

Metal-organic frameworks

Metal-organic frameworks (MOFs) are a diverse class of nanoporous materials characterized by remarkably high porosity (up to 90% free volume) and internal surface areas (up to 10,000 m^2/g) [1, 11]. In comparison, other porous materials such as zeolites and carbons have internal surface areas generally up to 1,000 m^2/g. MOFs form from the self-assembly of metal centers and organic linkers [12] (Figure 1.2). Because a tremendous number of metals and organic molecules can serve as the metal centers and linkers, a nearly limitless variety of structures can be formed. Furthermore, thanks to the modular nature of MOFs, their structure, composition, and functionality can be tuned, and, in principle, tailor-made for a given application [13].

MOFs were first developed in the 1990s; since then, the scope of research on MOFs and number of MOFs reported in the literature has grown enormously [1]. Their high porosity and internal surface areas and adjustable functionality and internal surface properties have led to extensive study of their potential applications in, for example, methane and hydrogen storage [15, 16], carbon dioxide capture [17], and numerous other gas separations [18, 19]. In the 2010s, the first MOFs became commercially available for gas separations including carbon dioxide capture from power plant emissions and ethylene capture for delaying fruit ripening [20, 21].

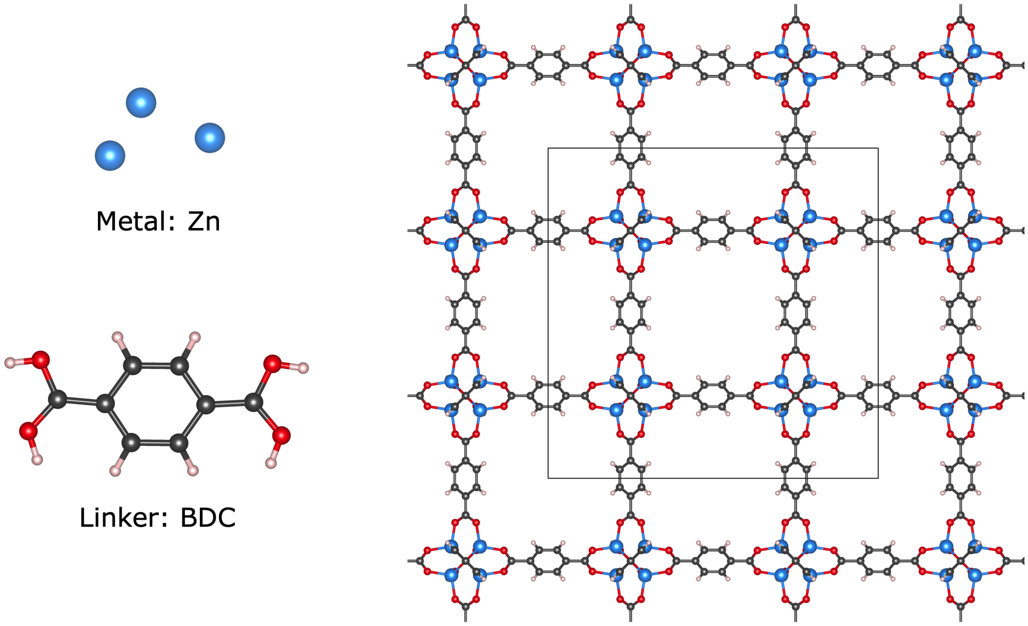

Figure 1.2: MOFs are composed of metal centers and organic linkers. For example, in MOF-5, also known as IRMOF-1 ($Zn_4O(BDC)_3$, BDC = 1,4-benzenedicarboxylate), the metal centers consist of zinc atoms, and the linkers are benzene dicarboxylate ions, which self assemble into a crystalline cubic structure [14]. The black lines on the crystal structure indicate the unit cell, which has dimensions 25.832 Å × 25.832 Å in the plane shown. Color scheme: C: gray; H: white; O: red; Zn: blue.

One subclass of MOFs is zeolitic imidazole frameworks (ZIFs). ZIFs are composed of M-Im-M bonds (M is Zn or Co, and Im is imidazolate), which form an angle of 145°, coinciding with the preferred Si-O-Si angle in zeolites [2]. Consequently, ZIFs possess zeolite-like topologies but MOF-like compositions and can combine advantages of both classes of materials. As a result, many ZIFs exhibit ultrahigh surface areas and extensive functionalities as well as exceptionally high thermal and chemical stabilities; they are therefore especially promising for applications in catalysis, gas separations, and sensing [22].

Covalent-organic frameworks

Covalent-organic frameworks (COFs) are composed solely of light elements, such as hydrogen, carbon, nitrogen, and oxygen, that are linked by strong covalent bonds (Figure 1.3). COFs' features include low densities, large internal surface areas, high thermal stabilities, permanent porosity, and regular pore structures [23, 24], making them promising for a range of gas separation and storage applications [25–27]. Similar to MOFs, COFs' modular nature allows tunability when synthesizing a material for a given application. In contrast with MOFs, however, COFs are relatively lightweight, since COFs contain no metals and only light elements. The design pathways developed for MOFs paved the way for COF synthesis, with the first COFs reported in 2005 [28].

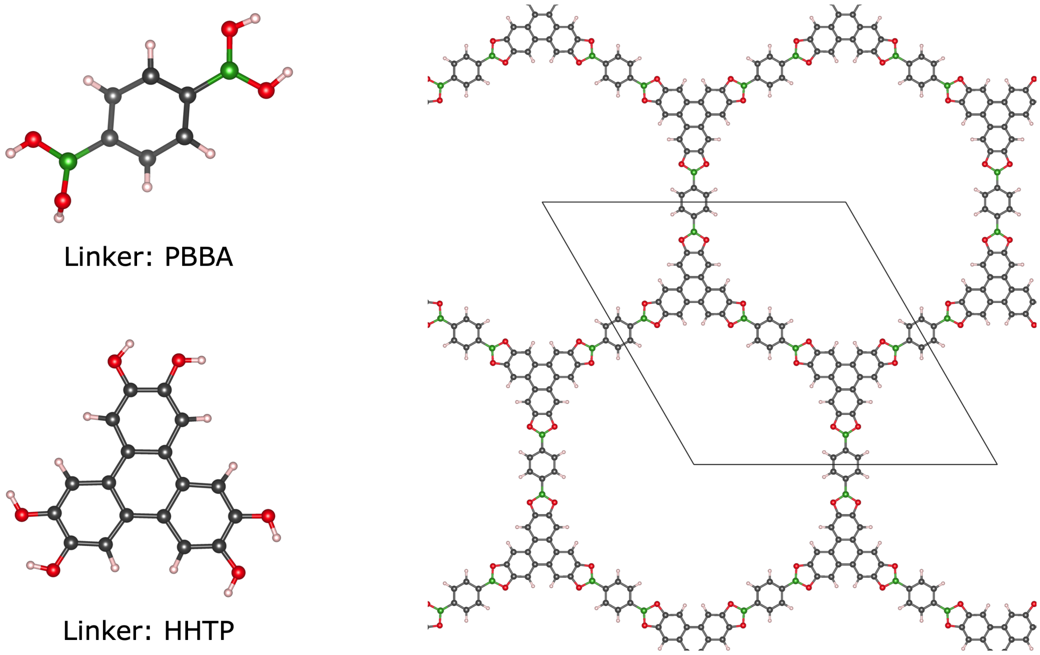

Figure 1.3: COFs are composed of organic molecules joined by covalent bonds. For example, COF-5 ($C_9H_4BO_2$) is made from 1,4-phenylenebis(boronic acid) (PBBA) and 2,3,6,7,10,11-hexahydroxytriphenylene (HHTP) molecules [28]. The black lines on the crystal structure indicate the unit cell, which has dimensions 30.0198 Å × 30.0198 Å in the plane shown. Color scheme: C: gray; H: white; O: red; B: green.

1.2 Clean energy applications of nanoporous materials

Physisorption of gas molecules is the underlying physical mechanism of the applications investigated in this study. All applications investigated within are directly related to clean energy.

Carbon capture

Carbon capture and sequestration (CCS) is a climate change mitigation technology that involves 1) capture of carbon dioxide (CO_2) from emissions from major stationary point sources, such as fossil fuel power plants and industrial facilities, 2) transportation of the CO_2 to a storage site, and 3) long-term storage of the CO_2 [29]. CCS will be necessary to achieve global warming targets, decarbonize energy-intensive industrial processes that cannot be electrified, and establish a low-carbon energy system [30]. Indeed, most projected greenhouse gas emission pathways that limit the increase in global average temperature to 1.5 °C above pre-industrial levels include CCS [31]. Limiting global warming to 1.5 °C compared to 2.0 °C or greater will significantly reduce the risks and impacts of climate change, especially those associated with long-lasting or irreversible changes to ecosystems and human health and well-being [31]. For these reasons, CCS will likely play a key role in climate change mitigation.

However, levels of CCS deployment remain low in comparison with those indicated necessary for meeting global warming targets established by the Intergovernmental Panel on Climate Change (IPCC) [32]. As of 2018, there were 23 large-scale CCS facilities in operation or under construction globally, capturing around 0.04 Gt (40 million tonnes) of CO_2 per year [33]. In contrast, CCS will need to capture on the order of 10 Gt of CO_2 per year by mid-21st century under IPCC projections [33]. This amounts to about 27% of the approximately 37 Gt of CO_2 emitted from human activities annually as of 2018 [34].

Increased deployment of CCS is limited largely due to its costs [35]. Within the CCS process, CO_2 capture requires the most energy and is responsible for at least 70% of the total costs [36]. In a power plant, CO_2 capture uses 25% to 40% of the total energy produced at the plant [36]. Of post-combustion capture processes, which can be applied to already-constructed plants, the dominant and most mature technology is currently amine scrubbing. In this process, CO_2 is selectively absorbed from flue gas into an aqueous solution of amine. The CO_2-enriched solution is heated using steam from the power plant, thereby regenerating the amine and leaving high-purity CO_2 to be subsequently compressed, transported, and stored [37]. The high energy penalty imposed by amine scrubbing is due in large part to the heat required for regenerating the amine solution. Of the various amines that can serve as chemical absorbents in amine scrubbing, monoethanolamine (MEA) is widely used and serves as the benchmark amine for CO_2 capture at power plants [30].

In order to reduce the costs of CCS and consequently facilitate implementation on a larger scale, it is therefore logical to focus research efforts on developing more-efficient CO_2 capture technologies. Post-combustion capture technologies alternative to MEA, each under various stages of development, include improved solvent-based chemisorption [30] (novel single amine absorbents, amine blends, multi-phase absorbents, and water-lean or nonaqueous solvents including ionic liquids [38]), calcium looping technology [39], membrane processes [40], and physical adsorption processes [41, 42].

In particular, physical adsorption processes are advantageous since the sorbent is regenerated by a moderate temperature or pressure swing, resulting in reduced energy costs compared to absorption processes [43]. Furthermore, physical adsorption is potentially more environmentally friendly than amine-based solvents, which can decompose to form toxic byproducts [36]. Research has focused on developing adsorbents with improved CO_2 selectivity and adsorption capacity, adequate mechanical and thermal stability, and low energy requirement to regenerate adsorbed CO_2 [44, 45].

In Chapter 2, we investigate covalent-organic frameworks as high-capacity adsorbents for carbon capture.

Hydrogen storage

Hydrogen is an alternative fuel that, if widely deployed, could help decarbonize electricity generation, heating, and transportation. If produced by electrolysis with renewable energy sources, hydrogen used as a fuel generates no carbon emissions. Highly abundant on Earth as an element, hydrogen could help address both the world's increasing energy demand, projected to grow 27% between 2017 and 2040 [46], and the need to reduce emissions from fossil fuel combustion in order to meet global climate targets. Hydrogen can be used to power fuel cells in electric vehicles. Fuel cell electric vehicles (FCEVs) are attractive because their only emission is water, they are highly efficient compared with internal combustion engines, and they refuel more quickly than current battery electric vehicles [47].

Although the availability of commercial FCEVs has increased in the last decade [48], and more hydrogen refuelling stations are being constructed [49], FCEVs remain a small fraction of total electric vehicle sales [47]. A major obstacle in increased deployment of FCEVs is affordable, safe on-board hydrogen storage with efficient, reversible hydrogen uptake and release. Hydrogen is a gas under ambient conditions and has a much lower volumetric energy density compared with liquid fuels such as gasoline [50]. The most commonly used storage method is gaseous hydrogen compressed to pressures up to about 10,000 psi (700 bar), but technological advances are still needed to achieve tanks with low enough volume and weight to achieve a conventional driving range (>300 miles) at a competitive cost [51, 52]. Another conventional method is to store liquefied hydrogen. Liquefaction requires cooling to -253 °C and is energy- and time-consuming [53]. A third method, cryogenic-compressed hydrogen storage, involves compressing hydrogen gas to moderate pressures and cooling to cryogenic temperatures. This method reduces boil-off of hydrogen while achieving a high energy density [53].

A promising strategy under current investigation is storage of hydrogen in nanoporous materials. Under certain temperature and pressure regimes, a tank filled with such a material can have greater capacity than an empty tank [54].

In Chapter 3, we screen a large, diverse library of nanoporous materials for room-temperature and cryogenic-compressed hydrogen storage.

Natural gas processing

Natural gas processing is one of the most important gas separation processes worldwide. As of 2017, over 3.7 trillion cubic meters of natural gas, or 22% of total global energy use [55], were consumed every year [56]. Furthermore, the natural gas market continues to grow and is projected to surpass 4 trillion cubic meters by 2022 [57]. All raw natural gas must be processed before use in order to remove impurities, which can include CO_2, H_2S, water, and a range of hydrocarbons. In natural gas processing, these impurities are removed in order to meet standards for transmission pipelines and consumer consumption.

One of the most common impurities present in unprocessed natural gas is CO_2. Pipeline specifications typically require a natural gas composition of no more than 2 to 4 mol% CO_2, depending on the country [58]. In the U.S., currently the world's top producer of natural gas, over 25% of natural gas fields contain over 1 mol% of CO_2 [59], and an important number of natural gas fields contain 10 mol% or more of CO_2 [60]. Meanwhile, biogas, a renewable energy source composed of a mixture of methane and other gases generated from the anaerobic digestion of organic matter, typically contains 30-40% CO_2, depending on the biogas source [61]. In these concentrations, CO_2 is corrosive to pipelines and decreases the gas's heating value [62]. Its removal is therefore essential in optimizing the value of the natural gas.

The most common method currently used to remove CO_2 during natural gas processing is amine scrubbing or amine washing. In this process, CO_2 is absorbed by a solution of amine compounds. Amines used commercially include monoethanolamine (MEA), diethanolamine (DEA), triethanolamine (TEA), methyl diethanolamine (MDEA), di-isopropanolamine (DIPA), and diglycolamine (DGA) [60]. However, amine-based absorption is energetically costly, as high temperatures are required to desorb CO_2 from the CO_2-rich liquid amine [60]. Furthermore, the solvent causes corrosion of the plant units; amine degradation and foaming reduce the efficiency of the CO_2 separation [63]. Another methods, cryogenic separation, where the gas mixture is cooled to below the boiling point of CO_2 and the liquid CO_2 is extracted, is used commercially to remove CO_2 from natural gas streams with very high CO_2 concentrations (50-70%). However, this technique is not economically viable for streams with lower concentrations of CO_2 [63]. Finally, membrane processes separate CO_2 from the other gases based on the gases' different permeabilities through a thin film. Polymeric membranes are commercially available for CO_2 separations in natural gas processing, and research into membrane selectivity and durability continues to improve membrane separation technology [63], already more economical than amine scrubbing in certain situations [62]. Yet there remain important challenges in membrane processes, including high replacement costs, susceptibility to fouling from contaminants, and methane loss [58].

Given the scale on which CO_2 is separated from natural gas, and given the energetic costs associated with current separation methods, there is significant potential for energy savings by developing new or improved separation processes [60]. An alternative separation process is physical adsorption, such as on molecular sieves or activated carbon. The interaction between CO_2 and the adsorbent is weaker than that between CO_2 and an amine solution, so less energy is required to regenerate the sorbent [63]. Metal-organic frameworks (MOFs), in particular, show promise as efficient adsorbents for CO_2 separation in natural gas purification. Their large surface areas and high CO_2 uptake contribute to their strong separation performance, and their adjustable pore sizes and tunable pore surface properties facilitate the rational design of a MOF for a given application [64]. MOFs have been well studied at the laboratory level for CO_2 separation from natural gas and biogas, and several show potential for successful application at scale [64–66].

In Chapter 4, we investigate in detail a novel MOF for CO_2/CH_4 separation. We consider this as a clean energy application because our study aims to develop pathways for more-efficient natural gas purification, thereby increasing energy efficiency of this large-scale industrial separation process.

1.3 Simulation methods

Models

Atomistic models for molecular simulations

We use atomistic models for studying gas adsorption via molecular simulations. Frameworks are modeled atomistically in crystallographic detail, as all materials considered in this dissertation are crystalline. Crystal structures of frameworks that have been synthesized experimentally can be determined from diffraction experiments, and these structures can be further relaxed to a minimum-energy state using density functional theory (DFT). Some frameworks considered in this dissertation are hypothetical frameworks generated in silico by combining known building units. In all cases, we consider frameworks to be rigid, which has been shown to be a good approximation in many cases, but may introduce artifacts in some cases; some materials are known to expand and contract with gas adsorption, which can affect gas uptake or separation selectivity [67, 68]. Guest molecules are modeled atomistically, in the case of CO_2 and N_2, or as a single united-atom particle, in the case of H_2 and CH_4. Periodic boundary conditions [69] are used in order to mimic an extended crystalline material and to avoid finite size effects.

The energy of the system is taken as the sum of non-bonded pairwise framework-guest and guest-guest interactions. Each interaction is computed as the sum of the Lennard-Jones 12-6 potential, representing dispersive interactions, and Coulomb's law, representing electrostatic interactions:

$$U_{\text{system}} = \sum_{i,j} (U_{ij,\,\text{LJ}} + U_{ij,\,\text{Coul}}), \tag{1.1}$$

where the sum is over all pairs of nonbonded atoms i and j, and pairwise interactions are given by

$$U_{ij,\,\text{LJ}} = 4\epsilon_{ij}\left[\left(\frac{\sigma_{ij}}{r_{ij}}\right)^{12} - \left(\frac{\sigma_{ij}}{r_{ij}}\right)^{6}\right] \text{ and} \tag{1.2}$$

$$U_{ij,\,\text{Coul}} = \frac{q_i q_j}{4\pi\varepsilon_0 r_{ij}^2}, \tag{1.3}$$

where r_{ij} is the distance between atoms i and j; q_i is the atomic charge of atom i; and ε_0 is the permittivity of free space. ϵ and σ are the two Lennard-Jones parameters that can be interpreted as interaction strength and effective particle size, respectively (Figure 1.4).

The Lennard-Jones potential goes to zero relatively quickly with distance, so Lennard-Jones interactions are truncated at 12-13 Å, and the potential is shifted such that it equals

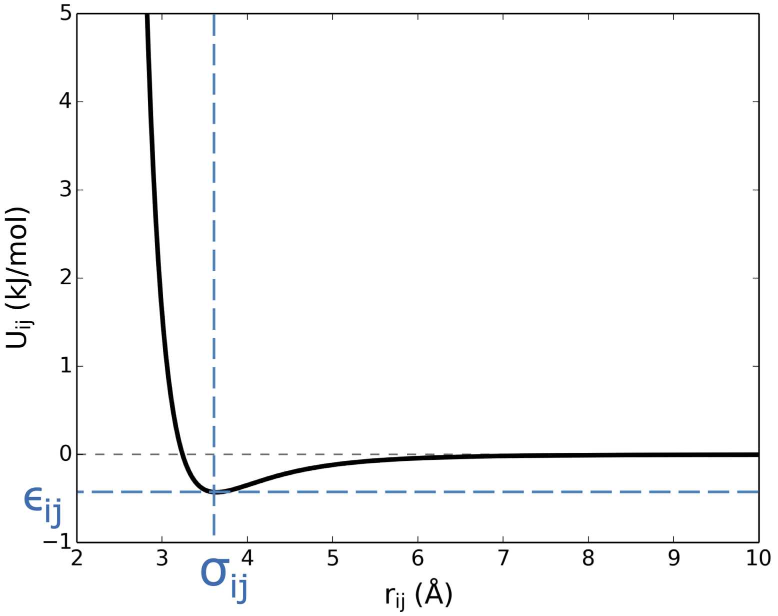

Figure 1.4: Lennard-Jones potential U_{ij}; in this graph, atoms i and j are O of CO_2 and C of a MOF, using previously reported Lennard-Jones parameters. ϵ_{ij} is the minimum value of $U_{ij}(r_{ij})$, and σ_{ij} is the distance at which $U_{ij}(r_{ij})$ is minimized.

0 at the cutoff distance. Meanwhile, to adequately treat the longer-range Coulombic interactions, Ewald summations are used [70, 71].

While a range of interatomic potentials have been developed of varying complexities and applicabilities, the Lennard-Jones potential provides a reasonable or, often, very good description of adsorption properties. Furthermore, it is probably the most commonly used interatomic potential in molecular simulation studies of nanoporous materials, and excellent parameters for many various systems have been developed.

Lennard-Jones parameters ϵ and σ can be developed by fitting to experimental bulk data in the case of guest-guest interactions [72, 73], to experimental adsorption data in the case of guest-host interactions [74, 75], or to ab initio calculations [76, 77]. Several general, transferrable parameter sets have been developed that describe a wide range of adsorbates and framework atoms, such as the Universal Force Field (UFF) [78], DREIDING [79], and TraPPE [80]. In the work herein, we utilize both general parameter sets as well as parameters developed for specific systems, all previously published.

Meanwhile, to calculate electrostatic interactions using Coulomb's law, framework atom point partial charges are needed. They can be developed most accurately by using wave function or DFT methods to compute the electronic density and electrostatic potential and subsequently deriving partial charges from the electronic density (e.g. via the Mulliken method [81]) or fitting the electrostatic potential around the atoms (e.g. via the REPEAT method [82]). Some methods (e.g. DDEC [83]) use both the electronic density and the electrostatic potential. Partial charges also can be computed using charge equilibration methods, which base the partial charges on an atom's geometry, ionization potential, electron affinity, and atomic radius [84]. Although potentially less accurate, charge equilibration methods require significantly less computing time than ab initio methods, and they can therefore be appropriate for screening large numbers of materials.

The term "force field" refers to the combination of the functional form of the interatomic potentials and their corresponding parameters.

Ising model

We use the Ising model, a lattice model of interacting particles, to simulate MOF self-assembly. In this model, the energy of the system is given by [85]

$$E = -J \sum_{\langle i,j \rangle} s_i s_j - h \sum_i s_i, \tag{1.4}$$

where s_i indicates the state or phase of site i, $\langle i, j \rangle$ indicates a sum over nearest-neighbor sites, J represents the interaction energy between two sites, and h represents a chemical potential that can be tuned to favor a certain phase.

In our simulations, the two states in which each site can exist are: 1) $s_i = 1$, occupied by a MOF building block, which corresponds to the crystalline phase, and 2) $s_i =$ -1, unoccupied by a MOF building block, which corresponds to the solution phase.

This implementation of the Ising model is suitable for studying nucleation of MOF clusters from MOF building blocks. Since $J > 0$, it is energetically favorable for neighboring sites to assume the same state. Therefore, at low-enough temperature, this tendency leads to spontaneous magnetization, where the net magnetization $\langle M \rangle$ of the lattice in the absence of a magnetic field h,

$$\langle M \rangle = \sum_{i=1}^{N} s_i, \tag{1.5}$$

is nonzero. This phenomenon is illustrated in Figure 1.5.

In the presence of a magnetic field h, at a temperature lower than the critical temperature, $\langle M \rangle$ will be positive if h is positive, and vice versa. In the simulations in this work, $h > 0$, favoring the crystalline MOF phase. We prepare the system in the solution phase; that is, $\langle M \rangle = -N$. Since $h > 0$, the system spontaneously undergoes a transition to the crystalline phase, $\langle M \rangle = N$, as indicated in Figure 1.6. Spontaneous fluctuations in the system eventually give rise to the nucleation of a critical cluster, a cluster of sites in the crystalline phase of size sufficiently large such that the favorable bulk contribution to its free energy outweighs the surface tension penalty. In Chapter 5 we study the nature of such nucleation events.

The Ising model is the simplest model that takes into account particle interactions and predicts phase transitions [85]. This model's simplicity is advantageous for isolating the fundamental effects of framework geometry on MOF nucleation and also for performing

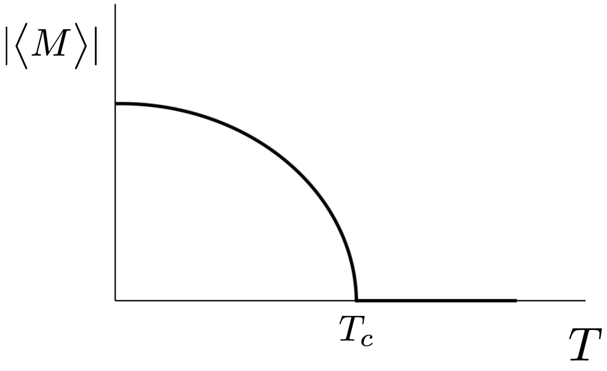

Figure 1.5: Net magnetization $\langle M \rangle$ vs. temperature. In the absence of a magnetic field h, and below the critical temperature T_c, the Ising model predicts spontaneous magnetization, or nonzero $\langle M \rangle$. This plot depicts $N \to \infty$, where N is the number of lattice sites.

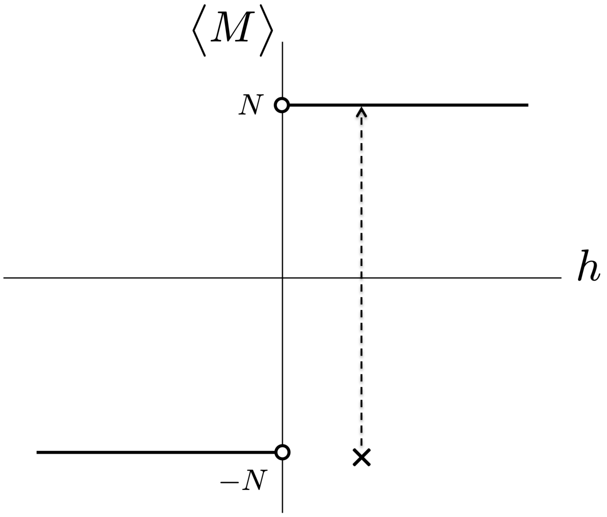

Figure 1.6: Net magnetization $\langle M \rangle$ vs. magnetic field h at a temperature less than the critical temperature. In the simulations in this work, $h > 0$. We prepare the system with $\langle M \rangle = -N$, as denoted by the black ×. The system spontaneously transitions to the state favored by h. This plot depicts $N \to \infty$.

simulations that are more computationally tractable than modeling MOF assembly atomistically. We note that a lattice model is appropriate for studying well-defined, crystalline materials, as we focus on in this work.

Monte Carlo simulations

Monte Carlo simulations use random numbers to efficiently sample a given probability distribution. The probability distributions of two statistical mechanical ensembles are relevant in the studies undertaken herein:

Grand-canonical ensemble: The grand-canonical ensemble describes a system with fixed chemical potential μ, volume V, and temperature T, and fluctuating energy E and number of particles N. This ensemble mimics experimental adsorption, where the chemical potential and temperature inside and outside the adsorbent are equal. In molecular simulations, one can implement the grand-canonical ensemble by placing the adsorbent in indirect contact with an infinitely large reservoir that imposes T and μ. Chemical potential and partial pressure can be related by an equation of state, such as the ideal gas law, van der Waals equation of state, or Peng-Robinson equation of state.

The grand-canonical distribution giving the probability of the system existing in a given state or configuration is [69]

$$p(\mathbf{r}^N; N) \sim \frac{V^N e^{\beta\mu N}}{\Lambda^{3N} N!} e^{-\beta E(\mathbf{r}^N)}, \tag{1.6}$$

where $\beta \equiv 1/k_{\mathrm{B}}T$, Λ is the thermal de Broglie wavelength, and $E(\mathbf{r}^N)$ is given by Equation 1.1. A configuration is defined by $\mathbf{r}^N$, or the spatial coordinates of all N adsorbate particles inside the adsorbent. Monte Carlo simulations that sample this distribution are referred to as grand-canonical Monte Carlo (GCMC) simulations.

Canonical ensemble: The canonical ensemble describes a system with constant number of particles N, V, and T, but fluctuating energy E. This ensemble mimics the case of a single adsorbate molecule in the limit of infinite dilution ($N \to 0$) or the case where we want to gather statistics for a constant number of adsorbate molecules. It is also appropriate for the lattice models used for studying MOF assembly in this work, where N corresponds to the (fixed) number of lattice sites.

The canonical distribution giving the probability of the system existing in a given state or configuration is [69, 85]

$$p(\mathbf{r}^N) \sim e^{-\beta E(\mathbf{r}^N)}, \tag{1.7}$$

where $E(\mathbf{r}^N)$ is given by Equation 1.1 (molecular simulation) or 1.4 (Ising). Again, a configuration is defined by $\mathbf{r}^N$. In molecular simulations, $\mathbf{r}^i$ is the spatial coordinates of adsorbate particle i. In Ising model simulations, $\mathbf{r}^i$ is simply s_i, the state of site i. The probability distribution (Equation 1.7) is also called the Boltzmann distribution. Monte Carlo simulations that sample this distribution are referred to as canonical Monte Carlo or NVT simulations.

In a Monte Carlo simulation, trial moves are performed in order to sample the probability distribution of interest. GCMC simulations for adsorption in nanoporous materials consist of random insertions, deletions, and translations of adsorbate molecules. Canonical Monte Carlo simulations for adsorption consist of random translations of the adsorbate molecule(s). Canonical Monte Carlo simulations for MOF assembly on a lattice consist of random spin flips (i.e. reversal of the state of a randomly-chosen site).

Trial moves are accepted or rejected according to the Metropolis algorithm, an efficient importance sampling technique [69]. In the canonical ensemble, the acceptance probability of a trial move under the Metropolis algorithm is [69]

$$p_{acc} = \min\left[1, e^{-\beta\Delta E}\right], \tag{1.8}$$

where ΔE is the change in energy of the system due to the trial move, as computed in molecular simulation by Equation 1.1 or in the Ising model by Equation 1.4. This acceptance probability means that if the trial move results in a decrease in the system's energy, the move is automatically accepted. If it results in an increase in the system's energy, the trial move is accepted if a randomly-drawn number between 0 and 1 is greater than $e^{-\beta\Delta E}$.

Similarly, in the grand-canonical ensemble, the acceptance probabilities for trial translation, insertion ($N \rightarrow N+1$), and deletion ($N \rightarrow N-1$) moves are [69]:

$$\begin{aligned}
p_{acc,\,translation} &= \min\left[1, e^{-\beta\Delta E}\right] \\
p_{acc,\,insertion} &= \min\left[1, \frac{V}{\Lambda^3(N+1)} e^{\beta\mu} e^{-\beta\Delta E}\right] \\
p_{acc,\,deletion} &= \min\left[1, \frac{\Lambda^3 N}{V} e^{-\beta\mu} e^{-\beta\Delta E}\right]
\end{aligned} \tag{1.9}$$

The Metropolis acceptance rules fulfill the condition of detailed balance, or microscopic reversibility, and ensure that, given a sufficiently large number of trial moves, the equilibrium canonical or grand-canonical distribution is sampled [69]. Thus Monte Carlo simulations are appropriate for computing thermodynamic properties of systems at equilibrium, as is the case for all systems investigated in this work.

Chapter 2

Screening covalent-organic frameworks for carbon capture

2.1 Introduction

Carbon capture and sequestration (CCS) is increasingly recognized as an important tool for lowering man-made CO_2 emissions and avoiding the most severe consequences of climate change [30]. An emerging method for CO_2 capture from flue gas emissions is selective adsorption of CO_2 on nanoporous materials. Metal-organic frameworks (MOFs) and zeolites have been studied extensively for CO_2 capture [17, 86–88], and characteristics that lead to successful carbon capture are relatively well understood [89]. The well-studied MOF-74 has been identified as one of the most promising MOFs for carbon capture, as its unsaturated metal coordination sites strongly bind CO_2 molecules and help lead to high CO_2 uptake from low-pressure gas streams and high selectivity for CO_2 over other flue gas components [90].

Covalent-organic frameworks (COFs) are a major class of nanoporous materials that, compared with MOFs and zeolites, have been understudied for carbon capture. COFs may be successful adsorbents for carbon capture because they have high porosities and internal surface areas like MOFs, but higher hydrothermal stabilities and lower molecular weights compared with MOFs and zeolites. Furthermore, the high CO_2 uptake of COFs, which is essential for an efficient carbon capture material, is well established [26, 91–94]. Additionally, previous studies suggest that COFs have high regenerability in a PSA, VSA, or TSA (pressure-, vacuum-, or temperature-swing adsorption) carbon capture process [95, 96], and several COFs with high CO_2/N_2 selectivity have been identified [27].

Here we examine a recently-published database of over 69,000 diverse, largely novel, in silico-designed COFs [25] that represent a variety of topologies and organic linkers. Using molecular simulations to simulate adsorption of major flue gas components (CO_2 and N_2) on these COFs, we study these COFs as adsorbents for a post-combustion carbon capture process at a coal-fired power plant using temperature-pressure swing adsorption (TPSA) for adsorbent regeneration. We use parasitic energy, as introduced by Lin et al. [97] and described by Huck et al. [98], as the metric to evaluate each material's carbon capture performance. Parasitic energy is the energy load imposed on a power plant when applying CCS using a given material as the CO_2 adsorbent. Compared with other proposed carbon capture performance metrics, such as CO_2 adsorption selectivity or heat of adsorption, parasitic energy more closely approaches a life-cycle analysis, taking into account both the CO_2 separation and compression steps and more accurately capturing the overall energetic penalty that CCS imposes on the power plant [98]. A number of COFs are identified with parasitic energy lower than that of an amine scrubbing process using MEA, the currently dominant technology in practice. We examine geometric characteristics of COFs with low parasitic energy in order to better understand top-performing materials.

2.2 Methods

Geometric properties of each framework in the database were computed using the Zeo++ software package [99, 100]. Pore volume of a material is defined here as the volume occupiable by a spherical probe following the method of Ongari et al. [101], who showed that this definition of pore volume can be directly related to experimentally-measured pore volumes, unlike other methods of computing pore volume. We use a spherical probe of radius 1.82 Å, the kinetic radius of N_2, following convention in experimental and simulation studies [101].

Location and radius of blocking spheres, to block access to pockets inaccessible to CO_2 or N_2 molecules, were computed for a spherical probe of a radius consistent with the TraPPE force field used in the molecular simulations in this work (*vide infra*). For CO_2, we used a probe radius of 1.525 Å; this value is half the Lennard-Jones σ of oxygen, the larger of the two atom types in CO_2 in the TraPPE model. For N_2, we used a probe radius of 1.655 Å, half the Lennard-Jones σ of nitrogen in N_2. Surface area and largest free sphere diameter are those reported by Mercado et al. [25]

CO_2 and N_2 molecules were modeled using the TraPPE force field [102], while framework atoms were modeled using the DREIDING force field [79], which was the force field used for structure relaxation in the original database generation [25]. Lorentz-Berthelot mixing rules were used to obtain mixed Lennard-Jones parameters. Lennard-Jones potentials were truncated at 12.8 Å, with tail corrections, while Coulombic interactions were computed using the Ewald summation method. To compute COF atom charges, we used a charge equilibration (QEq) method [84] with atomic parameters (electronegativity and idempotential) tuned by a genetic algorithm to reproduce DFT-derived DDEC charges for a set of about 100 COFs containing all the available ligands and nodes in the database, and validated upon a different set of about 100 COFs chosen with the same criterion. The genetic algorithm is described in detail in a forthcoming publication [103]. The COF frameworks were modeled as rigid. The simulation box was created by replicating unit cells until the distance along each direction of the simulation box was longer than twice the Lennard-Jones cutoff distance.

CO_2 Henry coefficients and heats of adsorption at zero loading were computed from Widom insertions [69] using the RASPA software package [104]. Each simulation consisted of at least 5×10^3 Monte Carlo cycles, and pockets inaccessible to CO_2 were blocked using the blocks computed from Zeo++. The relative error of all Henry coefficients was less than 10%. Single-component CO_2 and N_2 adsorption isotherms and CO_2 and N_2 heats of adsorption at non-zero loading were obtained from grand-canonical Monte Carlo (GCMC) simulations [69] performed at 298 K. Heats of adsorption were computed from energy/particle fluctuations [105]. 10^3 equilibration and 10^4 production cycles of Monte Carlo moves were performed in each simulation. The relative error of most computed loadings and heats of adsorption was less than 10%. Quantities computed from Monte Carlo simulations were used for the purpose of comparing structures and identifying top performers; in this context, the relative error in computed quantities is acceptable.

Parasitic energy was computed as described by Huck et al. [98]. It consists of two components: the heat $Q_{\text{separation}}$ required to separate CO_2 from the flue gas, and the energy $W_{\text{compression}}$ required to compress the captured CO_2 to 150 bar, the pressure required for a typical transport and storage process [29]:

$$E_{\text{parasitic}} = Q_{\text{separation}} + W_{\text{compression}}. \tag{2.1}$$

$Q_{\text{separation}}$ consists of the energy needed to heat the adsorbent to the desorption temperature and the energy required to desorb CO_2 and N_2 [98]. $W_{\text{compression}}$ was computed using a functional representation developed by Huck et al. [98] that depends on the desorption pressure and final CO_2 gas purity.

Coal flue gas conditions were taken to be 40 °C and 1 atm with CO_2:N_2 molar ratio of 14:86. The density of each framework was determined and used for computing the sorbent mass in the calculation of energy required for desorption. Thermodynamic properties needed for computing parasitic energy (single-component CO_2 and N_2 adsorption isotherms and CO_2 and N_2 heats of adsorption) were obtained from grand-canonical Monte Carlo (GCMC) simulations as described above, and Ideal Adsorbed Solution Theory (IAST) [106], as implemented in the pyIAST package [107], was used to compute the multi-component adsorption isotherms from single-component isotherms. Henry coefficient and GCMC simulations were managed using the AiiDA informatic infrastructure [108].

2.3 Results

Relationships between CO_2 Henry coefficient and geometric framework properties

We first computed CO_2 Henry coefficients for all COFs in the database. A material's CO_2 Henry coefficient is related to CO_2 working capacity, defined as the difference in CO_2 uptake at the adsorption and desorption conditions. Lin et al. established that there exists an optimal range of Henry coefficient values that maximize working capacity, which can contribute to a lower parasitic energy and smaller amount of adsorbent required to remove a

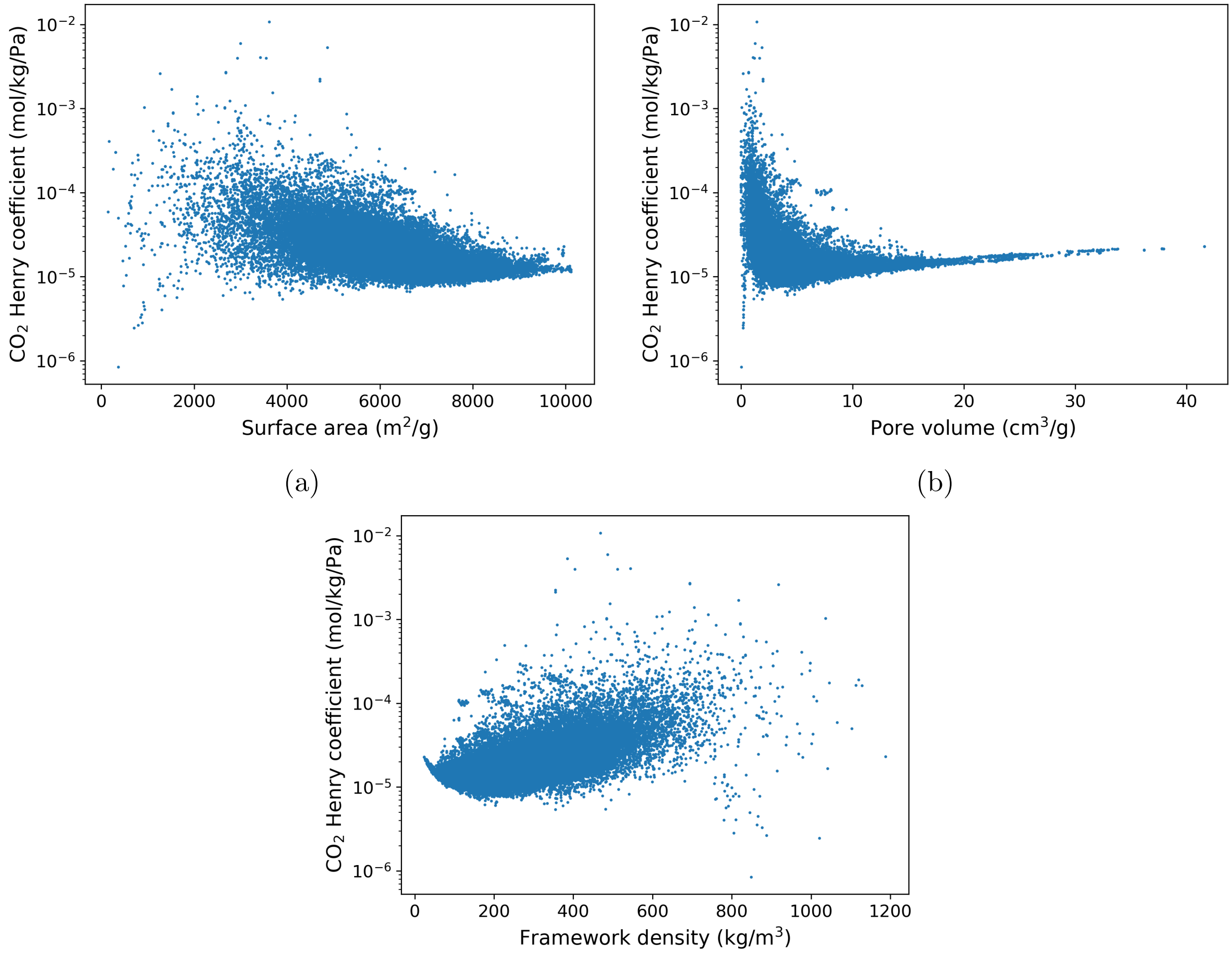

(a)

(b)

(c)

Figure 2.1: CO_2 Henry coefficient at 298 K as a function of a) surface area, b) accessible pore volume, and c) framework density for all COFs in the database.

given amount of CO_2 [97]. To gain insight on the relationship between CO_2 Henry coefficient and geometric properties of the COFs, we examined CO_2 Henry coefficient as a function of internal surface area, accessible pore volume, and framework density (Figure 2.1).

As surface area and pore volume increase and framework density decreases, the influence of pore topology decreases, and the Henry coefficient converges to a small range of values. We note that the maximum gravimetric surface areas, around 10,000 m^2/g, are remarkably high in the context of nanoporous materials [11].

Identification of COFs with minimum parasitic energy

A common relationship between CO_2 Henry coefficient and parasitic energy has been established for a range of nanoporous materials, including natural, synthetic, and hypothetical zeolites, MOFs, and porous polymer networks (PPNs) [97, 98]. Lin et al. have determined that the existence of an optimal value of CO_2 Henry coefficient that minimizes parasitic energy is attributed to a tradeoff between the greater CO_2 working capacity generally associated with higher CO_2 Henry coefficient and the higher cost of regeneration with higher Henry coefficient [97].

Having computed the CO_2 Henry coefficients of all COFs in the database, we selected about 150 COFs with a range of Henry coefficient values between 10^{-6} mol/kg/Pa and 10^{-2} mol/kg/Pa (the upper value corresponds to highest observed Henry coefficient in the database) for which to compute parasitic energy. We note that computing parasitic energy for the entire COF database is computationally intractable due to the computing time of the GCMC simulations needed for calculating parasitic energy. Based on these 150 COFs, we estimated the value of the optimal Henry coefficient and determined that the set of COFs with Henry coefficients above 10^{-4} mol/kg/Pa, of which there are 888, should include those with minimum parasitic energy. The parasitic energies of both the initial and latter sets of COFs are shown in Figure 2.2.

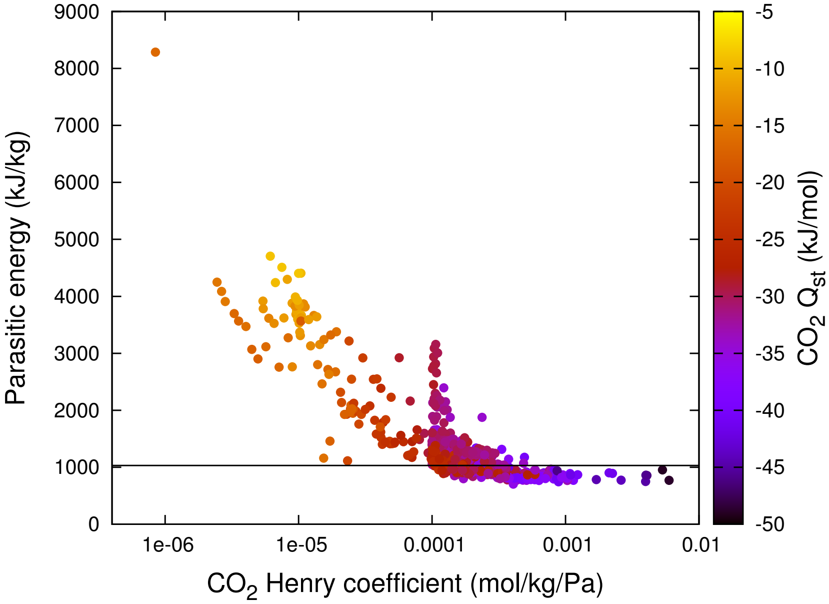

Figure 2.2: Parasitic energy vs. CO_2 Henry coefficient. The plot includes most COFs in the database that have Henry coefficients above 10^{-4} mol/kg/Pa. The color gradient denotes CO_2 isosteric heat of adsorption (Q_{st}) at zero loading. The horizontal line denotes the parasitic energy of an amine scrubbing process with MEA, as estimated by Huck et al. [98]

As expected based on other classes of nanoporous materials, there exists a range of values of Henry coefficient that minimizes the parasitic energy. In the case of the COF database, this value is between about 10^{-4} mol/kg/Pa and 10^{-2} mol/kg/Pa. Therefore, we can be confident that the COFs displayed in Figure 2.2 include most of those in the database with lowest parasitic energy, as well as most COFs with parasitic energy below that of an amine scrubbing process using monoethanolamine (MEA). MEA is widely used as the chemical absorbent in amine scrubbing processes and serves as the benchmark amine for CO_2 capture at power plants [30]. Numerous COFs in the database have parasitic energy below that of MEA. Furthermore, the CO_2 heat of adsorption at zero loading correlates strongly with Henry coefficient, as expected, and it explains some variation in parasitic energy of COFs with similar Henry coefficient but different parasitic energy (Figure 2.2).

Examination of top performers

We examined trends in top performers, those with lowest parasitic energy. Figure 2.3 shows parasitic energy as a function of framework geometric properties for all COFs with CO_2 Henry coefficient greater than 10^{-4} mol/kg/Pa. While nearly all top performers have a pore volume in the narrow range of 0-1 cm^3/g, surface area is a weaker predictor of low parasitic energy.

For this group of COFs, the most efficient process is a pressure swing combined with a small temperature swing (Table 2.1). In this case, $Q_{\text{separation}}$ is small since the temperature swing is small, so parasitic energy is dominated by $W_{\text{compression}}$ (Figure 2.4). The calculation of compression work does not take into account the amount of adsorbent material, only the desorption pressure and CO_2 purity. Therefore, it is also important to consider the working capacity of a material, since working capacity reflects the amount of material needed to remove a given amount of CO_2. A higher working capacity means that less material is needed, and therefore lower capital costs are entailed. Thus the top performers are not only those with low parasitic energy, but those that also have a high CO_2 working capacity. These materials are clearly seen in Figure 2.5. In particular, there are several COFs that have a parasitic energy and working capacity comparable to that of Mg-MOF-74, widely established as one the best-performing MOFs for carbon capture [90, 98].

The CO_2 purity of the final gas stream is another important consideration in a carbon capture process. CO_2 purity, computed as CO_2 working capacity divided by the sum of CO_2 and N_2 working capacities, increases with decreasing parasitic energy, meaning that the top performers also produce final streams with the highest CO_2 purity (Figure 2.6).

2.4 Conclusion

We have screened a database of over 69,000 diverse hypothetical COFs for carbon capture, evaluating their performance for a TPSA process at a coal-fired power plant using parasitic energy as a metric. By computing CO_2 Henry coefficients for the entire database and de-

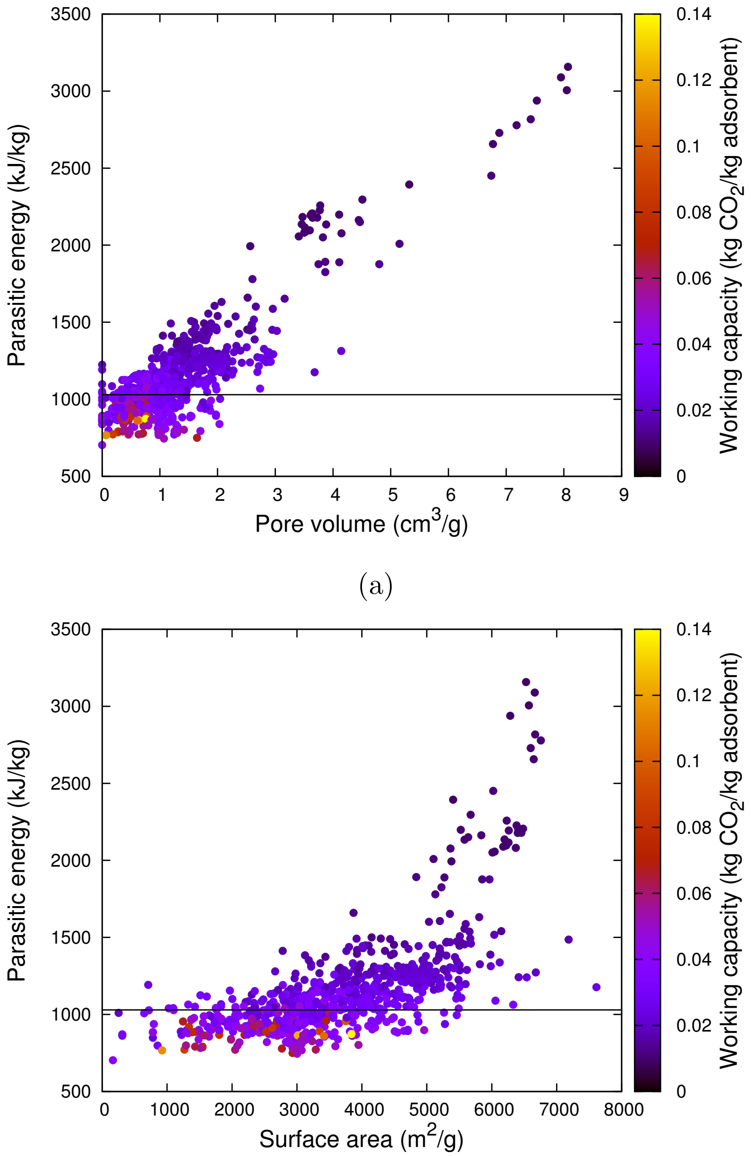

(a)

(b)

Figure 2.3: Parasitic energy vs. a) pore volume and b) surface area for each COF shown in Figure 2.2 with CO_2 Henry coefficient greater than 10^{-4} mol/kg/Pa. The horizontal line denotes the parasitic energy of an amine scrubbing process using MEA, as estimated by Huck et al. [98]

	Temperature	Pressure
Adsorption:	313 K	1 atm = 1.01325 bar
Desorption:	333-363 K	0.03-0.21 bar

Table 2.1: Adsorption conditions (temperature and pressure) considered in this work, corresponding to coal-fired power plant flue gas, and the minimum and maximum values of the optimal desorption conditions determined for each COF shown in Figure 2.2 with CO_2 Henry coefficient greater than 10^{-4} mol/kg/Pa. CO_2 working capacity is defined as the difference in CO_2 uptake at adsorption and desorption conditions. For all of these materials, a relatively large pressure swing combined with a relatively small temperature swing minimizes parasitic energy.

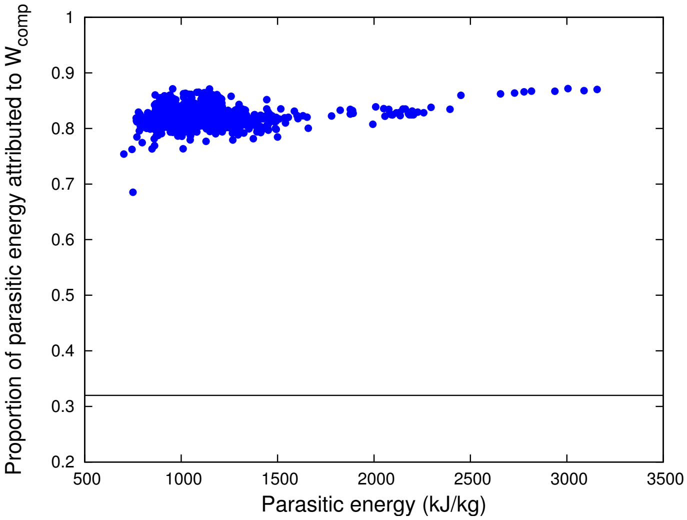

Figure 2.4: The proportion of parasitic energy attributed to compression work $W_{\text{compression}}$ (see Equation 2.1) for each COF shown in Figure 2.2 with CO_2 Henry coefficient greater than 10^{-4} mol/kg/Pa. The horizontal line marks this proportion, as computed by Huck et al. [98], for an amine scrubbing process using MEA, which involves a large temperature swing.

termining a relationship between Henry coefficient and parasitic energy, we identify COFs with the lowest parasitic energy in the database. Many COFs have parasitic energy lower than that of MEA, as well as a high purity of CO_2 in the final gas stream. These results indicate that COFs are promising carbon capture materials and merit further study for this application. On the broader scale, COFs could be used for a carbon capture process with lower parasitic energy than that of current technologies, resulting in more-economical carbon capture.

Future studies can examine the effect of gas stream impurities and of different concen-

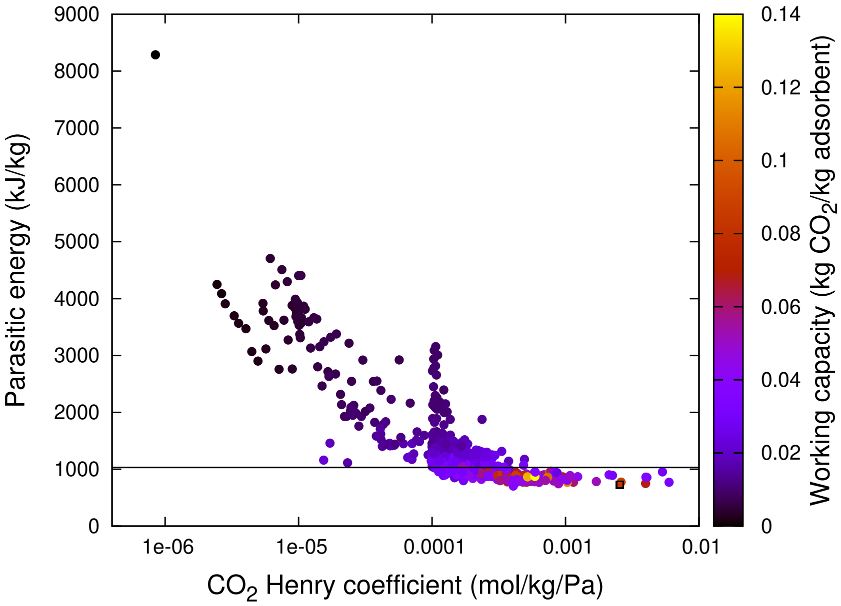

Figure 2.5: Parasitic energy vs. CO_2 Henry coefficient. Includes most COFs in the database that have Henry coefficient above 10^{-4} mol/kg/Pa. The color gradient denotes CO_2 working capacity. The horizontal line denotes the parasitic energy of an amine scrubbing process with MEA. The square with the black outline (lower right) denotes Mg-MOF-74, as computed by Huck et al. [98]

trations of CO_2 in the flue gas in order to obtain a more nuanced picture of COFs' carbon capture performance. Future studies can also aim to generate novel frameworks with pore volume in the range indicated in order to discover new materials with lower parasitic energy. Top performers identified in this study could be functionalized with amines, a strategy shown to improve CO_2 uptake and selectivity in MOFs [89], and evaluated for their carbon capture performance.

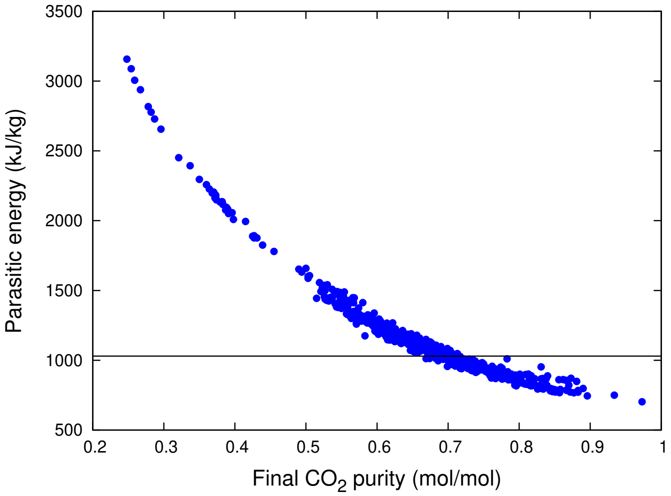

Figure 2.6: Parasitic energy vs. CO_2 purity of the final gas stream (mol CO_2 / (mol CO_2 + mol N_2)) for each COF shown in Figure 2.2 with CO_2 Henry coefficient greater than 10^{-4} mol/kg/Pa. Horizontal line denotes the parasitic energy of an amine scrubbing process with MEA, as estimated by Huck et al. [98]

Chapter 3

Screening nanoporous materials for hydrogen storage

3.1 Introduction

Widespread adoption of hydrogen, a clean fuel, in transportation vehicles could drastically cut CO_2 emissions from transportation, which accounts for about 20% of global CO_2 emissions [109]. A major challenge preventing significant use of hydrogen as a transportation fuel is lack of a method for affordable, safe on-board hydrogen storage with efficient, reversible hydrogen uptake and release. Storage of hydrogen in nanoporous materials is one potential method. Nanoporous materials' high surface areas and favorable interactions with hydrogen mean that a tank filled with such a material can have greater capacity than an empty tank [45]. Furthermore, since hydrogen physically adsorbs via weak van der Waals and electrostatic interactions in these materials, the adsorption process is reversible, and loading and unloading are fast compared with materials such as hydrides that chemically bind hydrogen [110].

For example, metal-organic frameworks (MOFs) with high hydrogen capacity and ultrahigh surface areas include MOF-210, which exhibits a hydrogen uptake of 167 mg/g (mg H_2/g MOF) at 77 K and 70 bar [111] and NU-100 with 163 mg/g [112]. It is plausible that with these uptakes, although at cryogenic rather than ambient temperature, these materials could be incorporated into a system that meets the U.S. Department of Energy's current long-term systems target for onboard hydrogen storage, 65 mg/g (mg H_2/g system) [113]. Other nanoporous materials that have been investigated for hydrogen storage include zeolites, carbon-based nanostructures, and organic polymer networks including covalent-organic frameworks (COFs) [45, 110].

In this study,[1] we perform an in silico screening of a library of over 850,000 well-defined

---

[1] The work in this chapter is based on material from the publication: A. W. Thornton, C. M. Simon, J. Kim, O. Kwon, K. S. Deeg, K. Konstas, S. J. Pas, M. R. Hill, D. A. Winkler, M. Haranczyk, and B. Smit. "Materials Genome in Action: Identifying the Performance Limits of Physical Hydrogen Storage."

crystalline nanoporous materials for room-temperature and cryogenic-compressed hydrogen storage. The screening involves thermodynamic models, molecular simulation, and a neural network machine learning algorithm to predict the net deliverable energy of each material. This metric is defined as the electrical energy from a certain volume of adsorbed hydrogen minus the energy required to cool and compress the hydrogen. The volumetric, rather than gravimetric, energy density is considered in this work since the former primarily determines driving range and cost of storage [15, 50]. With this screening, we aim to identify the limits of hydrogen storage via adsorption on nanoporous materials and to determine if there exist viable materials for hydrogen storage. The materials considered include hypothetical MOFs [114], computationally-ready experimental MOFs (CoRE-MOFs) taken from the Cambridge Structural Database (CSD) [115], hypothetical all-silica zeolites chosen from a set of energetically feasible structures from the Predicted Crystallography Open Database (PCOD) [116], ideal silica zeolites from the International Zeolite Association (IZA) [117], hypothetical covalent-organic frameworks (COFs) [118], hypothetical zeolitic imidazolate frameworks (ZIFs) [97], and hypothetical porous polymer networks (PPNs) [119].

3.2 Methods

The metric used in this study is net deliverable energy, which is computed from deliverable capacity. Deliverable capacity is defined as the difference between the hydrogen uptake per volume of material at the storage pressure (100 bar) and the hydrogen uptake at the depletion pressure (1 bar). At 298 K, Widom insertions [69] were performed to compute the H_2 Henry coefficient of a material. H_2 molecules were modeled as a single uncharged site. Lennard-Jones potential interaction parameters were taken from the Buch potential [72] for H_2 molecules and from the Universal Force Field (UFF) [78] for framework atoms. Lorentz–Berthelot mixing rules were used to obtain heterogeneous Lennard-Jones parameters. The choice of this force field is discussed in the Results section below. The Langmuir adsorption model, with the Henry coefficient from simulation and saturation loading determined from an empirical relation between saturation capacity and pore volume, was used to predict hydrogen uptake. At 77 K, the Langmuir model failed to adequately predict adsorption capacity because of the poor correlation between saturation capacity and pore volume, so hydrogen uptake was computed using grand-canonical Monte Carlo (GCMC) simulations, using the force fields described above. GCMC isotherms at 77 K were also used to train the neural network models.

Deliverable capacity was used to compute net deliverable energy, details of which can be found in the published work [120]. Full details on the use of the Langmuir adsorption model and empirical relation between saturation capacity and pore volume, calculation of optimal

---

Chemistry of Materials 2017, 29, 2844-2854. The material in this section focuses on the work that I primarily carried out: determination of a hydrogen force field for the molecular simulations used in this study. Results from the in silico screening are summarized within in order to illustrate how the zeolite force fields were used and the resulting information we gained. Complete details of the study can be found in the published work.

storage pressures, and the neural network algorithm can also be found in the published work [120].

3.3 Results

Force field selection for zeolites

Computing the metric, net deliverable energy, involves computing adsorption properties using molecular simulation. Here we discuss the choice of the Universal Force Field (UFF) [78] as the force field used for the framework atoms in all-silica zeolites. UFF, a general force field that is commonly used for MOFs, has been shown to satisfactorily model hydrogen adsorption in a range of MOFs [121–124], but has been less analyzed for hydrogen in zeolites. The relevant temperature and pressure regimes in which to validate UFF for zeolites in this study are 1) 77 K between 1 and 100 bar, the conditions of the computed isotherms used in calculating net deliverable energy for cryogenic storage and in training neural network models, and 2) 298 K in the Henry regime, the conditions corresponding to the computed Henry coefficients used in calculating net deliverable energy for room-temperature storage.

77 K: We compared three force fields for hydrogen adsorption at 77 K: UFF, UFF with the Feynman-Hibbs correction, and the force field presented by Deeg et al. [75], which also incorporates the Feynman-Hibbs correction. The third force field (Deeg et al.) was developed from experimental adsorption data on zeolites at cryogenic temperatures and shown to be transferable to different all-silica zeolites and cryogenic temperatures [75]. The Feynman-Hibbs correction is a correction to the Lennard-Jones potential that takes into account quantum effects by describing particles' positions with Gaussian distributions [125, 126]. In this work we use the quadratic Feynman-Hibbs effective potential for hydrogen-hydrogen and hydrogen-zeolite interactions:

$$U_{\mathrm{FH}}(r_{ij}) = U_{\mathrm{LJ}}(r_{ij}) + \frac{\hbar^2}{24\mu_{ij}k_{\mathrm{B}}T}\left[U''_{\mathrm{LJ}}(r_{ij}) + \frac{2U'_{\mathrm{LJ}}(r_{ij})}{r_{ij}}\right], \tag{3.1}$$

where r_{ij} is the distance between interacting particles i and j, $U_{\mathrm{LJ}}(r_{ij})$ is the classical Lennard-Jones pair potential, and μ_{ij} is the reduced mass of particles i and j given by $\mu_{ij}^{-1} = M_i^{-1} + M_j^{-1}$; M denotes molecular mass. $\hbar$, k_{B}, and T denote the reduced Planck constant, Boltzmann's constant, and temperature, respectively.

Numerous studies have established that use of the Feynman-Hibbs correction improves the accuracy of modeling hydrogen adsorption in nanoporous materials at cryogenic temperatures [75, 127–129].

With UFF, hydrogen was treated using the single-site model with the Buch potential [72], and hydrogen-zeolite interaction parameters were calculated using Lorentz-Berthelot mixing rules. Using these three force fields, we computed hydrogen adsorption isotherms at 77 K between 1 and 100 bar for four all-silica zeolites for which experimental or simulated adsorption data under these conditions has been reported. The comparisons between simulation results and reference results are shown in Figure 3.1.

In conclusion at 77 K, the comparisons show that, in agreement with previous studies, the Feynman-Hibbs correction in the UFF potentials improves agreement between computed loading and experimental loading. While the force field from Deeg et al. matches experiment closely in most cases, UFF with the Feynman-Hibbs correction usually overestimates the experimental loading. However, since the loading computed from UFF with the Feynman-Hibbs correction is consistently greater than that computed with Deeg et al., the deliverable capacity computed using the two force fields is similar.

298 K: At 298 K, we examined UFF as well as three other force fields for modeling hydrogen adsorption. The latter three force fields were developed specifically for hydrogen in zeolites and therefore taken as the reference against which to compare UFF, since we are not aware of any experimental data reported for hydrogen adsorption in zeolites at room temperature at pressures in the Henry regime. The first of the three reference force fields, from Deeg et al. [75], was modified from an existing force field by fitting parameters to experimental hydrogen adsorption data in all-silica zeolites at 77 K. The second reference force field, from Mahmati et al. [132], uses hydrogen parameters presented by Kumar et al. [127] adjusted to agree with GCMC simulations of bulk hydrogen and validated against experimental adsorption isotherms in zeolites. The third reference force field, from van den Berg et al. [131], was developed for hydrogen in zeolites and derived from experimental data.

Adsorption isotherms at 298 K in the Henry regime were computed for six all-silica zeolites. The comparisons between UFF results and reference force field results are shown in Figure 3.2.

In conclusion at 298 K, in all the zeolites considered, UFF-computed loading is higher than that computed by the reference force fields. Nevertheless, given the significant variation in loading among the reference force fields, the UFF results are reasonable.

Conclusions: We proceed with the screening portion of the study using UFF with the Buch single-site hydrogen potential and the Feynman-Hibbs correction at 77 K, given the reasonable agreement with loading computed from reference force fields in the Henry regime at 298 K and the satisfactory agreement with experimental deliverable capacity at 77 K. Furthermore, since the variation between UFF-computed loading and experimental or reference loading is consistent among different zeolites, UFF should be reliable for the purpose of comparing zeolites.

The consistent overestimation of loading using UFF is likely due in large part to the high interaction energy between hydrogen and zeolite silicon atoms according to this force field. Since UFF is a general force field, it does not reflect the fact that zeolite-adsorbate interactions are generally dominated by dispersive interactions between the adsorbate and the zeolite oxygen atoms, since the zeolite silicon atoms' accessibility to adsorbates is reduced

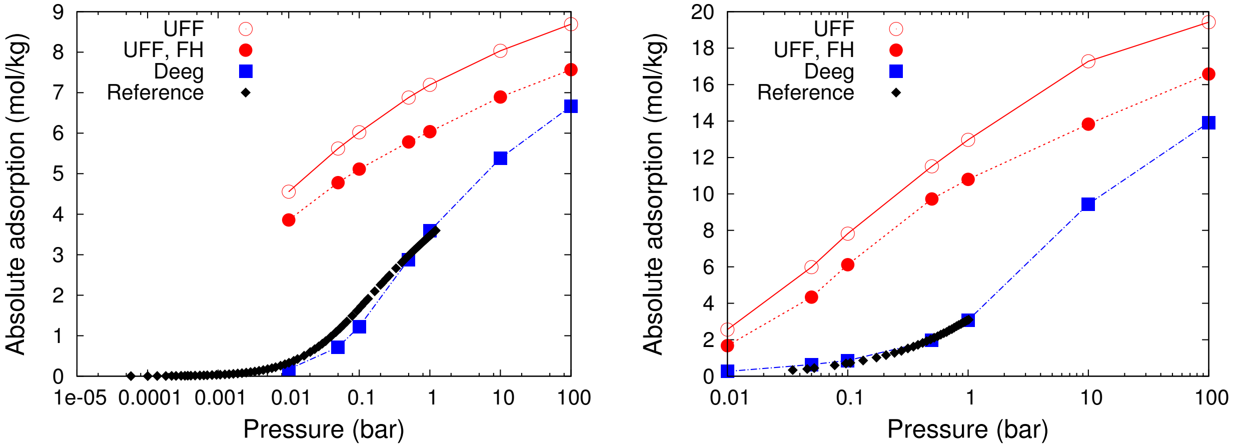

(a) MFI (b) FAU

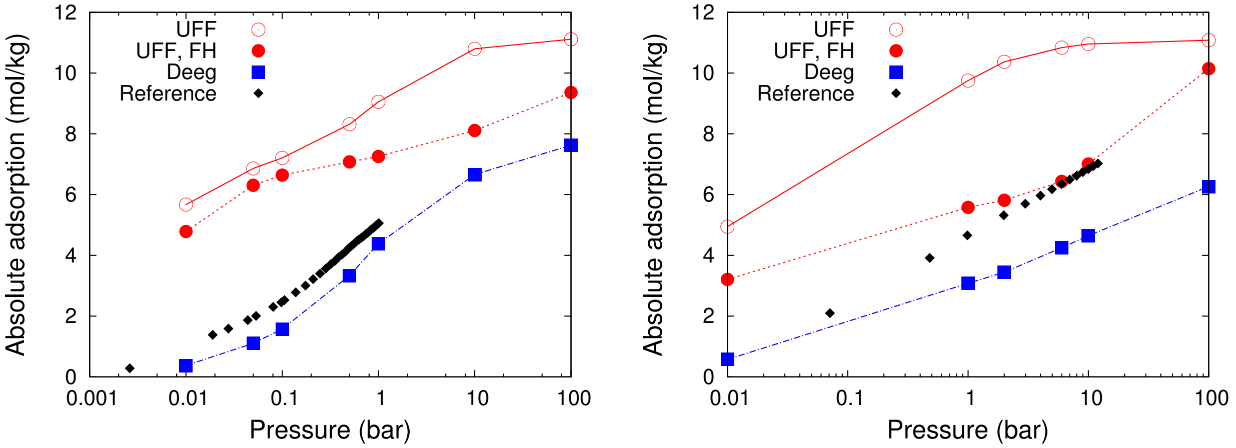

(c) MOR (d) SOD

Figure 3.1: Hydrogen adsorption isotherms at 77 K in different all-silica zeolites: a) MFI, b) FAU, c) MOR, and d) SOD. For each zeolite, adsorption isotherms were computed using UFF (empty circles), UFF with the Feynman-Hibbs correction (filled circles), and the force field presented by Deeg et al. (filled squares). Reference data (black diamonds) is from experiments reported in Deeg et al. [75] (a), experiments reported in Jhung et al. [130] (b, c), and GCMC simulations reported in van den Berg et al. [131] (d). Note that the experimental data for FAU and MOR were measured on aluminosilicate zeolites with high Si/Al ratio: 60 (FAU) and 90 (MOR); hydrogen uptake in the all-silica versions of these zeolites would be slightly lower.

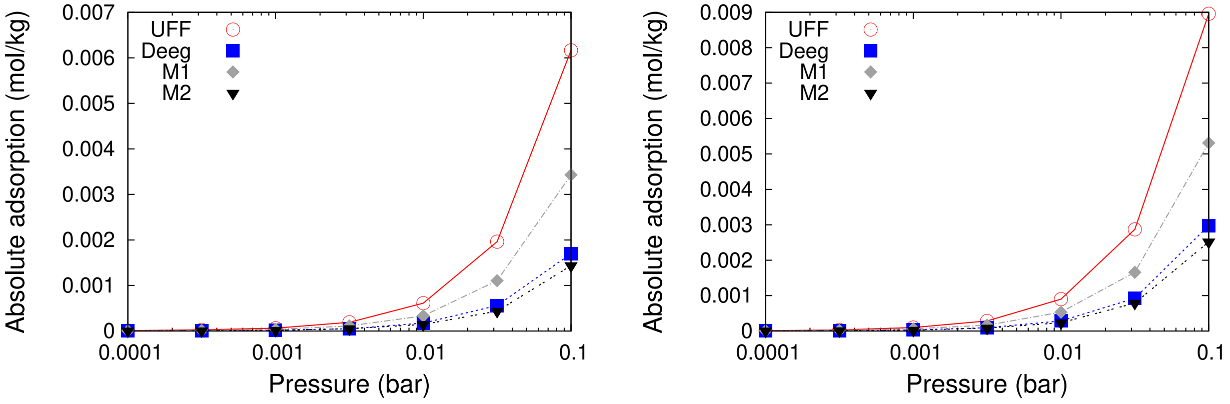

(a) MFI (b) ITQ-29

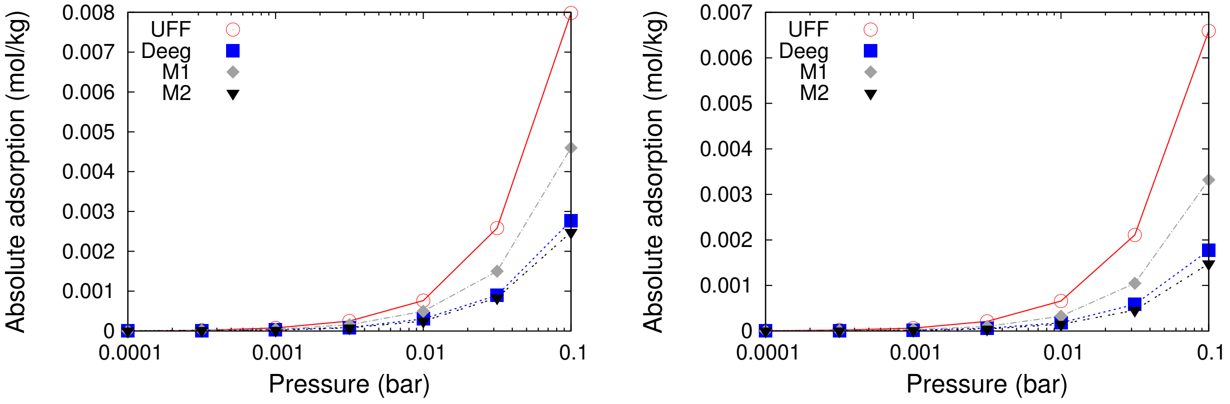

(c) FAU (d) MOR

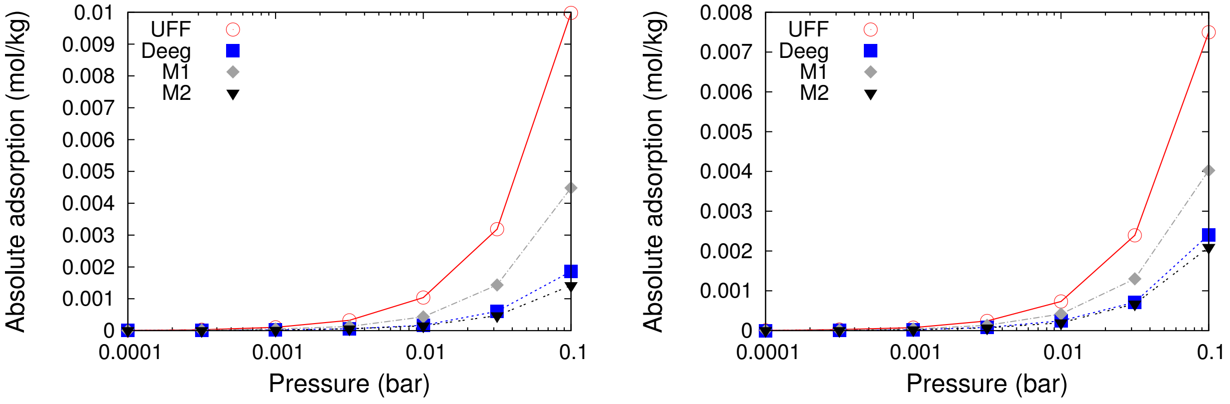

(e) SOD (f) RHO

Figure 3.2: Low-pressure hydrogen adsorption isotherms at 298 K in different all-silica zeolites: a) MFI, b) ITQ-29, c) FAU, d) MOR, e) SOD, and f) RHO, computed using UFF (circles) and three different reference force fields: Deeg et al. (squares), Rahmati et al. ("M1", diamonds), and van den Berg et al. ("M2", triangles).

due to the geometry of the the SiO_4 tetrahedra [133, 134]. Thus the UFF hydrogen-silicon Lennard-Jones ϵ parameter is artificially high (Table 3.1).

	H_2-H_2		H_2-O_{zeo}		H_2-Si_{zeo}	
	ϵ	σ	ϵ	σ	ϵ	σ
Deeg et al.	36.733	2.958	66.055	2.89	28.256	1.854
UFF	34.2	2.96	32.136	3.04	83.182	3.393

Table 3.1: Lennard-Jones parameters for two force fields considered in this work for modeling hydrogen adsorption in zeolites. UFF H_2-H_2 parameters are those of the Buch potential [72], and UFF mixed interaction terms are computed using Lorentz-Berthelot mixing rules.

As previously discussed, UFF has been shown to be reasonably accurate for modeling hydrogen adsorption in MOFs, which represent the majority of the materials in the library screened in this study. Using the same force field for the entire materials database considered in this study allows fairer comparison between different classes of materials, so we proceed with the UFF force field with the Feynman-Hibbs correction at 77 K.

Hydrogen storage screening

Storage at room temperature: For room temperature storage, the maximum net deliverable energy using adsorbents at pressures between 100 and 1 bar is about 0.4 kWh/L, as shown in Figure 3.3 for the complete database (about 850,000 materials). This is well below the net energy 1.2 kWh/L delivered by high compression (700 bar) systems. Deliverable energy is maximized at void fractions of 0.1 and pore sizes of 6 Å. At the predicted optimal storage pressures, the net deliverable energy is close to the DOE target; however, the pressures required are greater than 1,000 bar. Therefore, it is likely more economical to operate without an adsorbent at room temperature.

Storage at cryogenic temperatures: To evaluate hydrogen storage at cryogenic temperatures, isotherms between 100 and 1 bar were computed using GCMC simulations. The simulations were run in stages, where results from each stage were fed into a neural network to generate models that identified the next set of materials to simulate. The first stage of GCMC simulations was run on the complete set of known IZA zeolites and a diverse set of hypothetical zeolites selected on the basis of molecular similarity [135], shown as red circles in Figure 3.4. A neural network model was then constructed, and a new set of materials with improved properties were identified. The limited parameter space (domain of applicability) of zeolites meant that the neural network model suggested structures with the largest amount of void fraction, consisting of PPNs and COFs. The top 1,000 structures suggested by the neural model in the first stage were then simulated using GCMC, and the results are shown as blue circles in Figure 3.4. As expected, the difference between the stage 1 neural network predictions and the GCMC simulations were large because of the limited information used to train

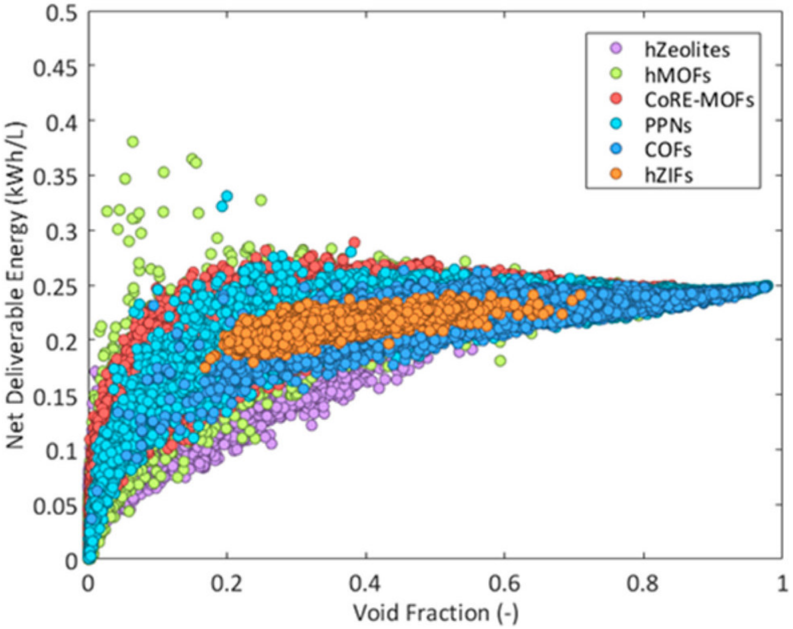

Figure 3.3: Net deliverable energy, predicted at room temperature and cycling between 100 and 1 bar, versus void fraction, for the entire database.

each neural network model. However, the new GCMC results were used to further retrain the neural model, and more complex relationships between the structural descriptors of the materials and performance were subsequently observed. For example, an optimal range was identified for each parameter, including a pore diameter of around 6 Å and surface area of 4,000 m^2/g. The range of materials found within these optimal ranges included a combination of hypothetical MOFs and CoRE-MOFs. A third stage of GCMC simulations was run for the next top 1,000 structures suggested by the neural model, which was once again retrained on the new simulated data, shown as green circles in Figure 3.4. The new results identified an optimal range of void fraction around 0.5, highlighting a trade-off between free space for adsorbed H_2 molecules and a framework to construct binding sites with a high affinity for hydrogen. A final neural network model was developed with this additional simulation data that revealed a convergence in the list of top candidates; i.e., no new candidates were suggested. This can be seen in Figure 3.4 where the final neural model predictions are shown as pale gray circles. To ensure that the neural network had a sufficiently large domain of applicability in the available parameter space, a diverse test set of candidates (based on molecular similarity [135]) was tested. No new high performing candidates were discovered, confirming that the neural network has captured enough of the parameter space to arrive at a good approximation of the global maximum. Furthermore, the neural network model predicted the performance of the diverse test set with good accuracy ($R^2 = 0.88$ and root mean squared error of 3.64), showing that it could accurately predict the properties of materials not used in the training set.

The top candidates were predicted to deliver a net energy of around 1.3 kWh/L, well above the bare tank option at 1.02 kWh/L for the same operating conditions. Catenated hypothetical MOFs, as well as CoRE-MOFs, were the most common among the highest-performing candidates. Compared to current industrial practice, this maximum net deliverable energy by adsorbents is higher than the 700 bar compression technology (1.2 kWh/L) but lower than the liquefaction option (2.1 kWh/L). The advantage of cryo-adsorption is clearly in applications where high pressures (700 bar) and low temperatures (20 K) are not appropriate due to safety, source of hydrogen, available floor space, engineering factors, cost, or other restrictions. For example, adsorbents can reduce the high pressures in confined spaces, which are considered unsafe or at least undesirable, although carbon fiber composites are raising the reliability of storage tanks. Another example to consider is for locations with access to liquid nitrogen but not the equipment required to produce liquid hydrogen. In this example, adsorbents will offer the additional storage performance. Hydrolyzers produce hydrogen at high temperatures, and therefore another opportunity for adsorbents could be to adsorb this hydrogen along heat exchangers.

To better understand this predicted peak in net energy at an optimal void fraction of 0.5, the Langmuir model was fitted to the final neural network predictions (solid dark gray line in Figure 3.4). By simply assuming that the saturation capacity and adsorption energy are linear functions of void fraction, the data were fitted with high accuracy ($R^2 = 0.985$). These generalized semi-empirical relationships were observed previously, and the trends are confirmed in this work [97, 136, 137]. Saturation capacity is an increasing function of void fraction while adsorption energy (represented as positive values, where a large positive value is a strong attractive adsorption energy) is a decreasing function of void fraction. This model intuitively captures the natural trade-off between saturation capacity and adsorption energy, which are proportional to and inversely related to void fraction, respectively.

Experimental data were collected from a range of review articles including Sculley et al. [138], Suh et al. [139], Yang et al. [140], Hu et al. [141], Lai et al. [142], and Murray et al. [143] A selection is plotted in Figure 3.4 as black squares. Top candidates include MOF-210 [111], NOTT-400 [144], PCN-68 [145], and ZIF-8 [146]. The reason for discrepancies between simulation and experiment is difficult to identify because of the multiple, interdependent variables involved in the synthesis and measurements, as well as the assumptions behind the simulations. For example, adsorption in ZIF-8 has proven difficult to predict due to observed "gate-opening" effects whereby the imidazole groups rotate at high pressures to adsorb more gas [147]. Adsorption in MOF-210 has also proven difficult to predict because of its large unit cell containing 5562 atoms [111]. Furthermore, the force fields used in this study cannot adequately treat interactions between hydrogen molecules and open metal sites in MOFs; introduction of the latter is a promising strategy for improving hydrogen storage in MOFs [143]. Although there is significant scatter across void fraction and deliverable capacity, a maximum is also observed close to that of the predictions at around 1.3 kWh/L.

The top candidates are illustrated in Figure 3.5 and consist of two hypothetical MOFs, two CoRE-MOFs with no known experimentally-measured hydrogen uptake, and two CoRE-MOFs where experimental hydrogen uptake is available. The top hypothetical MOF candi-

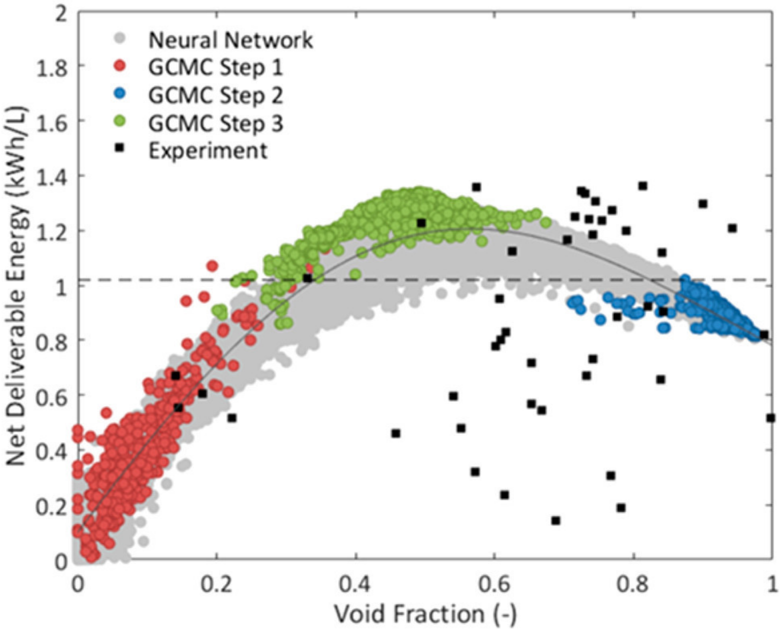

Figure 3.4: Net deliverable energy as a function of void fraction for the predictive and experimental data at 77 K cycling between 100 and 1 bar. Predictions include the GCMC-simulated sample sets and the final neural network model for the complete genome (about 850,000 materials). Experimental data from the literature is shown as black squares with top candidates including NOTT-400, MOF-210, ZIF-8, and PCN-68. Dashed line represents the predicted bare tank performance based on NIST data. Solid dark gray line represents the fitted Langmuir model.

dates contain long and thin ligands such as alkynes that maximize surface area and porosity. hypMOF-5003600 is an interpenetrated zinc-based cubic framework while hypMOF-5059389 is functionalized with hydroxyl groups, and both strategies are typically adopted to maximize adsorption energy. The top candidates share common characteristics such as a void fraction close to 0.5 and a major pore diameter of around 10 Å, along with high surface areas above 3,000 cm^2/cm^3 and 5,000 m^2/g. The exception is MOF-210 with a wide distribution of pores from 10 up to 28 Å.

Hypothetical MOF-5059389 was identified to have the highest working capacity, of 40 g H_2/L, of all materials in the database. This corresponds to a 30% enhancement above the bare-tank scenario (Figure 3.6).

3.4 Conclusion

A library of over 850,000 nanoporous, crystalline structures, was screened computationally using a combination of molecular simulation and machine learning techniques to explore the limits of physisorbed hydrogen storage.

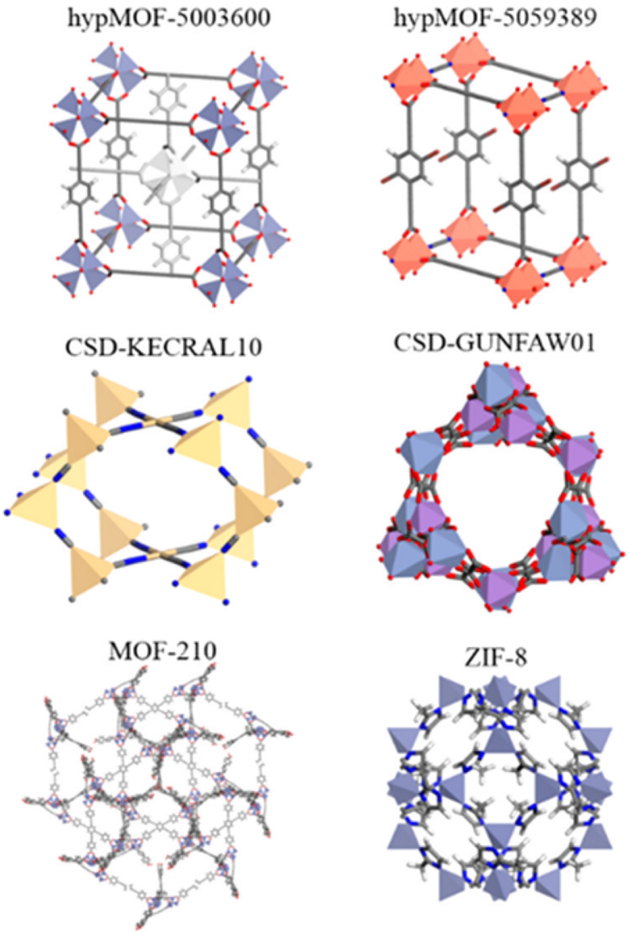

Figure 3.5: Top candidates for hydrogen storage at 77 K. Structures include two hypothetical MOFs that have never been synthesized, two MOFs from the Cambridge Structural Database (CSD) that were synthesized but never tested for hydrogen storage [148, 149], and two MOFs that have been synthesized and measured for hydrogen storage [111, 146]. Color code for atoms: Zn (lavender), Cd (yellow), C (gray), O (red), N (blue), H (white), Cr (violet), Mn (dark blue), and Cu (orange).

Focusing on the net energy derived from deliverable capacity between 100 and 1 bar, use of the Universal Force Field was validated for describing zeolite-hydrogen interactions in the molecular simulations portion of this study. It was also determined that the Feynman-Hibbs correction for taking into account quantum effects of H_2 improves the accuracy of the model at 77 K. Ultimately, the finding that zeolites generally deliver a lower net deliverable energy than MOFs, PPNs, and COFs (Figures 3.4 and 3.3) is expected, as it has been established in previous studies that zeolites' relatively low surface areas and high density compared with these other classes of nanoporous materials [3, 150] usually result in a lower deliverable capacity in zeolites.

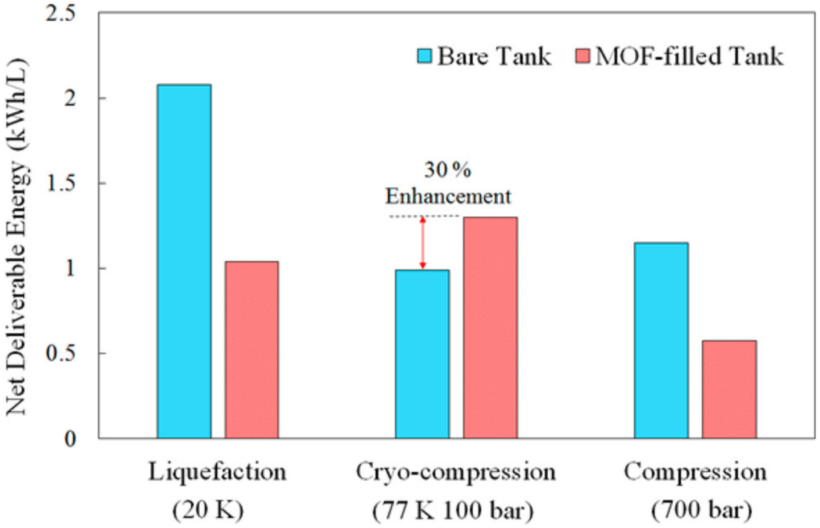

Figure 3.6: Net deliverable energy with and without MOF for the available storage conditions associated with liquefaction, cryo-compression, and compression. The top identified candidate hypMOF-5059389 is chosen for comparison. The 30% enhancement is observed for the MOF-filled tank at cryo-compression conditions which corresponds to about 30% enhancement in volumetric capacity to 40 g/L.

Optimal candidates were discovered that consisted of both hypothetical MOFs and already-synthesized CoRE-MOFs. MOF-210, PCN-68, NOTT-400, and ZIF-8 were four of the best materials identified, and experimental validation for their high hydrogen storage performance was found in the literature. Other top candidates included MOFs that have been synthesized in the literature but not yet measured for hydrogen capacity, such as the cadmium-based framework and the mixed-metal chromium-manganese based framework. Furthermore, hypothetical MOF candidates with a combination of large void fraction and high adsorption energy were also predicted to perform at a high level. Optimal characteristics were determined, including a void fraction of 0.5, a pore diameter of 10 Å, and a surface area of 5,000 m^2/g, which offer quantitative guidelines for the future design of nanoporous materials for hydrogen storage.

Finally, the maximum net deliverable energy was found to be around 1.3 kWh/L, which is well above the 1.02 kWh/L for the bare tank scenario at identical operating conditions, 1 to 100 bar at 77 K. In addition, this technology termed "cryo-adsorption" has significant engineering advantages over the current liquefaction (20 K) and mega-compression (700 bar) storage technologies.

Chapter 4

Detailed investigation of a novel biporous metal-organic framework for natural gas processing

4.1 Introduction

Natural gas processing, or the removal of CO_2 and other impurities from raw natural gas, is performed on a huge scale worldwide. Natural gas currently accounts for 22% of global energy use, and demand is expected to grow 1.6% annually through 2022 [55, 57].

For removal of acid gases such as CO_2 and H_2S from natural gas, amine absorption techniques are most commonly used [151]. While these techniques are effective at reducing acid gas levels, they consume large amounts of energy in order to regenerate the amine solvents. Furthermore, since the amine absorbents are dissolved in water, the natural gas becomes mixed with water, which must subsequently be removed.

Physical adsorption on nanoporous materials is an emerging alternative technique for separating CO_2 from CH_4, the primary component of natural gas [65, 152, 153]. The interaction between CO_2 and the adsorbent is weaker than that between CO_2 and an amine solution, so less energy is required to regenerate the sorbent [63]. MOFs have been well studied at the laboratory level for CO_2 separation from natural gas and biogas, and several show potential for successful application at scale [64, 66, 154].

Biporous MOFs [155–157], only a handful of which have been reported, offer different chemical environments within a single material, leading to complex and varied structure–adsorbate chemical interactions that can be harnessed for gas separations and other applications. Such MOFs have been shown to exhibit highly selective gas separations [158], while biporous coordination networks have been studied for their gas separation performance [159] and unusual ability to store differing gas species [160, 161]. Even fewer biporous MOFs have had practical use made of their biporosity, e.g. by taking up mutually incompatible molecules [160], selective recognition of alcohol molecules [162], or alternating the gas sorption properties [163]. More widely encountered are MOFs with chemically distinct types of nanocages [164, 165]. Given the interesting fundamental gas adsorption behavior in biporous materials and their potential for gas separations and other applications, we emphasize the importance of fully understanding and characterizing biporous materials, as we have undertaken for the MOF introduced here.

In this study,[1] we present the synthesis of a novel biporous MOF based on Ca(II) and a tetracarboxylate ligand featuring two chemically distinct types of pores: hydrophobic and hydrophilic. Owing to judicious choice of conditions, both the fully-activated material and the partially-activated material with exclusively hydrophobic pores activated are obtained. The difference in the sorption behavior of these materials was rationalized in terms of different molecular interactions between the partially and the fully activated material and CO_2 or CH_4, and the selectivity of CO_2 over CH_4 was studied with breakthrough experiments and molecular simulations.

4.2 Methods

Periodic density functional theory

Structure relaxation and binding energy calculations were performed using periodic density functional theory (DFT) calculations as implemented in the Quantum Espresso software package [166]. The PBE functional [167] as well as the DFT-D2 correction for dispersion interactions [168] were used for all calculations. The projector-augmented wave approximation (PAW) [169] was adopted, using a plane-wave kinetic energy cutoff of 90 Ry, which ensures the electron energy is converged to within 1 mRy. The Brillouin-zone sampling was performed on a Gamma-centered Monkhorst–Pack k-point mesh of 2 × 1 × 1 points, due to the unit cell's short a-dimension (about 7 Å). The crystal structure used in all simulations was obtained by performing a DFT relaxation on the experimentally determined structure. Binding energies (BE) for an adsorbate (ads) were computed according to the following formula:

$$\mathrm{BE}(\mathrm{ads}) = E(\mathrm{MOF} + \mathrm{ads}) - E(\mathrm{MOF}) - E(\mathrm{ads}) \tag{4.1}$$

For dimethylformamide (DMF) binding energies, $E(\mathrm{MOF} + \mathrm{ads})$ was computed by allowing the DMF molecule as well as the MOF atom positions and unit-cell dimensions to change during the DFT relaxation. We found that assuming a nonrigid MOF was necessary to

---

[1] The work in this chapter is based on material from the publication: A. Gładysiak, K. S. Deeg, I. Dovgaliuk, A. Chidambaram, K. Ordiz, P. Boyd, S. M. Moosavi, D. Ongari, J. Navarro, B. Smit, and K. C. Stylianou. "Biporous Metal–Organic Framework with Tunable CO_2/CH_4 Separation Performance Facilitated by Intrinsic Flexibility." *ACS Applied Materials & Interfaces* 2018, 10, 36144-36156. While the material in this chapter focuses on the work that I primarily carried out, selected experimental and simulation results from the co-authors of this study are summarized within in order to illustrate the motivation for my analyses and to compare with results from my simulations. Complete details of co-authors' experiments and simulations from this study can be found in the published work.

capture the hydrogen bonding that occurs between a DMF molecule and a bound water molecule in the hydrophilic pore.

Monte Carlo

CH_4, CO_2, and N_2 single-component adsorption isotherms, as well as CH_4/CO_2 dual-component mixture isotherms, were computed using grand-canonical Monte Carlo (GCMC) simulations performed in the RASPA software package [104]. Lennard-Jones potentials were truncated and shifted to zero at 12 Å. Coulombic interactions were computed using the Ewald summation method. CO_2, CH_4, and N_2 molecules were modeled using the TraPPE force field [80, 102]. DMF Lennard-Jones parameters were those presented by Sarkisov [170], with the charges presented by Vasudevan and Mushrif [171]. MOF Lennard-Jones parameters were taken from Wu et al. [172], with framework oxygen Lennard-Jones parameters obtained using the formula described in this same work for modifying UFF parameters. MOF atom charges were computed using the REPEAT scheme [82]. Lorentz–Berthelot mixing rules were applied to all heterogeneous Lennard-Jones parameters. For single-component isotherms, at least 10^5 (CH_4) and 5×10^4 (CO_2) equilibration cycles of Monte Carlo trial moves and at least 2.5×10^5 (CH_4) and 1.2×10^5 (CO_2) production cycles were performed in each simulation. For dual-component isotherms, at least 1×10^5 equilibration cycles and 3×10^5 production cycles were performed. All adsorption isotherms in SION-8P were obtained by placing non-interacting blocking spheres in the hydrophilic pores. Heats of adsorption at nonzero loading were computed from GCMC simulations based on energy/particle fluctuations, while those at zero loading were computed using Widom insertions [105].

Probability density plots of adsorbate positions of CO_2 and CH_4 in SION-8 were generated from NVT simulations, using the force fields described above. 10^5 initialization cycles were performed for each simulation, and adsorbate positions were recorded every 10 or more production cycles such that positions of at least 6×10^6 individual adsorbate molecules were recorded. The plots were generated using a Julia-based software package written by Dr. Cory Simon. NVT simulations of water used the TIP4P-Ew model for water [173].

Initial adsorption sites and geometries for DMF periodic DFT calculations were obtained from simulated annealing calculations of one DMF molecule within the canonical (NVT) ensemble, using the force fields described above. The initial temperature for the simulated annealing calculations was 313 K, and this temperature was decreased by 2 to 4 K every 10^5 Monte Carlo steps. The simulation continued until the temperature reached 1.0 K.

Remaining methods

Details of the following experimental methods can be found in the original publication [174]: synthesis of SION-8, single-crystal X-ray diffraction (SCXRD), variable-temperature (VT) and variable-pressure (VP) powder X-ray diffraction (PXRD), bulk characterization, sorption studies, and breakthrough experiments, as well as stiffness tensor calculation.

4.3 Results

Crystal structure description and bulk characterization

Self-assembly of Ca(II) ions with the H_4TBAPy ligand in an acidified mixture of DMF and water gave rise to the crystallization of $[Ca_2(TBAPy)(\mu_2{-}OH_2)_2]{\cdot}2DMF$, hereafter SION-8, with complete synthesis details in the published work [174]. The resulting structure features one-dimensional channels along the crystallographic *a* direction, with one-dimensional chains of Ca atoms, each 8-coordinated, along the same direction (Figure 4.1).

The phase purity of bulk SION-8 was confirmed through Le Bail fit of the powder X-ray diffraction (PXRD) pattern recorded with synchrotron radiation. The PXRD pattern is retained upon the immersion of SION-8 in water, proving its hydrolytic stability. The IR spectrum of SION-8, and in particular stretching vibrations of the carbonyl group at 1590 cm^{-1} and an intense absorption band of the extended aromatic ring at 1411 cm^{-1}, corroborate the incorporation of $TBAPy^{4-}$ ligand into the framework. Moreover, the broad band corresponding to the stretching vibrations of the carboxylic acid hydrogen at 3000 cm^{-1}, present in the spectrum of H_4TBAPy, is absent upon formation of SION-8, confirming that the $TBAPy^{4-}$ ligand is coordinated to Ca(II).

Stepwise activation

Thermogravimetric analysis (TGA) provides insight into the thermal stability of SION-8. The TGA profile of SION-8 (Figure 4.2) does not show an abrupt decrease in mass; instead, the mass loss occurs in several steps. The two initial segments of the TGA profile can be attributed to the release of guest DMF molecules residing within the pores; since the mass loss is not smooth in this region, we raise the hypothesis (see below for the experimental and computational evidence) that this release is stepwise: the DMF molecules trapped in the hydrophobic pores are removed first (below 520 K), while those remaining in the hydrophilic pores are removed at higher temperatures, up to 590 K. The decomposition of SION-8 occurs only once the coordinated H_2O molecules are removed between 590 and 670 K, suggesting their vital role in maintaining the framework integrity. The experimental mass loss values match those based on the formula derived from single-crystal X-ray diffraction (SCXRD), $[Ca_2(TBAPy)(\mu_2{-}OH_2)_2]{\cdot}2DMF$ (Table 4.1). The stepwise release of DMF molecules from the pores of SION-8, as strongly suggested by the TGA, prompted us to study the gradual activation of this material in an in situ SCXRD experiment.

An in situ SCXRD experiment provided proof of the stepwise activation of SION-8. Under vacuum, the unit cell volume, pore volumes, and excess electron density per pore were recorded at different temperatures (Figure 4.3). Upon temperature increase, the volume as well as the residual electron content of the hydrophilic pore change to a limited extent, despite the overall unit cell volume increase upon heating from 300 K to 400 K as a consequence of thermal expansion. At the same time, the hydrophobic pore, while increasing only slightly its volume of about 120 Å^3, loses its excess electron density from 36 electrons at 300 K to only

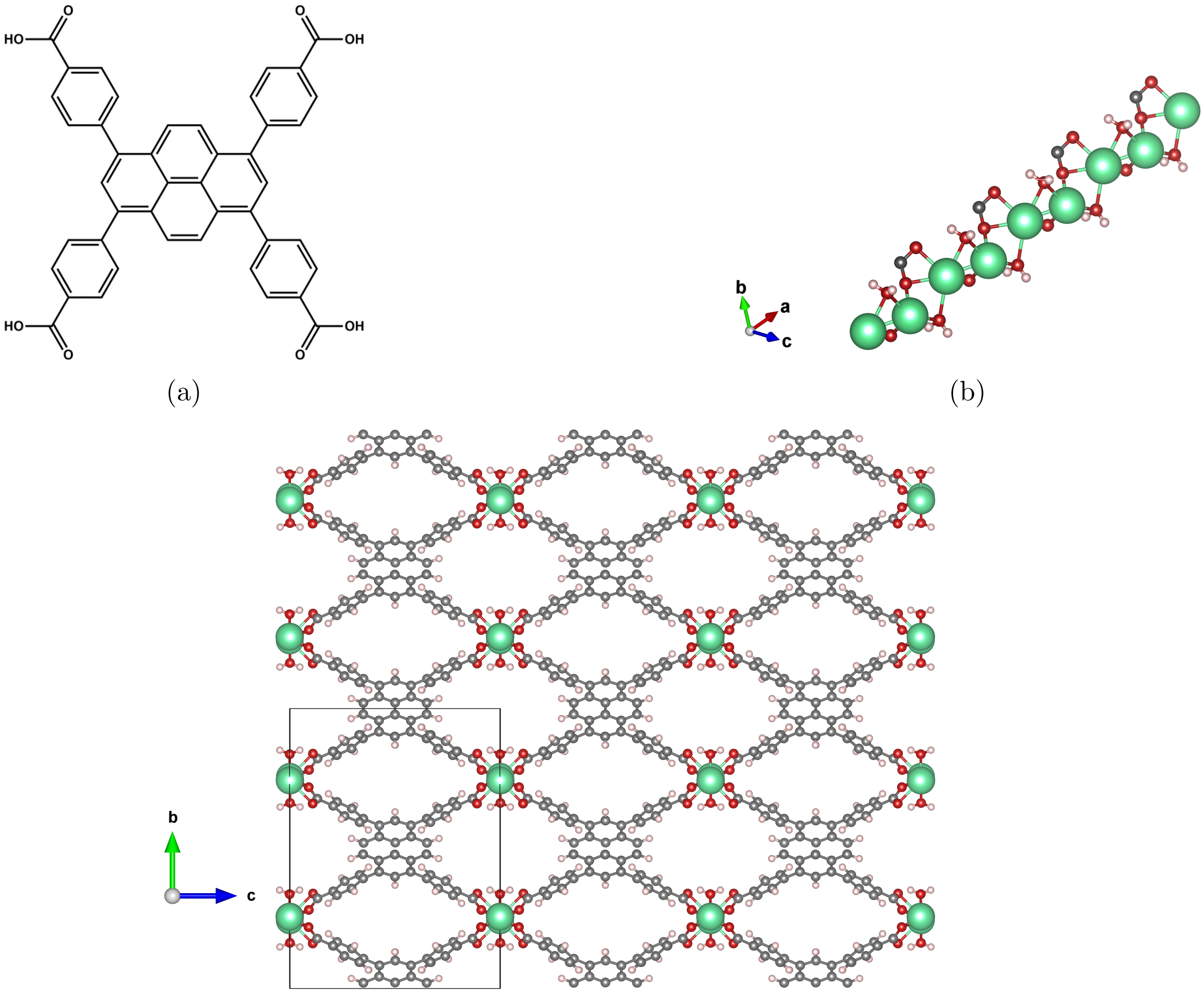

(a)

(b)

(c)

Figure 4.1: a) The tetracarboxylate ligand H_4TBAPy used in the synthesis of SION-8. b) One-dimensional chain of 8-coordinated Ca atoms present in the framework. c) Crystal structure of solvent-evacuated SION-8, with unit cell indicated lower left. Color scheme: C, gray; H, white; O, red; Ca, green.

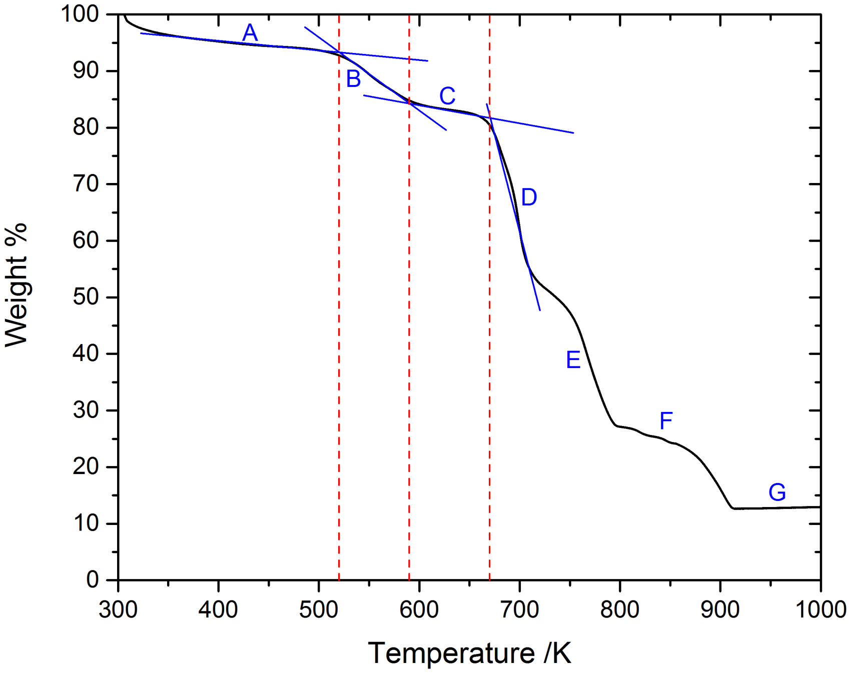

Figure 4.2: Thermogravimetric analysis of SION-8. Carrier gas: air. Letters A–G refer to the segments described in Table 4.1.

9 electrons at 400 K. Comparing these results to the electron count of DMF, it is observed in this temperature range that the hydrophilic pore contains approximately 1 molecule of DMF, irrespective of temperature, while the hydrophobic pore loses its 1 molecule of DMF upon heating, and at 400 K, it is virtually empty. Therefore, at 400 K and under vacuum, the selective partial activation of SION-8, limited solely to its hydrophobic pore, can be achieved. The partially-activated phase is referred to as SION-8P, while the phase where the pores of the framework are completely empty is named SION-8F (fully activated).

Periodic DFT calculations clarified the molecular-level interactions responsible for the partial activation of SION-8. The calculations show that when DMF is present in a hydrophilic pore, the incorporated water molecule rotates, as compared to the empty structure. This facilitates the formation of a hydrogen bond between the water hydrogen atom and the DMF oxygen atom (Figure 4.4). Accordingly, DMF has a significantly greater DFT-computed binding energy in the hydrophilic pore than in the hydrophobic pore: 105 kJ/mol and 66 kJ/mol, respectively. Importantly, all the MOF and DMF atoms are allowed to move during the relaxation; this is necessary for the structural relaxation that facilitates hydrogen bonding between DMF and the coordinated water molecule. In fact, the b dimension of the unit cell changes considerably when the structure is relaxed along with the DMF molecule

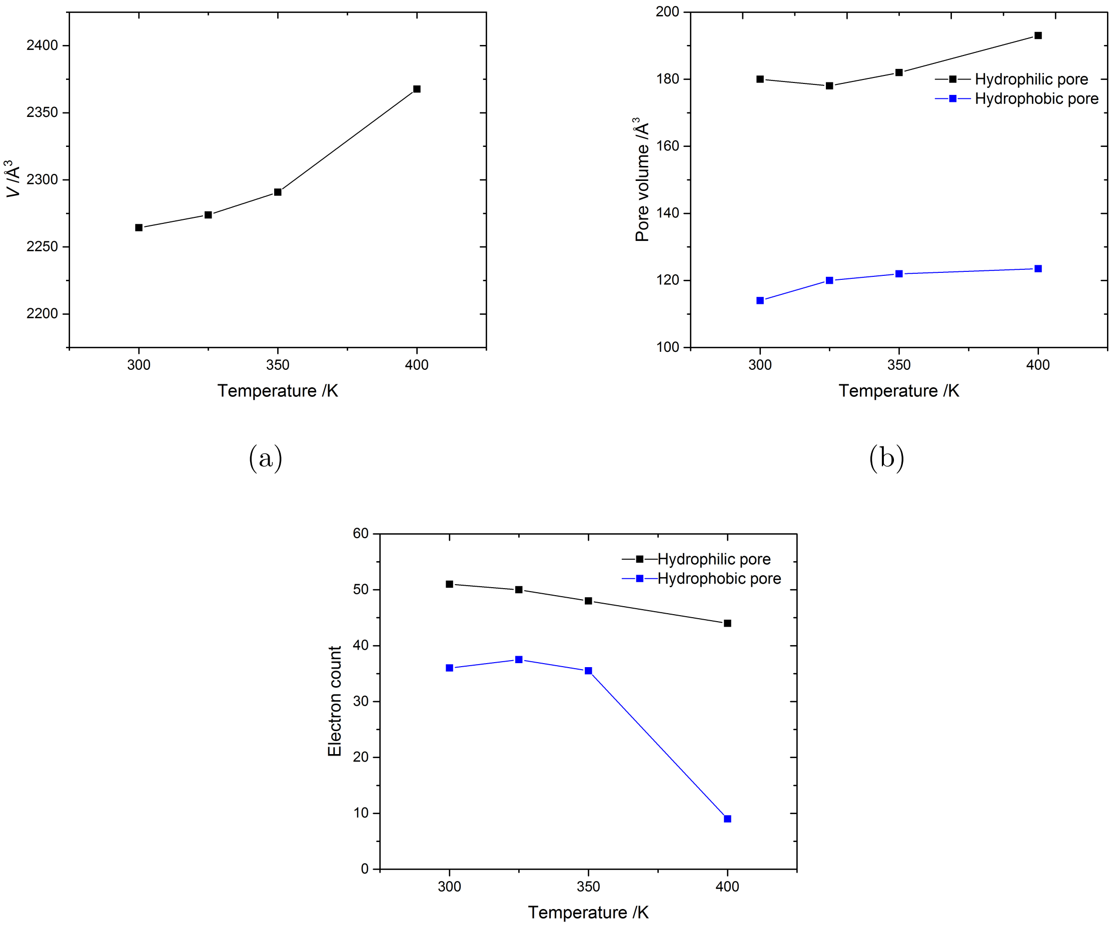

(a)

(b)

(c)

Figure 4.3: Stepwise activation of SION-8 under vacuum investigated with SCXRD. (a) Volume, V, of the unit cell of SION-8 plotted against temperature. (b) Volume of hydrophilic (black markers) and hydrophobic (blue markers) pores as calculated with the SQUEEZE procedure of the PLATON program suite [175]. (c) Excess electron density per pore found in both types of pores. Note that there are two hydrophobic and two hydrophilic pores in each unit cell.

Segment	Upper limit	Loss of mass observed from TGA	Loss of mass calculated from SCXRD	Description
A	520 K	7.2%	7.8%	DMF in the hydrophobic pores
B	590 K	7.9%	7.8%	DMF in the hydrophilic pores
C	670 K	4.3%	3.8%	Bridging H_2O molecules
D, E, F	915 K			Framework decomposition
G		87.0%	79.4%	Mineralized sample

Table 4.1: Gradual decrease in mass of a sample of SION-8 recorded in the TGA experiment compared to the values based on the formula derived from SCXRD.

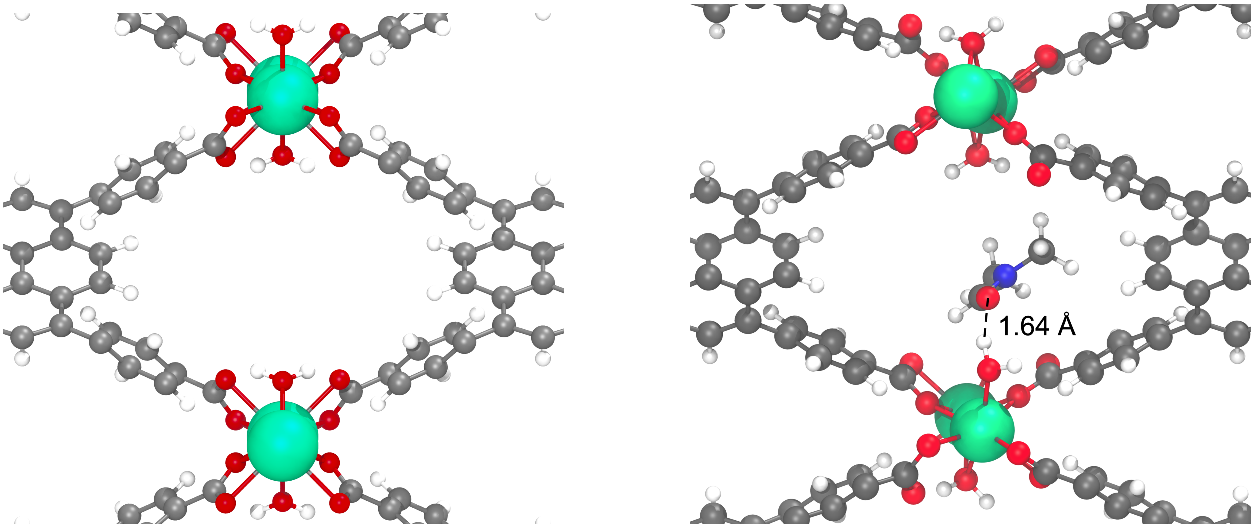

(a) (b)

Figure 4.4: a) Empty framework and b) result of DFT relaxation (MOF and DMF atoms allowed to move) of one DMF molecule in a hydrophilic pore of SION-8. The hydrogen bond between the framework and DMF is illustrated in b).

(Table 4.2).

The formation of this hydrogen bonding interaction helps explain why higher temperature is required to remove DMF from the hydrophilic pores. These findings are consistent with the partial activation of SION-8 observed in the in situ SCXRD experiment and the infeasibility of the full activation while maintaining the crystal's singularity.

The hydrophilicity/hydrophobicity of both pores of SION-8 was confirmed by exploring the interaction of water with the two different pores via molecular simulation. A greater

	Empty structure	Structure with DMF in hydrophilic pore
a	6.914 Å	6.757 Å
b	21.772 Å	20.544 Å
c	16.367 Å	16.680 Å

Table 4.2: Unit cell dimensions of DFT-relaxed structures.

number of water molecules were found to preferentially occupy the hydrophilic pore (with a contribution of 81.28% to the atom residence) compared to the hydrophobic pore, thus demonstrating the hydrophilic nature of the former. In addition, the hydrophilic pore showed a greater affinity (Q_{st} = -24(1) kJ/mol) to water at zero loading compared to the hydrophobic pore (Q_{st} = -14.90(2) kJ/mol).

Framework flexibility

The significant change in the unit cell's b dimension upon DMF adsorption, as observed in DFT calculations, alerted us to the possibility that SION-8 exhibits non-negligible flexibility. Accordingly, three computational approaches were undertaken in order to explore the flexibility of the fully-activated framework.

First, we examined the mechanical properties of the structure using DFT and computed the complete stiffness tensor, which according to the theory of elasticity, describes the mechanical properties of a crystal in the elastic regime, i.e. the region where a crystal recovers its original shape when the stress is removed [176]. The Young's modulus, i.e. the resistance of a material to uniaxial stress, was then extracted from it and presented in a geometrical form. The material is very stiff along the a-axis (Young's modulus 12.4 GPa), the parameter a corresponding to the particularly inflexible 1-dimensional Ca–O chains. The parameter c exhibits greater flexibility (Young's modulus 4.9 GPa); this represents the hydrophobic pore length. Since the Ca–O vs TBAPy^{4-} angle can assume a wide range of values, SION-8 exhibits the highest flexibility along the b axis (Young's modulus of 0.8 GPa). The anisotropy of Young's modulus, i.e. the ratio between its maximum and minimum values, of 15.5, places SION-8 among materials of intermediate anisotropy, along with those classified as reinforced wine-rack, e.g. MIL-140A. Typically, flexible MOFs, e.g. MIL-53, have a very large anisotropy factor ($\sim$100), while rigid MOFs, e.g. ZIF-8 and UiO-66, have an anisotropy factor of around 1 [177].

Second, DFT calculations were performed for SION-8 with a series of fixed values of the unit-cell dimension b, changing it up to ±10% and allowing the lattice parameters a and c, and the atomic coordinates of the entire structure, to relax to the minimum energy. The energy difference between these structures was subsequently assessed. Compressing or stretching the b dimension by up to 2 Å from the b corresponding to the minimum-energy structure incurs an energy penalty of less than 7 kJ/mol, which is less than the adsorption enthalpy of the gases studied (*vide infra*). Hence, it is suspected that, upon gas adsorption, adsorption-accommodating unit-cell deformations could occur.

Third, coefficients of thermal expansion were computed along the three crystallographic axes via a slow annealing NPT molecular dynamics simulation. SION-8F exhibits a negative thermal expansion along the c axis, a very weak positive thermal expansion along a, and a particularly strong positive thermal expansion along b, which provides still further evidence of the anisotropic framework flexibility, with greatest flexibility in the b direction.

Structural flexibility can lead to drastic alterations of the adsorption capacity of a porous material. In particular, flexibility in a MOF can either improve or reduce its performance, mainly because of the impact on the pore size and shape [68]. For this reason, the flexibility of SION-8 was studied as a function of the external gas pressure with SCXRD and PXRD chosen as experimental techniques to monitor the mechanical changes.

In the SCXRD experiment, a single crystal of SION-8P was subjected to a range of high pressures of N_2, CH_4, and CO_2, and the corresponding crystal structures were solved and refined at each pressure point of these isotherms. By calculating the electron density within the structural voids and comparing with the changes in unit cell parameters, we observe that the most noticeable structural changes in SION-8P are exerted by CO_2. The influence of CO_2 on SION-8P is two-fold: the uniform external pressure compresses the crystallites, and simultaneously, due to their porous nature, their pores are gradually filled with an increasing number of CO_2 molecules; as deduced from the observed pressure dependence of the unit-cell volume, the second phenomenon prevails. When the external pressure of CO_2 is increased, the parameter a elongates to a small extent and the parameter b, to a considerable extent, while the unit-cell dimension c shrinks; the magnitude of these deformations is analogous to that predicted from the Young's modulus calculation.

The variable-temperature PXRD experiment monitoring unit cell volume and parameters as a function of temperature shows a sudden 1.0% drop in unit cell volume upon heating between 325-360 K, which we associate with the partial desolvation of as-synthesized SION-8 and generation of SION-8P. This structural change is anisotropic as it is primarily realized along the b axis.

We therefore reason that, in order to accommodate guest species within its pores, SION-8 shrinks along c, elongates to a significant extent along b, and stays virtually invariant along a. Ultimately, the uptake of guest molecules exhibited by SION-8 is greatly enhanced by its flexibility; in order to accommodate CO_2 gas molecules, SION-8 anisotropically enhances its volume. In this respect, the behavior of SION-8 resembles that of Co(bdp) [178] and MIL-53(Cr) [179], although in both of these cases the accommodation of additional gas molecules is realized upon phase transitions toward the forms of higher capacity, rather than through continuous structural changes within the same phase.

Determination of force field for modeling CO_2 and CH_4 adsorption

Adsorption of different gases in the hydrophobic pores of SION-8P observed in the in situ SCXRD experiment prompted us to study bulk adsorption and adsorption phenomena on the molecular level via molecular simulation. Since SION-8 is a novel material, we tested the validity of several force fields for describing CO_2 and CH_4 adsorption in SION-8 by comparing with experimental data, which is presented fully in the next section. Three trial force fields were selected: 1) the Universal Force Field (UFF) [78], 2) DREIDING [79], and 3) that presented by Wu et al. [172], here referred to as Flex-ZIF, since it is a flexible force field formulated for ZIF-8. UFF and DREIDING were selected because they are generic force fields that are commonly used to model adsorption in nanoporous materials and in many cases show satisfactory accuracy [119, 180, 181]. Flex-ZIF was selected because it was developed for ZIF-8, a MOF that has small pores, as does SION-8.

To assess the three force fields, single-component CO_2 and CH_4 adsorption isotherms were computed in both SION-8F and SION-8P (Figure 4.5), as well as heats of adsorption Q_{st} in SION-8F (Table 4.3), and compared with experimental data. The Flex-ZIF force field overall gives the best quantitative and qualitative agreement with the experimental isotherms for both CO_2 and CH_4. All three force fields correctly reflect the stronger heat of adsorption of CO_2 compared with CH_4, but Flex-ZIF gives the closest quantitative agreement with experimental heats of adsorption.

	CO_2	CH_4
UFF	35.5 kJ/mol	22.7 kJ/mol
DREIDING	31.8 kJ/mol	22.1 kJ/mol
Flex-ZIF	24.3 kJ/mol	20.0 kJ/mol
Experimental	23.4 kJ/mol	16.0 kJ/mol

Table 4.3: Experimental and simulated (from Widom insertions) heats of adsorption of CO_2 and CH_4 in SION-8F at zero loading at 303 K.

Nonetheless, there is significant quantitative discrepancy between the heats of adsorption from Flex-ZIF and from experiment. Based on this observation, and in order to attempt to improve the accuracy of the Flex-ZIF force field for modeling adsorption in SION-8, a method developed by Kim et al. [182] was adopted, referred to here as the “energy-shifting method.” In the implementation of the energy-shifting method adopted in this work, one begins with a reference force field whose accuracy needs to be improved for a given nanoporous material. A classical simulated annealing simulation, using the reference force field, is used to find the minimum-energy binding site and corresponding binding energy. Then a high-accuracy ab initio method is used to find the minimum-energy binding site and compute the corresponding binding energy. The difference in the classically- and ab initio-determined binding energies is ΔE. Adsorption isotherms are again computed, using the reference force field but with the interaction energy in each Monte Carlo step shifted by ΔE. In this case, the reference force field is Flex-ZIF, and the energy-shifted version is referred to as “Flex-ZIF-shifted.” Since the two pores of SION-8 are chemically distinct, separate binding energies in each pore were computed, as well as loading in each individual pore. The reported Flex-ZIF-shifted

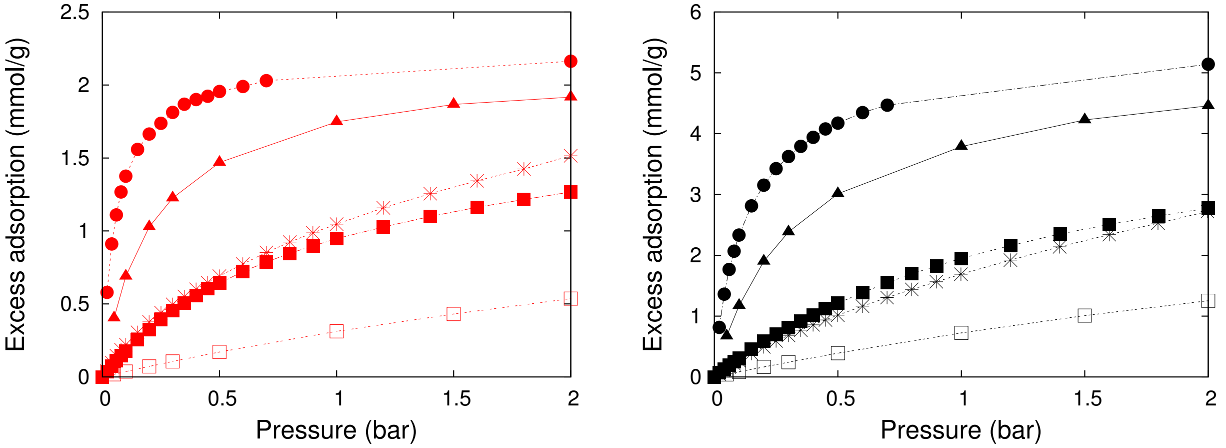

(a) CO_2 in SION-8P (b) CO_2 in SION-8F

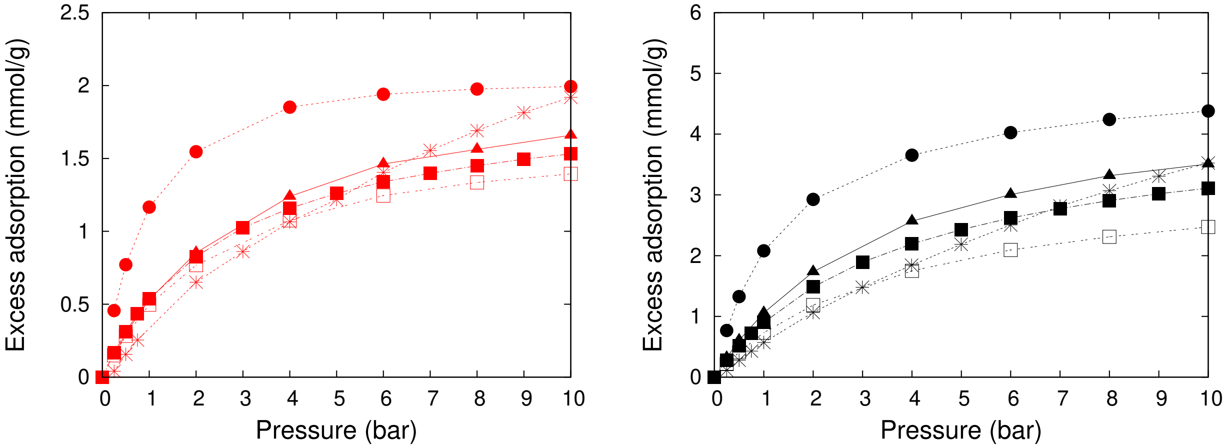

(c) CH_4 in SION-8P (d) CH_4 in SION-8F

Figure 4.5: CO_2 and CH_4 adsorption isotherms in SION-8P (red plots) and SION-8F (black plots) computed at 303 K using various force fields, with experimental isotherms for comparison. Key: UFF: circles; DREIDING: triangles; Flex-ZIF: filled squares; Flex-ZIF-shifted: empty squares; experiment: stars.

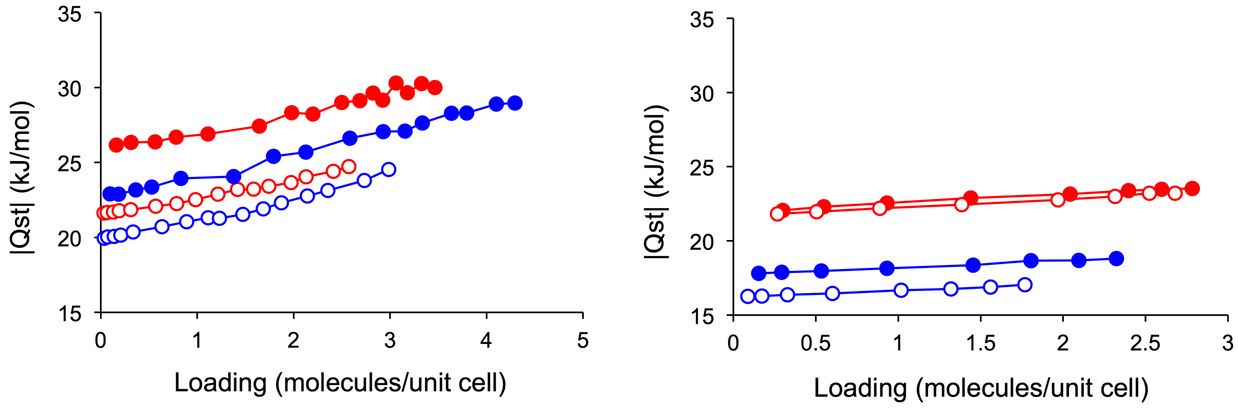

(a) CO_2 (b) CH_4

Figure 4.6: Isosteric heat of adsorption vs. loading for a) CO_2 and b) CH_4 computed using the Flex-ZIF and Flex-ZIF-shifted force fields, in both pore types. Key: hydrophobic pore: red; hydrophilic pore: blue; Flex-ZIF: filled symbols; Flex-ZIF-shifted: empty symbols.

isotherms for SION-8F are consequently the sum of the loading in the two pores. The binding energies, and resulting ΔE, used to compute the Flex-ZIF-shifted adsorption isotherms are shown in Table 4.4.

	DFT	Flex-ZIF	ΔE
CO_2, hydrophobic pore	-24.38 kJ/mol	-29.69 kJ/mol	5.31 kJ/mol
CO_2, hydrophilic pore	-27.02 kJ/mol	-31.46 kJ/mol	4.44 kJ/mol
CH_4, hydrophobic pore	-21.17 kJ/mol	-21.47 kJ/mol	0.30 kJ/mol
CH_4, hydrophilic pore	-16.90 kJ/mol	-18.70 kJ/mol	1.80 kJ/mol

Table 4.4: Binding energies used to compute the ΔEs for the Flex-ZIF-shifted force field.

Heats of adsorption were computed at various loadings in order to determine the effect of applying the energy-shifting method to the Flex-ZIF force field. As expected based on the binding energies, the heats of adsorption computed from Flex-ZIF-shifted are lower in magnitude than those from Flex-ZIF, in both pores and for both adsorbates, by an amount commensurate with the ΔE for each situation (Figure 4.6).

As evident from comparing the Flex-ZIF, Flex-ZIF-shifted, and experimental adsorption isotherms (Figure 4.5), the energy-shifting method overall does not improve the accuracy of the force field. We explored the reason for this by examining the minimum-energy binding sites (Figure 4.7). The minimum-energy binding site in the hydrophilic pore, as determined by classical simulation, is near the aromatic rings of one of the conjugated TBAPy linkers. DFT calculations yield the same result. There exist multiple identical sites in the unit

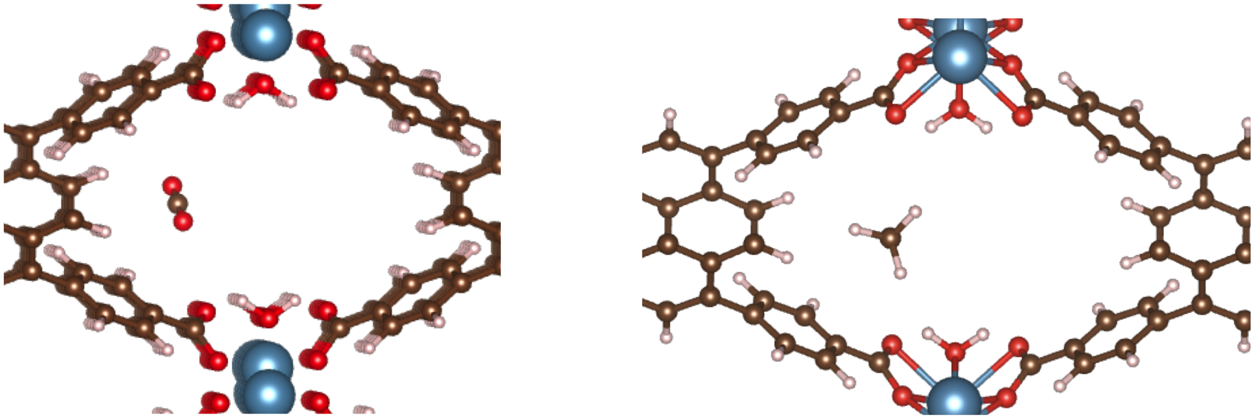
(a) CO_2 (b) CH_4

Figure 4.7: Minimum-energy binding sites of CO_2 and CH_4 in the hydrophilic channel, as determined by classical simulated annealing simulations using the Flex-ZIF force field. Color scheme: C: brown; H: white; O: red; Ca: blue.

cell. Furthermore, the minimum-energy binding site of CO_2 in the hydrophilic pore is not at the water molecule incorporated in the framework as we had hypothesized. In fact, by computing each framework atom type's energetic contribution (Lennard-Jones) to the total binding energy of CO_2 in the hydrophilic pore, we find that the hydrogen and oxygen water atoms contribute only 9.4% of the total binding energy (Table 4.5). The majority of the binding energy is contributed by framework carbon and hydrogen found in the TBAPy linkers. Thus since there is not one specific, relatively strong minimum-energy binding site, the energy-shifting method is not appropriate for SION-8 or similar materials. Therefore, we selected the Flex-ZIF force field to use for subsequent simulations.

Atom type	Contribution to binding energy
Ca	3.3%
C	61.9%
O in linker	11.7%
O in H_2O	4.1%
H in linker	13.7%
H in H_2O	5.3%

Table 4.5: Energetic contribution (Lennard-Jones) to CO_2 minimum-energy binding energy in hydrophilic pore by framework atom type.

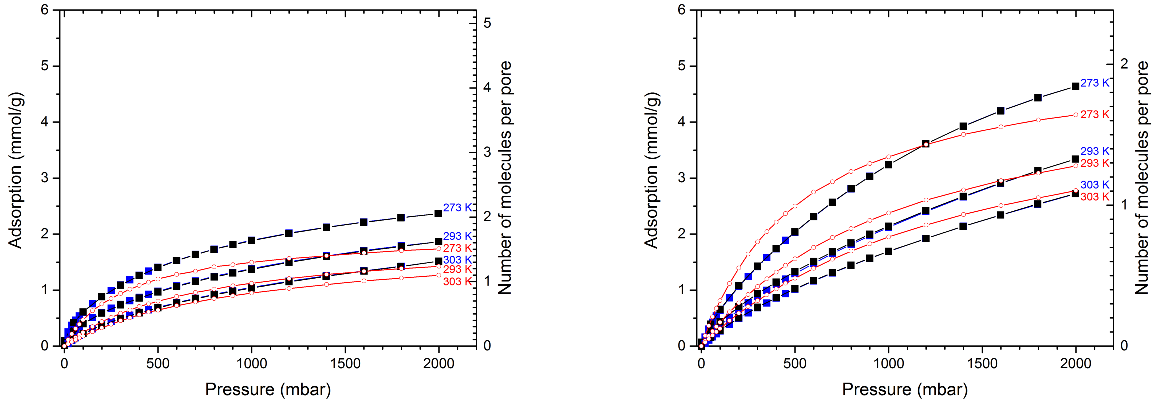

(a) CO_2 in SION-8P

(b) CO_2 in SION-8F

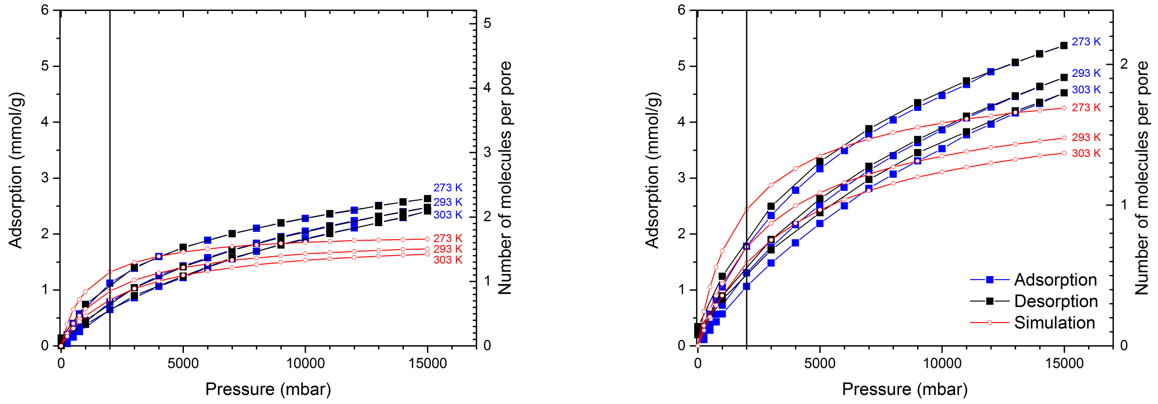

(c) CH_4 in SION-8P

(d) CH_4 in SION-8F

Figure 4.8: Experimental (blue, black) and simulated (red) CO_2 and CH_4 adsorption isotherms in SION-8P and SION-8F at 273 K, 293 K, and 303 K.

Single-component CO_2 and CH_4 adsorption

Adsorption isotherms, both from experiment and from GCMC simulations, were obtained for CO_2 and CH_4 at a range of near-ambient temperatures (Figure 4.8).

In all cases, above 1 bar, the sorption performance of SION-8F was nearly two times that of SION-8P. In contrast, at low pressures, the loading in the two materials is similar, since the heat of adsorption of both species in the hydrophobic pore is significantly greater than in the hydrophilic pore (*vide infra*). The flexibility of this MOF and the complex effect of guest adsorption on the framework, as described in the previous section, make this a challenging MOF to model computationally; thus, CO_2 and CH_4 isotherms computed from molecular simulations in both SION-8F and SION-8P deviate from experimental isotherms. However, the satisfactory agreement at low pressures led us to use this model for qualitative insight on adsorption.

In order to gain insights into the interactions of CO_2 and CH_4 with the surface of each pore type, we used molecular simulations to compute the heats of adsorption in each individual pore as well as in the fully activated structure as a function of loading (Figure 4.9). Both CO_2 and CH_4 are more strongly bound in the hydrophobic pore, and CO_2 is overall more strongly bound than CH_4. Interestingly, for both CO_2 and CH_4, the heat of adsorption of SION-8F is not a simple average of energies of interaction between the hydrophilic pore and the hydrophobic pore. The isosteric heats of adsorption Q_{st} were also calculated from the experimental isotherms (Table 4.6). In qualitative agreement with the simulation results, in SION-8P, the interaction between CO_2 and the pores is 1.3 times stronger than the analogous interaction of CH_4; in SION-8F, this ratio increases to 1.5. Consequently, the CO_2/CH_4 separation is expected to be more efficient with SION-8F.

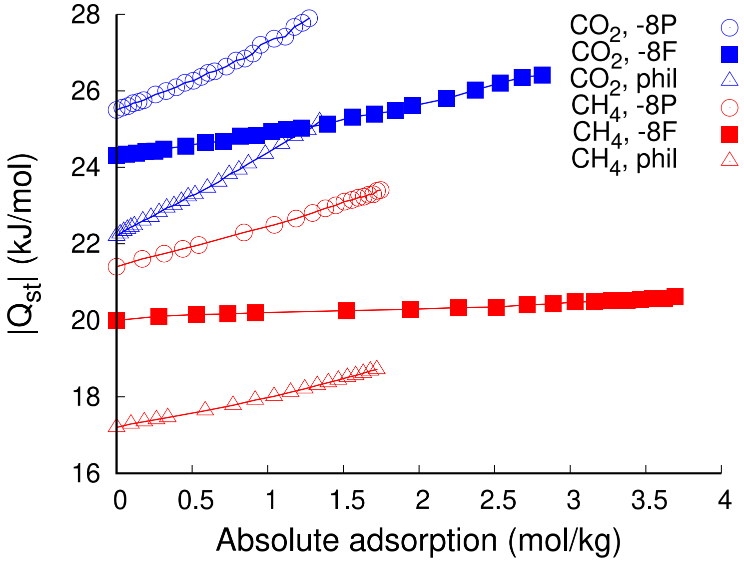

Figure 4.9: Heats of adsorption of CO_2 and CH_4 as computed from GCMC simulations (except those at zero loading, which were computed from Widom insertions) at 303 K. Loadings correspond to those considered in the adsorption isotherms. “-8P” refers to adsorption in SION-8P, “-8F” refers to adsorption in SION-8F, and “phil” refers to adsorption in the hypothetical SION-8 with only the hydrophilic pore available for guest adsorption.

The trends in the energy of interaction between adsorbates and pore surfaces in SION-8F compared to SION-8P can further be understood by examining the simulated probability density of CO_2 and CH_4 locations in both materials (Figure 4.10). CO_2 is only slightly more preferentially adsorbed in the hydrophobic pore compared to the hydrophilic one, thus reflecting the small difference in respective heats of adsorption. CH_4, however, shows greater preference for the hydrophobic pore than CO_2 does. This constitutes even further evidence

		SION-8P	SION-8F
CO_2	Simulation	25.5 kJ/mol	24.3 kJ/mol
	Experiment	28.4 kJ/mol	23.4 kJ/mol
CH_4	Simulation	21.4 kJ/mol	20.0 kJ/mol
	Experiment	21.4 kJ/mol	16.0 kJ/mol

Table 4.6: CO_2 and CH_4 isosteric heats of adsorption Q_{st} at zero loading for SION-8P (only hydrophobic pores accessible) and SION-8F (both pores accessible), calculated from experimental isotherms and from simulation (Widom insertions)

suggesting that, when the hydrophilic pore is available as in SION-8F, the ratio of CO_2 to CH_4 adsorbed shall increase, thereby increasing the CO_2/CH_4 selectivity.

CO_2/CH_4 separation

Prompted by the significantly different isosteric heats of adsorption in SION-8P and SION-8F, the CO_2/CH_4 separation performance of SION-8P and SION-8F was investigated further through both experiment and simulation. Breakthrough experiments, which provide additional information on the adsorption kinetics as compared with the equilibrium isotherms, were performed. Gas mixtures with a range of CO_2/CH_4 molar ratios were tested, including 90% CH_4 and 10% CO_2 (model composition of acid natural gas) and 50% CH_4 and 50% CO_2 (model composition of biogas). As can be seen from the recorded breakthrough curves (Figure 4.11), at each condition, CH_4 was released from the chromatographic column first, followed by CO_2 after a certain retention time spanning from several seconds to minutes. Adsorption capacities of SION-8P and SION-8F were calculated by integrating breakthrough curves and subsequently used to calculate CO_2/CH_4 dynamic breakthrough selectivities α using the following formula:

$$\alpha = \frac{q_{\mathrm{CO_2}}/q_{\mathrm{CH_4}}}{x_{\mathrm{CO_2}}/x_{\mathrm{CH_4}}}, \tag{4.2}$$

where q = adsorption capacity (mmol/g) and x = amount in moles. These selectitivies are summarized in Figure 4.12.

Dual-component mixture isotherms were computed for the same range of CO_2/CH_4 ratios considered in the breakthrough experiments. CO_2/CH_4 adsorption selectivities were calculated following the same formula as for the selectivities calculated based on the breakthrough experiments, with the CO_2 and CH_4 loading taken to be those at 1 bar, the pressure corresponding to the experimental breakthrough conditions (Figure 4.12). Qualitative agreement is observed between selectivities computed from simulation vs. experiment. The qualitative results in the remainder of this section (trends in selectivities with composition, temperature,

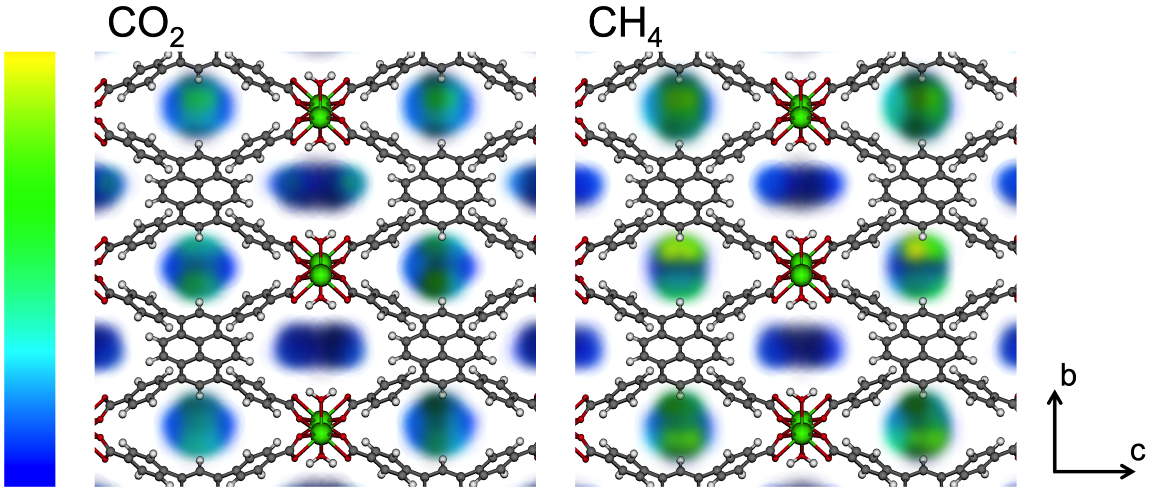

(a) View down channels

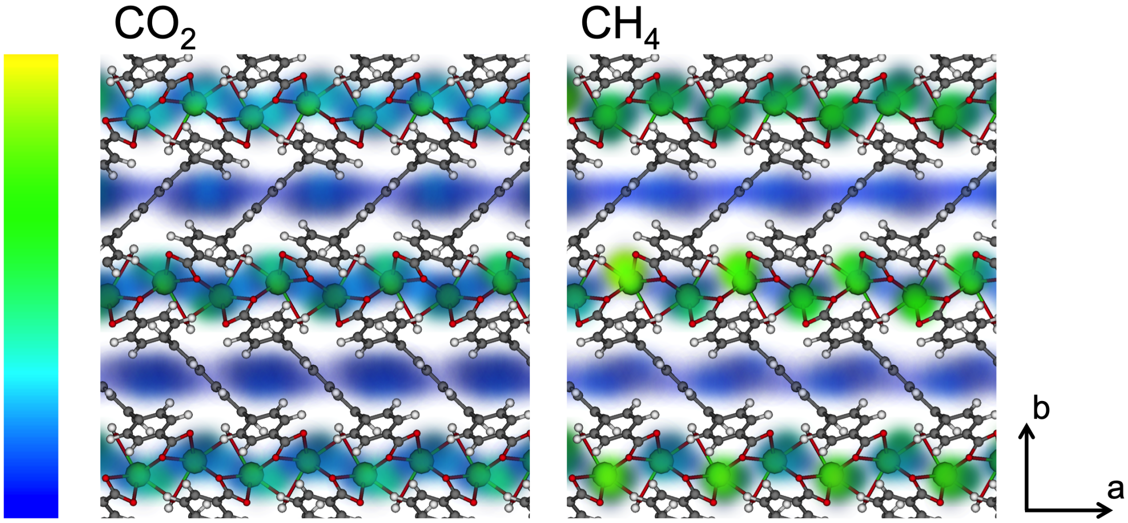

(b) View along side of channels

Figure 4.10: Probability density plots of adsorbate positions in SION-8F, generated from Monte Carlo NVT simulations with 2 molecules per unit cell, at 293 K. The color bar on the left denotes low (blue) to high (yellow) relative probability. CO_2 has 61.9% and 38.1% occupation in the hydrophobic and hydrophilic pores, respectively, while CH_4 has 66.1% and 33.9% occupation. a) Viewed down the channels and b) viewed along the side of the channels.

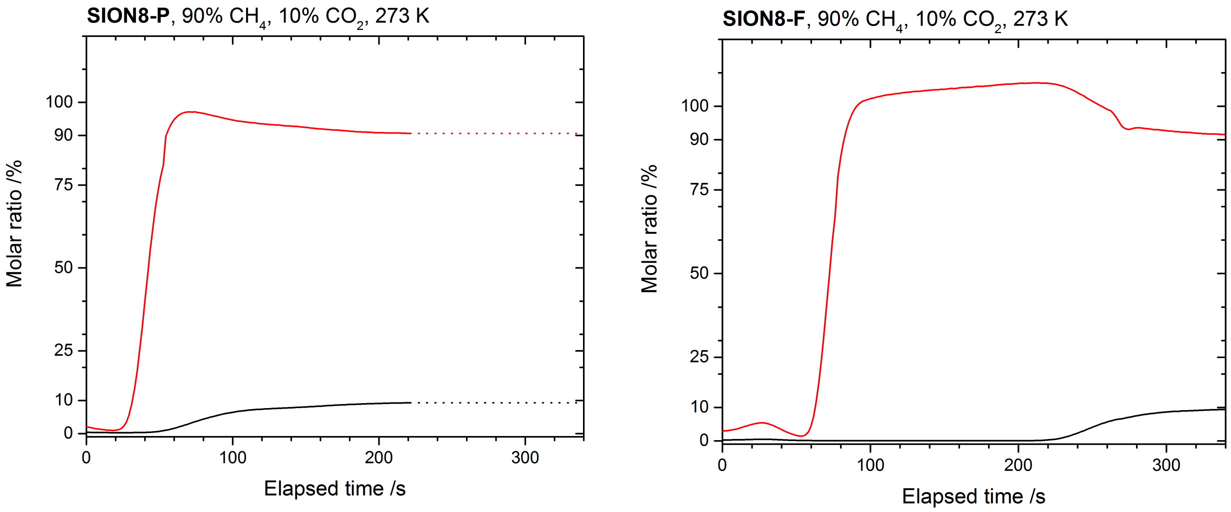

(a) SION-8P

(b) SION-8F

Figure 4.11: Experimental breakthrough curves for SION-8F and SION-8P recorded at 273 K for an initial mixture with molar ratio 90% CH_4 / 10% CO_2. CH_4: red lines; CO_2: black lines. While a range of temperatures and mixture molar ratios were measured, these curves are displayed to illustrative the selectivity of CO_2 over CH_4 and the improved selectivity of SION-8F over SION-8P.

and SION-8P vs. SION-8F) derive from both the simulation and experimental selectivities, while the quantitative results derive from the experimental selectivities.

In all cases, α is greater than 1, implying that, indeed in contact with the CO_2/CH_4 mixture, SION-8P and SION-8F selectively adsorb CO_2 over CH_4 (Figure 4.12). The CO_2/CH_4 separation is more efficient at lower concentrations of CO_2, which require lower adsorbed amounts of CO_2 for an equally efficient separation, and at lower temperature, which favors the increase in CO_2 adsorption capacity more as compared to that of CH_4 (Figure 4.12). The better performance of SION-8F compared to SION-8P, greater by 40% in the case of a 90% CH_4 / 10% CO_2 mixture at 323 K and by nearly 3-fold for the same gas mixture at 273 K (Figure 4.12), is a consequence of the different CO_2/CH_4 Q_{st} ratios exhibited by these materials as described in the previous section. SION-8F showed the best separation performance toward the 90% CH_4 / 10% CO_2 mixture, and it decreased toward more moderate values with increased concentrations of CO_2. Similar dependence of the selectivity on the CO_2/CH_4 mixture composition has been previously observed in other materials selective for CO_2, e.g. MIL-101(Al)-NH_2 [183], MIL-53(Al)-NH_2 [184], and CCP-1 [185].

With its CO_2/CH_4 dynamic breakthrough selectivity of 2.34 toward the 50% CH_4 and 50% CO_2 gas mixture at 303 K, SION-8F performs similarly well compared to other MOFs that are also based upon ligands with aromatic groups exposed to the pore surfaces (e.g. MOF-508b, α = 3 [186]; MIL-101(Cr), α = 3.6) [187]; however, MOFs containing unobstructed amino functionalization (e.g. MIL-101(Al)-NH$_2$, α = 6.3 [183]; MIL-53(Al)-NH$_2$, α = 45 [184]) or negatively-charged SiF_6^{2-} groups within the pores (e.g. SIFSIX-2-Cu-i, α = 51 [188]) perform better. Nevertheless, SION-8 has a tunable separation performance, which to the best of our knowledge has not been reported previously.

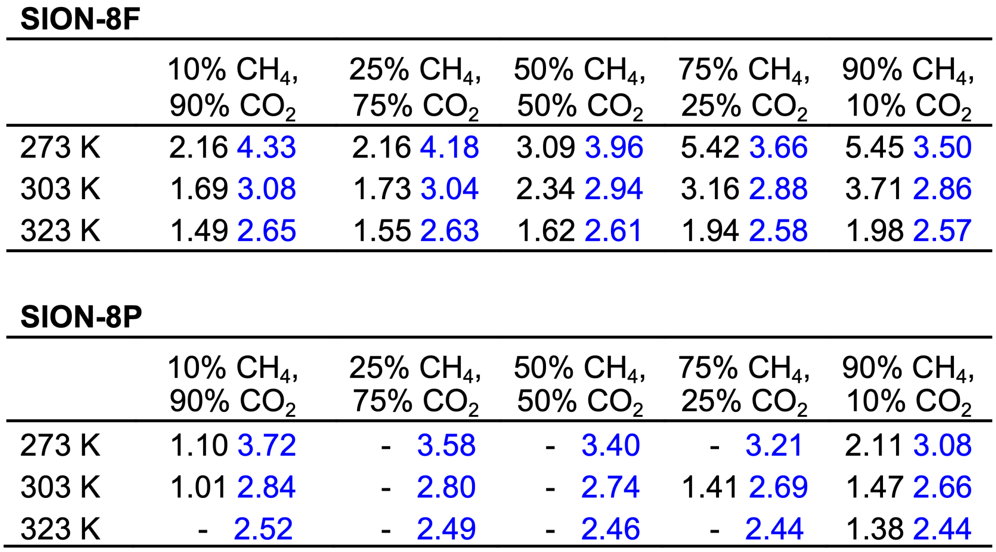

SION-8F

	10% CH$_4$, 90% CO$_2$	25% CH$_4$, 75% CO$_2$	50% CH$_4$, 50% CO$_2$	75% CH$_4$, 25% CO$_2$	90% CH$_4$, 10% CO$_2$
273 K	2.16 4.33	2.16 4.18	3.09 3.96	5.42 3.66	5.45 3.50
303 K	1.69 3.08	1.73 3.04	2.34 2.94	3.16 2.88	3.71 2.86
323 K	1.49 2.65	1.55 2.63	1.62 2.61	1.94 2.58	1.98 2.57

SION-8P

	10% CH$_4$, 90% CO$_2$	25% CH$_4$, 75% CO$_2$	50% CH$_4$, 50% CO$_2$	75% CH$_4$, 25% CO$_2$	90% CH$_4$, 10% CO$_2$
273 K	1.10 3.72	- 3.58	- 3.40	- 3.21	2.11 3.08
303 K	1.01 2.84	- 2.80	- 2.74	1.41 2.69	1.47 2.66
323 K	- 2.52	- 2.49	- 2.46	- 2.44	1.38 2.44

Figure 4.12: Experimental (black numbers) CO$_2$/CH$_4$ dynamic breakthrough selectivities α for SION-8F and SION-8P and selectivities α from simulations (blue numbers).

4.4 Conclusion

SION-8, a novel biporous MOF endowed with two chemically contrasting structural pores, the hydrophobic and the hydrophilic, was successfully synthesized and fully characterized. By judiciously altering the activation conditions, two functional materials were obtained: the partially-activated SION-8P and the fully-activated SION-8F. Due to their distinct pore environments, SION-8P and SION-8F showed different adsorption properties toward CO$_2$ and CH$_4$. Intrinsic structural flexibility, exhibited by SION-8 primarily along the *b*-axis as anticipated through computations, was found to be responsible for the structural adjustments allowing for the accommodation of guest solvent and gas molecules. The tunable CO$_2$/CH$_4$ separation performance was tested with breakthrough experiments at 1 bar and quantified by the CO$_2$/CH$_4$ dynamic breakthrough selectivity factors, α. At 273 K, SION-8P showed α of 2.11 toward the gas mixture composed of 90% CH$_4$ and 10% CO$_2$, while the respective value for SION-8F reached 5.45. A significant contrast between the values of Q_{st} and probability density of CO$_2$ and CH$_4$ locations in the two chemically different pores constitutes the rationale behind the different dynamic breakthrough selectivity factors in both materials. The discovery of SION-8 and the link between the macroscopic properties and the underlying chemistry of this material bring us closer to the rational design of new materials that can be used for a plethora of applications such as natural gas purification and other energy-related separations.

We propose several directions of future study to uncover other potentially useful applications of SION-8. Molecular simulations using a flexible model for the framework could be utilized in order to better capture the interplay between framework flexibility and gas adsorption. Diffusion behavior of CO_2 and CH_4 can be studied using molecular dynamics simulations in order to obtain dynamic insight into the molecular interactions affecting the CO_2/CH_4 separation process. SION-8's flexibility could be leveraged for sensing by incorporating the material in electromechanical sensors: upon adsorption of a gas, the expansion or contraction of the material is detected. Finally, SION-8 could be effective for multicomponent gas separation. To separate a three-component gas mixture, the two distinct pore types in SION-8 could be useful. Conceivably, components A and B could be adsorbed in the hydrophobic and hydrophilic pores, respectively, while component C is separated. This would represent an unusual and useful separation application.

Chapter 5

Understanding assembly of metal-organic frameworks

5.1 Introduction

As discussed throughout this dissertation, metal-organic frameworks (MOFs) are promising materials for various gas storage and separation applications that are relevant in clean energy. Moreover, an enormous variety of topologies, compositions, and surface properties can be achieved by varying the components of the frameworks. Because of this, in principle, one can tailor-make a MOF with optimal properties for a given application.

In reality, a major obstacle to tailor-making MOFs is that it is difficult to control the size and shape of MOF crystals. This lack of control is due to lack of understanding of the assembly process of MOFs. MOFs are most commonly synthesized solvothermally by heating the various components (metal salts and organic ligands) in solution [189]. The components self-assemble from solution to form a crystalline structure, but this self-assembly process is not well understood. The reaction temperature, time, solvent, and reagent concentration, among other parameters, can be varied to modify the resulting crystal's topology, size, and phase purity [190], but the effect of each parameter on the assembly process is generally not well characterized. Trial and error is usually needed to find reaction conditions that result in good-quality crystals of the desired form that are optimal for a given application. A fundamental understanding of the MOF assembly process would greatly facilitate the rational design of optimal materials for any of the applications discussed in this dissertation.

An illustrative example is MOF-74 [191] (Figure 5.1), the MOF that the work in this chapter focuses on. MOF-74 compounds and their derivatives demonstrate exceptional capacity for CO_2 adsorption and separation of CO_2 from H_2 or N_2 [192, 193], separations that are relevant in capture of CO_2 from flue gas. However, the preference of macroscopic MOF-74 crystals for growth along the crystallographic *c*-axis, resulting in anisotropic, needle-shaped crystals (Figure 5.2), is not ideal for incorporation of the MOF in a membrane for gas separation. Growth in the *a*-*b* plane would be preferable for membrane formation, so as to result in a continuous crystal with many channels perpendicular to the membrane, to maximize the diffusing gas's access to the pores.

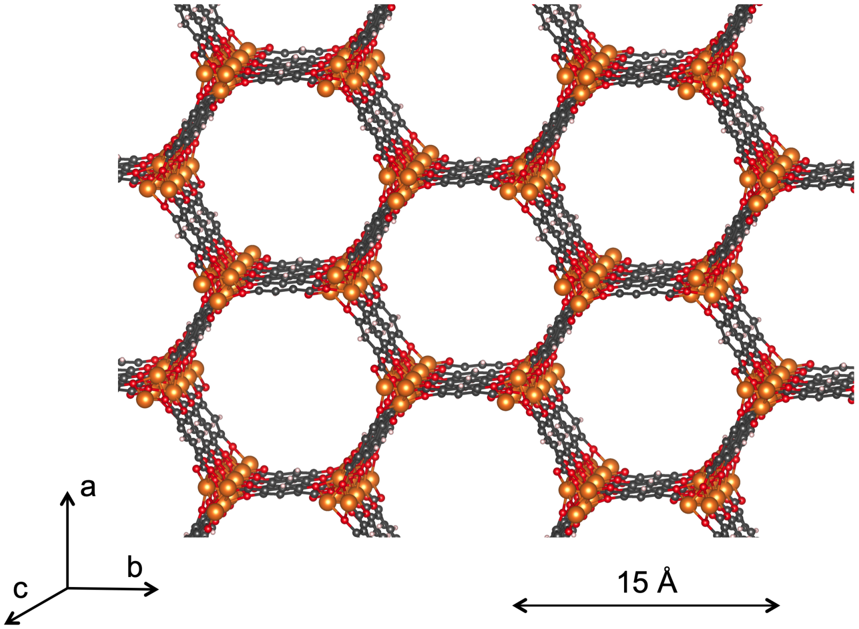

Figure 5.1: Crystal structure of M-MOF-74, also known as M_2(dobdc) (M = Mg in the structure shown; dobdc^{4-} = 2,5-dioxido-1,4-benzenedicarboxylate). The structure features 1-dimensional channels that run in the direction of the *c*-axis. Color scheme: C: gray; H: white; O: red; Mg: orange.

While the extent of study of MOF nucleation and growth has increased in the last decade, significant gaps of knowledge remain in fundamental understanding of nucleation and growth mechanisms and of the relation between reaction parameters and synthetic outcome [194, 195]. MOF-5, a zinc-based MOF, underscores the difficulties of studying MOF assembly. This MOF is thermodynamically stable and has a relatively simple cubic structure (illustrated in Figure 1.2 in the introduction), yet its assembly pathway is complex. One study suggested that the first solid phase formed in the crystallizing system is MOF-5 [196], while a later study showed that under various synthetic conditions, a complex series of reactions transform multiple metastable solid phases into the final product [197]. Furthermore, multiple synthesis routes for MOF-5 have been demonstrated, involving different zinc precursors, metal-ligand ratios, solvents, and reaction times and temperatures, each with potentially different assembly pathways. Another example of the challenge of mapping the enormous parameter space of MOF synthesis is a series of compositionally-identical ZIFs with distinct structures (ZIF-2, ZIF-3, ZIF-6, and ZIF-10). These ZIFs can be synthesized by small alterations to the reaction conditions, such as temperature and solvent [146]. Moreover, due to the great chemical and structural diversity of MOFs, it is difficult to generalize findings into conclusions that can guide syntheses in a more universal manner.

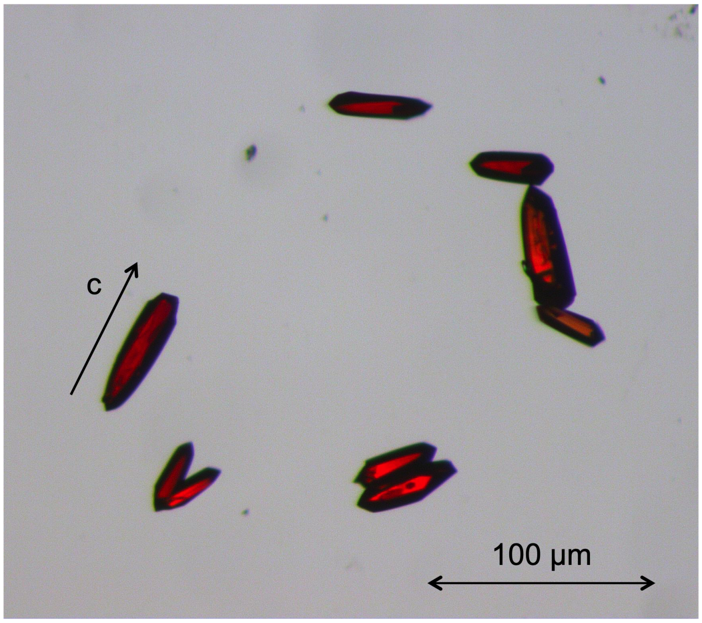

Figure 5.2: Optical microscope image of single crystals of Co-MOF-74. The preferred direction of growth is along the crystallographic *c*-axis.

Computational mechanistic studies face the challenges of large time and length scales needed to simulate nucleation and crystallization, as well as the difficulty of adequately modeling metal-linker bond formation and breaking [194]. Nevertheless, recent computational studies have established important insight on the role of solvent during MOF assembly (e.g. via DFT and molecular mechanics studies by Goesten et al. [198] and by Yang and Clark [199]), surface termination effects (e.g. via DFT calculations by Amirjalayer et al. [200]), kinetic effects (e.g. via kinetic Monte Carlo studies by Anderson et al. [201] and DFT studies by Cantu et al. [202]), and impacts of metal-ligand bond strength (e.g. via molecular dynamics studies with a continuum solvent by Umemura et al. [203]).

The work presented in this chapter takes a coarse-grained approach to gain fundamental mechanistic insights on MOF nucleation. Using a simplistic model combined with enhanced sampling techniques (vide infra) allows us to get around time-scale issues in order to study the rare event of nucleation. As nucleation is an ubiquitous phenomenon occurring in many natural processes, we draw upon a well-established body of work on theories of nucleation and computational techniques to study it [204].

In this work, we focus on MOF-74, and our approach is to characterize MOF-74's assembly pathway, or a description of the structures that self-assemble throughout this process. Elucidating the assembly pathway is valuable because if the assembly process is well understood, then we may be able to determine reaction conditions that favor an assembly pathway that results in MOF crystals of the desired form. Self-assembly, a non-equilibrium process, can be described as near or far from equilibrium [205]. In a "near-equilibrium" pathway, the resulting structure is the thermodynamically stable shape; the assembly process is dominated by thermodynamic factors. Physical examples include the self-assembly of NaCl crystals [206] and some instances of protein crystallization (e.g. [207]). In contrast, in a "far-from-equilibrium" pathway, the resulting structure is not a thermodynamically stable structure; the assembly process is dominated by dynamics. Physical examples include formation of gels [208] and fractal diffusion-limited aggregates [209].

In this work, the thermodynamic assembly pathway of MOF-74 is characterized using simulations on a simple lattice model. A 3-dimensional hexagonal lattice is used to represent MOF-74. Results from the hexagonal lattice are compared with those from a cubic lattice, which corresponds, for example, to MOF-5. The cubic lattice provides a reference point with which to compare the hexagonal geometry, since the cubic geometry has no preferred axis for growth. A square lattice is also examined in order to better visualize cluster characteristics. The use of a lattice model keeps constant the geometry of growing MOF crystals and allows the isolation of the effect of geometry on assembly. The effect of temperature on the assembly pathway is also investigated.

We find that critical clusters on the hexagonal lattice are elongated in the c-direction, the direction of macroscopic elongation. The thermodynamic reason for this is the different surface tension energies on different surfaces of a cluster.

5.2 Methods

Free-energy curves

A lattice model is used to represent the system comprising the MOF crystallizing from solution. In this model, a lattice site is located on each vertex of the MOF-74 structure, as illustrated in Figure 5.3. This 3-dimensional hexagonal lattice is a simplistic representation of MOF-74 that captures the hexagonal nature of the structure. Periodic boundary conditions are used in order to simulate an infinite structure. Similar lattices are constructed for cubic and square systems (see Figure 5.3).

Each site exists in one of two states: occupied by a MOF building block, which corresponds to the crystalline phase, or unoccupied by a MOF building block, which corresponds to the solution phase (Figure 5.4). This lattice model is one-component: all components, or MOF "building blocks," are identical. In this model, a "cluster" refers to a portion of MOF crystal and is defined as a group of connected (nearest-neighbor) occupied sites.

With the square lattice, a simulation box of 100×100 lattice sites is used, and with the cubic and hexagonal lattices, the simulation box is 32×32×32 lattice sites. These simulation box sizes were determined to be large enough that clusters do not span the simulation box, as a cluster interacting with itself would introduce artifacts. This was determined by visual inspection.

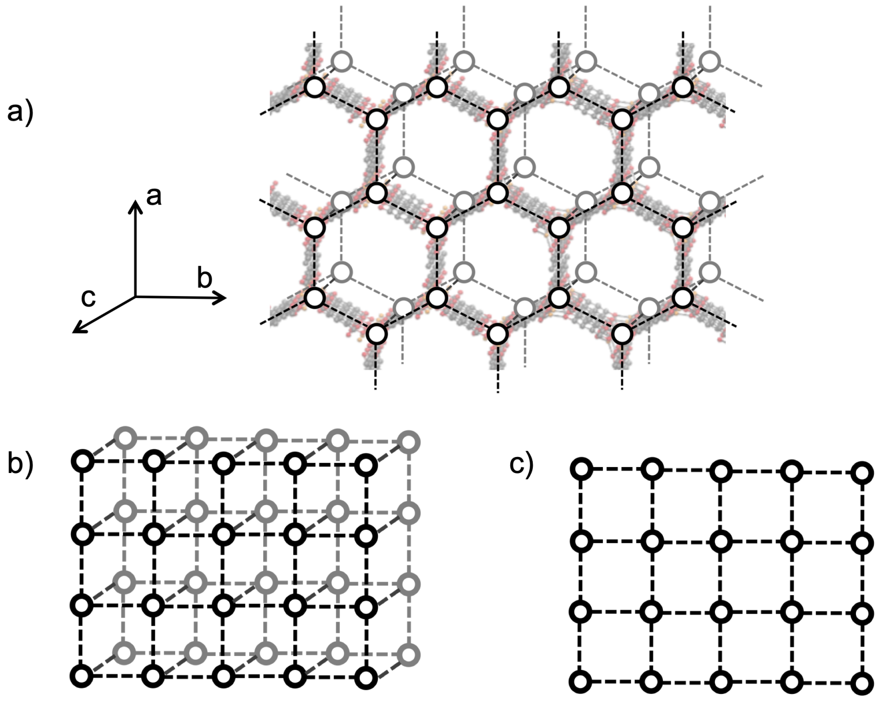

Figure 5.3: Illustration of the a) 3-dimensional hexagonal lattice model overlaid with the crystal structure of MOF-74, b) cubic lattice, and c) square lattice. Circles represent lattice sites; nearest-neighbor sites are connected with dashed lines. All nearest-neighbor distances are equal.

Ising model

We define the energy of the system using the Ising model:

$$E = -J \sum_{\langle i,j \rangle} s_i s_j - h \sum_i s_i, \tag{5.1}$$

where s_i indicates the state of the site: +1 for occupied, −1 for occupied. $\langle i, j \rangle$ indicates a sum over nearest-neighbor sites, J represents the interaction energy between two sites, and h represents a chemical potential that can be tuned to favor the crystalline phase. Note that we work in the spin-spin representation, rather than the lattice gas representation, of the Ising model.

The Ising model is appropriate for this study because it is a simple model that can describe the essence of nucleation and growth, as has been shown in various studies [210–213]. Furthermore, the Ising model differentiates between the square, cubic, and hexagonal geometries, via the sum over nearest neighbors.

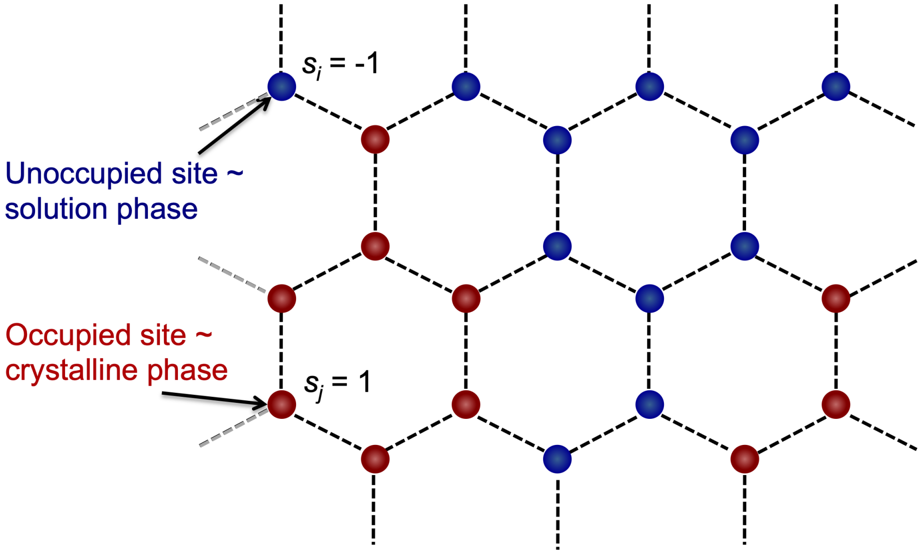

Figure 5.4: A 2-dimensional slice of the 3-dimensional hexagonal lattice. Each site exists in one of two states: occupied by a MOF building block, which corresponds to the crystalline phase and $s_i = +1$, or unoccupied by a MOF building block, which corresponds to the solution phase and $s_i = -1$. Occupied sites are depicted as red and unoccupied sites as blue, for the remainder of this chapter.

Monte Carlo

Monte Carlo simulations in the canonical ensemble are performed to mimic the assembly of the MOF from solution.

Single spin-flip Monte Carlo moves are used: a lattice site is chosen at random and its state is reversed, with energy ΔE given by Equation 5.1. Moves are accepted according to the Metropolis probability [69]: $\min[1, e^{-\beta \Delta E}]$.

After repeating many times, the Boltzmann distribution is sampled, making this sampling procedure appropriate for determining the thermodynamic assembly pathway.

Umbrella sampling

Umbrella sampling is used to compute free-energy curves for nucleation [85]. Such a non-Boltzmann sampling technique is needed in order to obtain adequate sampling of the system near the top of the curve, since this corresponds, at the conditions studied, to a rare event where the system would, under Boltzmann sampling, rarely exist.

Cluster size N is used as the reaction coordinate. A critical cluster has maximum free energy and has size N^*. This reaction coordinate is a logical choice for tracking the growth of MOF clusters. Furthermore, cluster size has been shown to be an important reaction coordinate in various studies of nucleation in the Ising model [214, 215].

The distribution of sizes of clusters is recorded in each umbrella-sampling window. Windows have width 8, with an overlap of 4 with neighboring windows.

The system is constrained to a certain window using hard-wall sampling: every 1 to 3 "sweeps" of Monte Carlo moves, we check if the largest cluster in the system is within the window bounds. If so, the simulation continues; if not, the system is returned to its state at the last time that hard wall sampling was performed. One sweep is equal to the number of lattice sites in the simulation box.

Data from all umbrella-sampling windows are combined using the weighted histogram analysis method (WHAM) [216] to give a single free-energy curve. Compared to stitching free-energy curves in each window by hand (by making the curves match at arbitrary overlapping points), WHAM results in a smoother curve (Figure 5.5). The combining method also affects the height of the free energy barrier.

The free-energy curves are shifted such that $\Delta E(N=0)=0$.

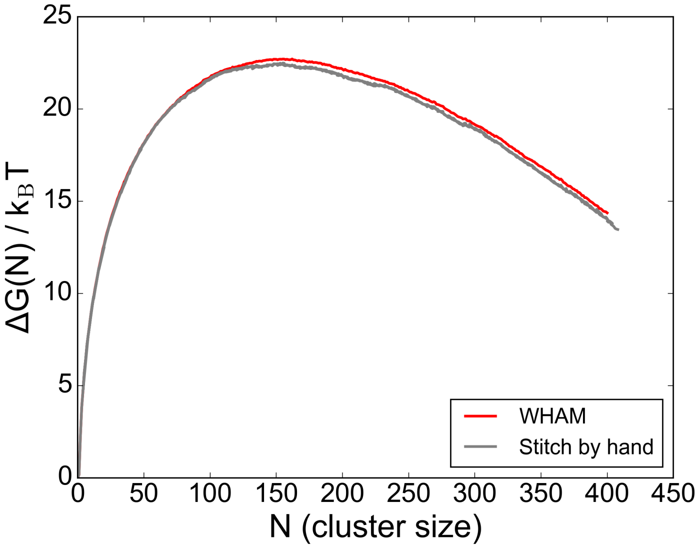

Figure 5.5: Free-energy barrier to nucleation for the square lattice Ising model at 60% T_c ($J/k_BT = 0.71$, $h/k_BT = 0.071$), generated using two different methods for combining histograms from each umbrella-sampling window. Given the same data, WHAM results in a smoother curve and a slightly different barrier height compared with stitching together windows by hand.

Analyses of clusters of a single size (see Figures 5.8, 5.9, 5.12, 5.13, and 5.14) were carried out by performing a simulation in one umbrella-sampling window, collecting data for only clusters of that size.

In computing free energy curves, at least 2×10^4 initialization sweeps and 2×10^4 production sweeps of Monte Carlo moves were performed per umbrella-sampling window. Data are collected only in the production sweeps. In simulations collecting data on clusters of one size, at least 5×10^5 initialization sweeps and 5×10^5 production sweeps were performed.

Convergence of histograms (of cluster size) in each window was confirmed by plotting the first 50 percent of production data along with the last 50 percent of production data. Histograms equivalent within statistical error show that sufficient sampling was performed.

Free-energy curves for the square lattice were benchmarked against results from Hedges et al. [215] and found to agree.

Values of Ising parameters

For each lattice type, two temperatures were studied, corresponding to approximately 60% and 30% of the critical temperature. Different temperatures are implemented by changing the value of the Ising parameter J. Values of h equal to approximately half of J were used, except in the square lattice, where values of h are equal to approximately 10% of J. All values of J and h used in the simulations in this work are listed in Table 5.1.

These values of J and h were chosen so that the free energy barriers would have heights of approximately 20 to 100 $k_{\mathrm{B}}T$, magnitudes that are tractable in simulation.

Lattice type	**Temperature**	$J/k_{\mathrm{B}}T$	$h/k_{\mathrm{B}}T$
Square	60% T_{c}	0.71	0.071
	30% T_{c}	1.47	0.14
Cubic	60% T_{c}	0.37	0.20
	30% T_{c}	0.74	0.41
Hexagonal	60% T_{c}	0.50	0.24
	30% T_{c}	0.89	0.49

Table 5.1: Values of J and h used in simulations.

The critical temperature of the 2-dimensional square Ising model has been found analytically to be 2.269 J/k_{B} [85], and that of the 3-dimensional cubic Ising model has been found numerically to be 4.5 J/k_{B} [217, 218]. We estimated via simulation that the critical temperature of the 3-dimensional hexagonal lattice is 3.4 J/k_{B} (Figure 5.6).

Methods for quantitative characterization of cluster shape

Cluster shape is characterized quantitatively using two measures. The first measure is the anisotropy parameter A,

$$A = I_{+}/I_{-} - 1, \tag{5.2}$$

where I_{+} and I_{-} are the largest and smallest, respectively, principal moments of inertia.

The moment of inertia I describes a body's resistance to rotational acceleration about an axis:

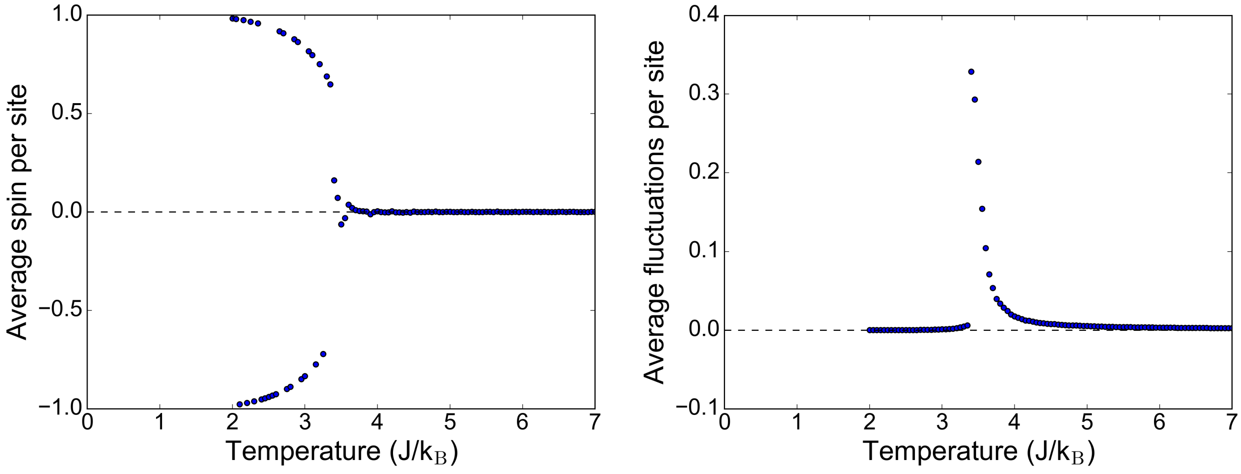

(a) (b)

Figure 5.6: a) Average magnetization vs. T for the 3-dimensional hexagonal lattice with h = 0. The critical temperature is the temperature at and above which spontaneous magnetization does not exist. b) Average squared fluctuations vs. T with $h = 0$. There is a near-discontinuity at the critical temperature. A true discontiunity would be observed in an infinite system.

$$I = mr^2, \tag{5.3}$$

where m is the mass of the body and r is the radius of rotation about an axis.

On the x, y, z plane, I can be expressed as an integral over mass, or equivalently,

$$I = \int_V \rho(x, y, z)[I]dV, \tag{5.4}$$

where $\rho(x, y, z)$ is the density of the body, dV is a volume element, and $[I]$ is the inertia tensor:

$$[I] = \begin{pmatrix} I_{xx} & -I_{xy} & -I_{xz} \\ -I_{yx} & I_{yy} & -I_{yz} \\ -I_{zx} & -I_{zy} & I_{zz} \end{pmatrix}. \tag{5.5}$$

The diagonal elements, I_{xx}, I_{yy}, and I_{zz}, are the moments of inertia about the x, y, and z axes, respectively, and the off-diagonal elements are the xy, yz, and xz products of inertia for a discrete system of N particles of identical mass:

$$
\begin{aligned}
I_{xx} &= \sum_{i=1}^{N} y_i^2 + z_i^2 \\
I_{yy} &= \sum_{i=1}^{N} x_i^2 + z_i^2 \\
I_{zz} &= \sum_{i=1}^{N} x_i^2 + y_i^2 \\
I_{xy} = I_{yx} &= -\sum_{i=1}^{N} x_i y_i \\
I_{xz} = I_{zx} &= -\sum_{i=1}^{N} x_i z_i \\
I_{yz} = I_{zy} &= -\sum_{i=1}^{N} y_i z_i
\end{aligned}
\tag{5.6}
$$

The eigenvalues of $[I]$ are the principal moments of inertia of the body, and the eigenvectors are the principal axes of inertia. These entities describe the distribution of mass in the body. In particular, they quantify the degree and direction of elongation of the body. I_-, the smallest principal moment of inertia, corresponds to the direction in which the body is longest. The eigenvector corresponding to this eigenvalue I_- points in the direction of elongation.

Hence the anisotropy parameter $A = I_+/I_- - 1$ is equal to 0 for a perfectly isotropic (spherical) cluster; deviation from 0 reflects the degree of elongation. This anisotropy parameter depends solely on the cluster shape and is not defined by the underlying lattice.

The second measure of cluster shape describes the length of a cluster in the a, b, and c directions, by comparing coordinates of sites in the cluster with the center of mass ("com") of the cluster:

$$
\begin{aligned}
I_a &= \left\langle (x - x_{\mathrm{com}})^2 \right\rangle \\
I_b &= \left\langle (y - y_{\mathrm{com}})^2 \right\rangle \\
I_c &= \left\langle (z - z_{\mathrm{com}})^2 \right\rangle
\end{aligned}
\tag{5.7}
$$

For simulations in one umbrella sampling window, collecting data for clusters of one certain size, the quantities A, I_a, I_b, and I_c are recorded every sweep at the end of which there exists a cluster of this size.

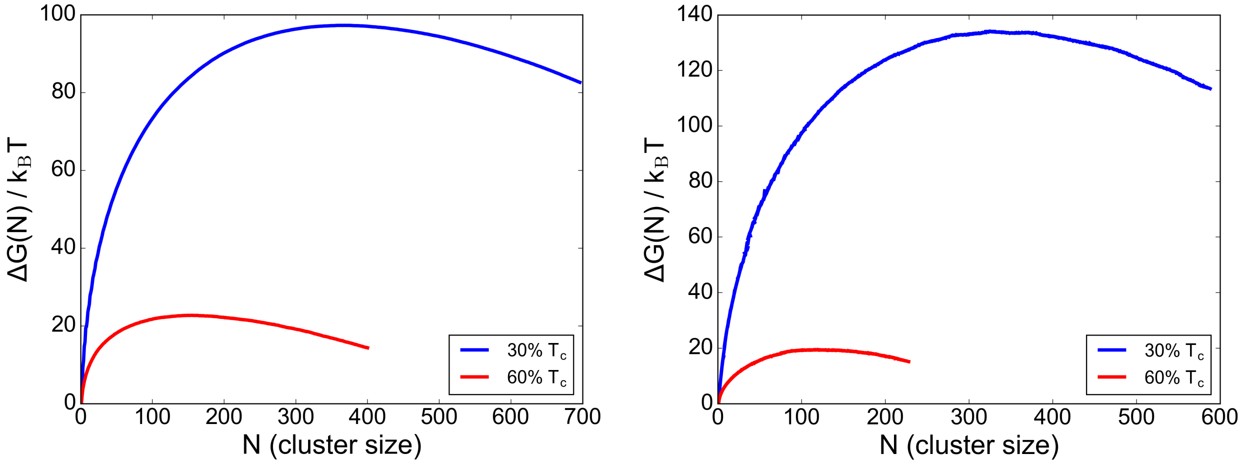

(a) Square lattice

(b) Cubic lattice

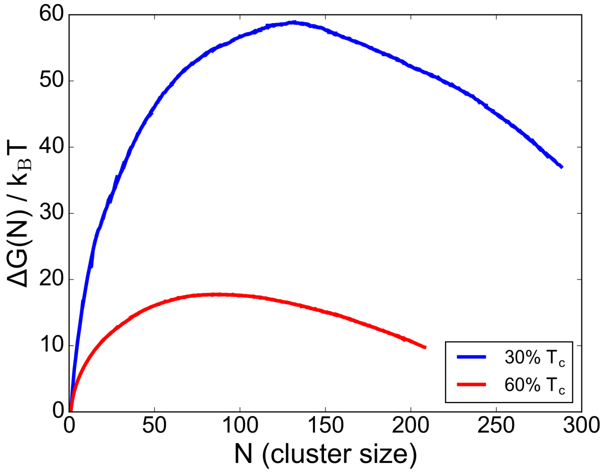

(c) Hexagonal lattice

Figure 5.7: Free-energy barrier to nucleation for the a) square, b) cubic, and c) hexagonal lattices at 60% (red lines) and 30% (blue lines) of critical temperature. These free-energy curves provide a framework for understanding the equilibrium preference for shape, since they are computed using umbrella sampling, so the system remains at the most thermodynamically favored configuration at every point along the assembly pathway.

5.3 Results

Free-energy curves

As the first step towards the goal of mapping out the thermodynamic assembly pathway, free-energy barriers to nucleation were computed (Figure 5.7).

The height of the free energy barrier is greater at lower temperature, for all lattices.

This agrees with classical nucleation theory (CNT) predictions [219]. The hexagonal lattice has a lower free energy barrier than the cubic lattice. This finding also agrees with CNT predictions and can be seen by considering a CNT expression for the free energy of formation of a three-dimensional isotropic cluster of size N:

$$\Delta G(N) = -\Delta g N + \sigma A, \tag{5.8}$$

where Δg is the bulk free energy difference between the two bulk phases, σ is the surface tension between the two phases, and A is the cluster's surface area, $A \sim N^{2/3}$. By finding the value of N that maximizes this function, it can be shown that the barrier height ΔG^* depends on σ and Δg as follows:

$$\Delta G^* \sim \frac{\sigma^3}{(\Delta g)^2}. \tag{5.9}$$

σ is proportional to the number of broken bonds, or number of neighboring sites of the opposite state, per site. Every site on the hexagonal lattice has five neighboring sites, while every site on the cubic lattice has six. Therefore, in the case of a nucleating cluster, it is expected based on CNT that the height of the free energy barrier to nucleation will be lower on the hexagonal lattice.

From the free-energy curves, we determined the critical cluster size in each system (Table 5.2).

	$T = 0.6T_\mathrm{c}$	$T = 0.3T_\mathrm{c}$
Square	155	369
Cubic	119	325
Hexagonal	85	131

Table 5.2: Size of critical clusters in each system studied.

Qualitative exploration of cluster shape

In the investigation of anisotropic growth of MOF-74, characterizing cluster shape is of interest. To begin, we explored qualitatively the shapes of clusters of critical size: we visualized individual instances of critical clusters (Figure 5.8) and for the square lattice, visualized the effect of temperature on cluster shape (Figure 5.9). These analyses show that average cluster shape transitions from square-like to more circular with temperature.

Investigation of square-to-circular cluster transition

To better understand the shape transition from square to circular with increasing temperature observed in simulation (Figure 5.9), we consider the effects of fluctuations in the

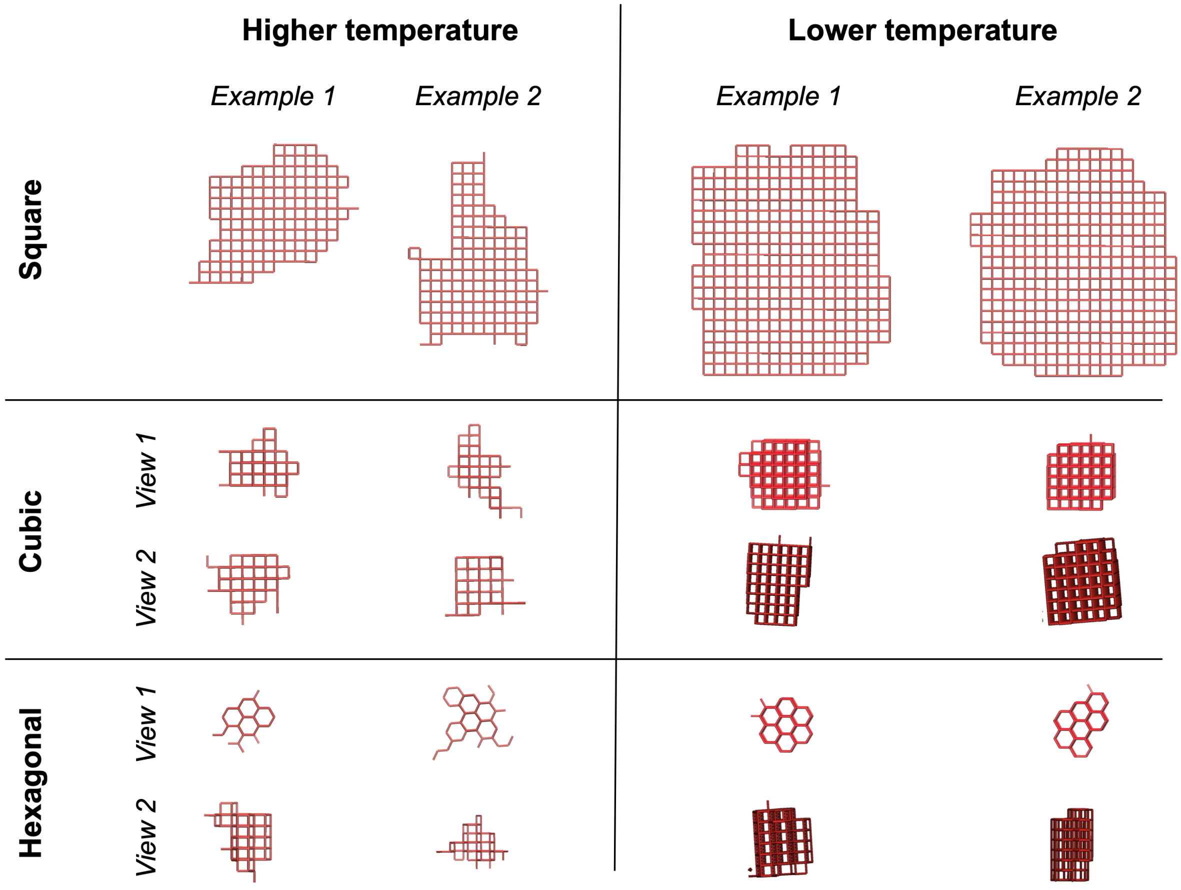

Figure 5.8: Snapshots of critical clusters on the square, cubic, and hexagonal lattices at 60% T_c (“higher temperature”) and 30% T_c (“lower temperature”). Lines connect nearest-neighbor sites in the cluster. Clusters show large shape fluctuations, with this phenomenon being more pronounced at higher temperature.

cluster-solution interface. At low temperatures, fluctuations should be relatively low, and individual instances of clusters should be representative of the average cluster shape. Meanwhile, at higher temperatures, fluctuations should be greater, and individual instances of clusters should differ from the average cluster shape. To quantify this trend, we derived an analytical expression for the surface tension of a cluster-solution interface, based on a simple model illustrated in Figure 5.10.

The corresponding analytical expression is derived for σ, the surface tension per unit length along the cluster-solution interface, as a function of temperature. Noting that the energy of a broken bond is $2J_\mathrm{h}$ horizontally and $2J_\mathrm{v}$ vertically, the energy E_i of the interface is

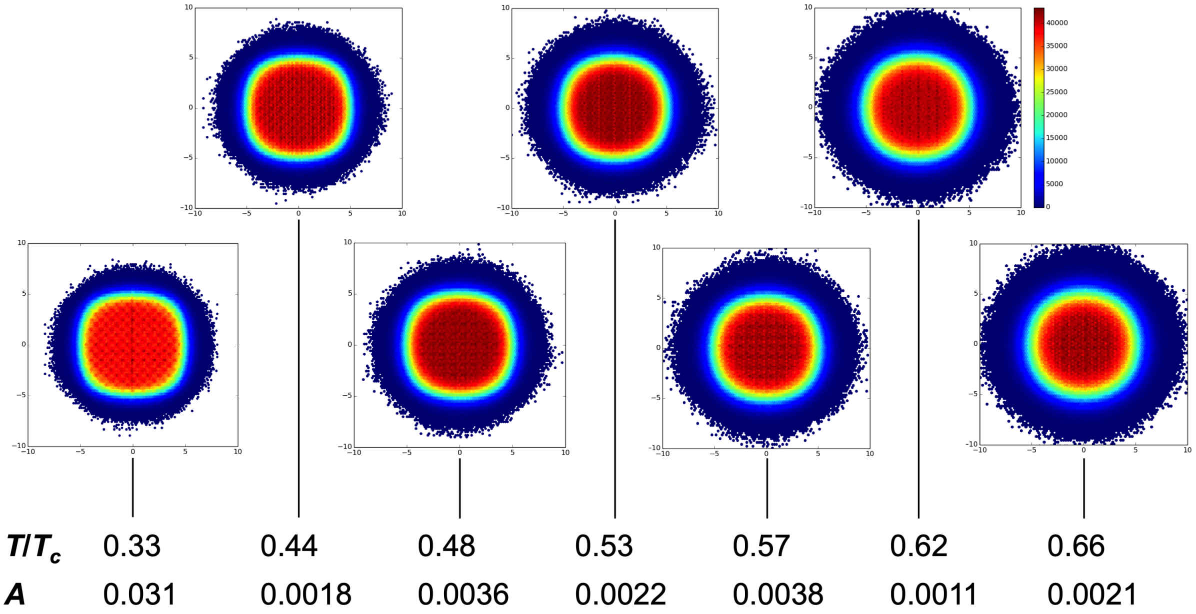

Figure 5.9: Density plots of clusters of size 85 on the square lattice at different temperatures, with $h = 0.071$. The color gradient is based on count, with about 106 clusters comprising each image. The axes quantify the cluster size. Clusters transition from square to circular as temperature increases. All values of A are close to 0, reflecting the fact that square and circular clusters are symmetric about the center of mass along each axis.

$$E_{\mathrm{i}}(\eta) = 2J_{\mathrm{v}}L + 2J_{\mathrm{h}}\sum_{n=1}^{L}|\eta_n|. \tag{5.10}$$

The canonical-ensemble partition function Z of the interface is

$$\begin{aligned}
Z &= \sum_{\{\eta\}} e^{-\beta E_{\mathrm{i}}(\eta)} \\
&= \sum_{\eta_1=-\infty}^{\infty}\sum_{\eta_2=-\infty}^{\infty}\cdots\sum_{\eta_L=-\infty}^{\infty} e^{-2\beta J_{\mathrm{v}}L-2\beta J_{\mathrm{h}}\sum_{n=1}^{L}|\eta_n|} \\
&= e^{-2\beta J_{\mathrm{v}}L}\left(\sum_{\eta=-\infty}^{\infty} e^{-2\beta J_{\mathrm{h}}|\eta|}\right)^{L},
\end{aligned} \tag{5.11}$$

An expression for σ, surface tension per unit length along the interface, is

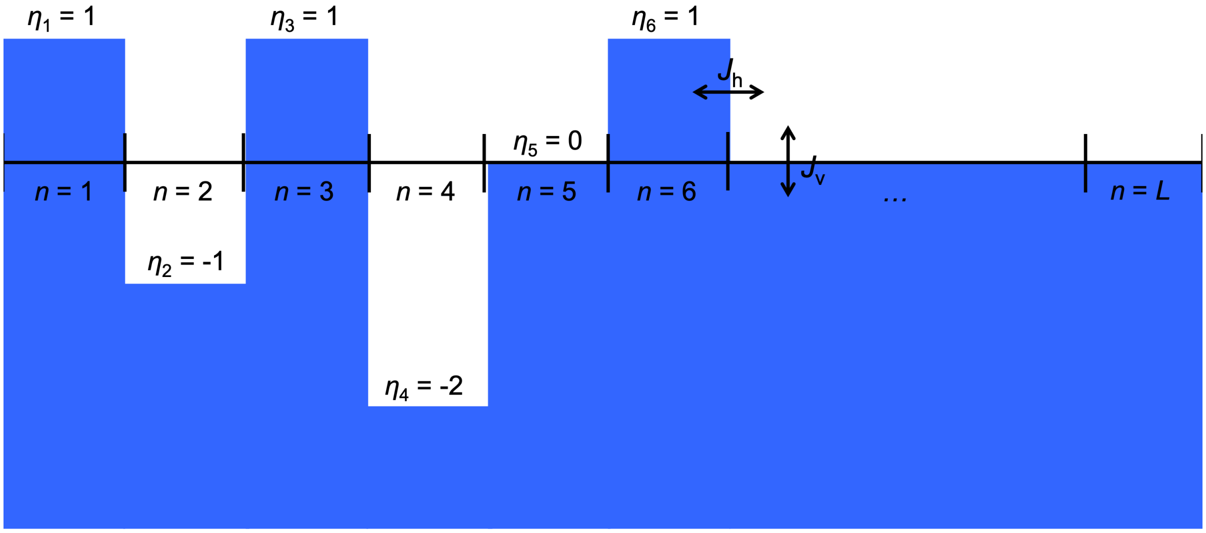

Figure 5.10: Simple model of an example interface of length L with periodic boundary conditions, where η_n = height of the surface above or below the interface, J_h = interaction energy between two sites neighboring horizontally, and J_v = interaction energy between two sites neighboring vertically.

$$\sigma = \frac{-k_\mathrm{B} T \ln Z}{L} = \frac{-\ln Z}{\beta L}. \tag{5.12}$$

Simplifying, and using an infinite sum formula, it can be shown that

$$\ln Z = -2\beta J_\mathrm{v} L + L \ln\left(\coth \beta J_\mathrm{h}\right), \tag{5.13}$$

so

$$\sigma = \frac{-\ln Z}{\beta L} = 2\beta J_\mathrm{v} - \ln\left(\coth \beta J_\mathrm{h}\right). \tag{5.14}$$

This is the Ising model surface tension in the direction of the lattice vectors known from the Onsager solution, and is plotted versus temperature in Figure 5.11a. Surface tension decreases with temperature until it vanishes at the critical temperature. It can be inferred from the form of the surface tension that root mean square fluctuations must increase with temperature, as these fluctuations are controlled by surface tension. This trend agrees with the cluster shape fluctuations observed in simulation (Figures 5.8 and 5.9).

In order to better understand the contribution of surface tension to the square-to-circular cluster shape transition, we take another simplified approach to consider the different surface tensions of 2-dimensional square and circular clusters of the same area.

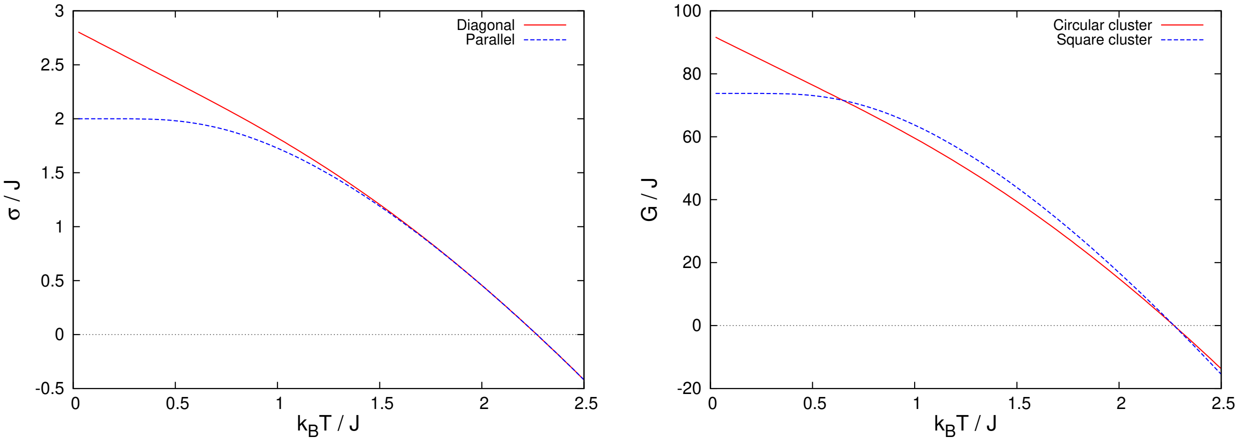

(a) (b)

Figure 5.11: a) Surface tension σ as a function of temperature in the direction parallel to the lattice vectors ($\sigma_{\|}$, Equations 5.14 and 5.15), and along the lattice diagonal (σ_{diag}, Equation 5.16). b) Surface tension contribution to the free energies G of a square and a circular cluster, each of size 85, which corresponds to the size of clusters in Figure 5.9. The surface tension is calculated as the product of the shape's perimeter ($4\sqrt{N}$ for a square and $2\sqrt{N\pi}$ for a circle) and its surface tension per unit length ($\sigma_{\|}$ for a square and σ_{diag} for a circle).

For a square cluster, the Ising model surface tension per unit length (with h=0 and $J = J_{\text{h}} = J_{\text{v}}$) is that in the direction of the lattice vectors, known from the Onsager solution [215, 220]:

$$\sigma_{\|} = 2J - k_{\text{B}}T \ln \coth \beta J. \tag{5.15}$$

For a circular cluster, an approximate surface tension per unit length is that of the diagonal on the Ising model lattice [221]:

$$\sigma_{\text{diag}} = \sqrt{2} k_{\text{B}}T \ln \sinh 2\beta J. \tag{5.16}$$

Considering that a square of area N has a perimeter of $4\sqrt{N}$, and a circle of the same area has a perimeter of $2\sqrt{N\pi}$, we compute the surface tension contribution to the free energy of clusters of these shapes as a function of temperature, with the results shown in Figure 5.11b.

There exists a temperature at which the square and circular clusters' free energies cross; thus the different surface tensions of square and circle give rise to a crossover temperature. This is because while the square has greater perimeter, its surface tension is much lower than the circle's at low temperatures but similar to the circle's at higher temperatures, so these competing effects result in a crossover temperature (Figure 5.11b). The crossover temperature is about 0.65 $k_{\text{B}}T/J$, or 0.29 T_{c}, which corresponds roughly to the transition temperature observed qualitatively in Figure 5.9.

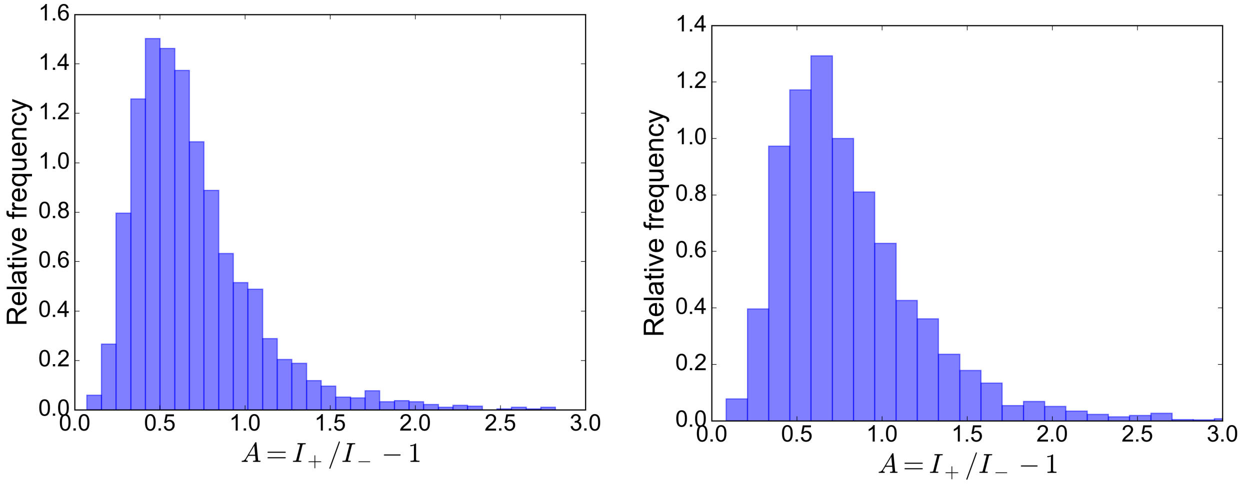

(a) Cubic lattice

(b) Hexagonal lattice

Figure 5.12: Histograms of A for clusters of critical size on the 3-dimensional a) cubic and b) hexagonal lattices at 60% of critical temperature. The average value of A is greater on the hexagonal lattice (0.824) than on the cubic lattice (0.698), indicating that clusters are elongated in one direction.

Thus the combination of surface tensions and surface fluctuations provides a basis for understanding the transition from square to circular clusters with increasing temperature.

Investigation of cluster elongation

Cluster shape was characterized quantitatively using the anisotropy parameter $A = I_+/I_- - 1$. This parameter was chosen since it detects elongation of clusters and since it is independent of the underlying coordinate system. However, this parameter does not distinguish between square and circular clusters, as both shapes have mass symmetrically distributed across the center of mass along each axis (see Figure 5.9).

We used this parameter to analyze the shape of critical clusters on the 3-dimensional cubic and hexagonal lattices. Distributions of A show that clusters on the hexagonal lattice are longer in one direction, which can be seen by the deviation of A from 0 (Figure 5.12). Figure 5.12a agrees with results from Pan et al. [214].

In order to obtain more information about fluctuations of cluster shape, we analyzed ratios of the principal moments of inertia. In Figure 5.13, deviation from (1, 1) indicates anisotropy. In particular, a cluster long in one direction has an I_- significantly smaller than both I_{mid} and I_+, meaning that I_+/I_- is especially large compared to I_+/I_{mid}. Figure 5.13 suggests that this is the case on the hexagonal lattice, at both temperatures considered. The relative difference between these two ratios is greater on the hexagonal lattice than on the cubic lattice. This is further confirmation that clusters on the hexagonal lattice are elongated

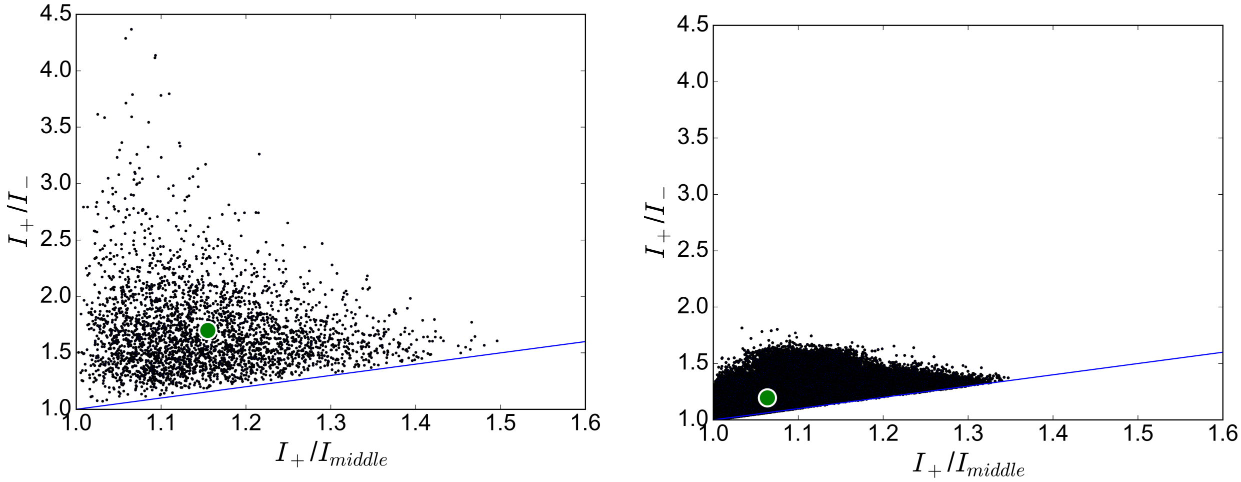

(a) Cubic lattice at 60% T_c. Averages: (1.15, 1.70)

(b) Cubic lattice at 30% T_c. Averages: (1.06, 1.20)

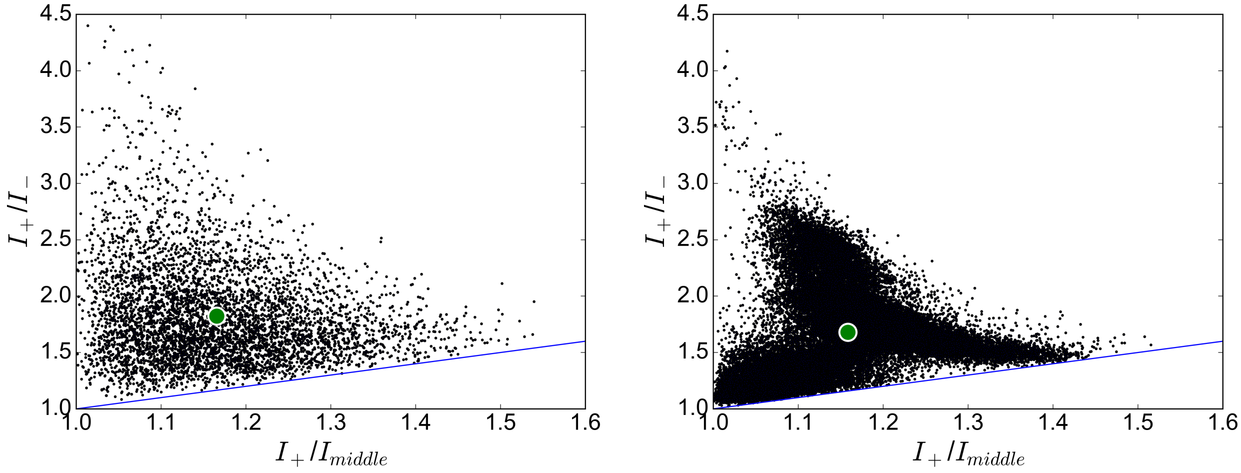

(c) Hexagonal lattice at 60% T_c. Averages: (1.17, 1.82)

(d) Hexagonal lattice at 30% T_c. Averages: (1.16, 1.68)

Figure 5.13: I_+/I_- vs. I_+/I_mid for critical clusters on the cubic and hexagonal lattices at 60% and 30% of critical temperature, with average values marked by a large circle and specified in the subcaptions. I_+ is the largest principal moment of inertia, I_- is the smallest, and I_mid is in the middle. Clusters on the hexagonal lattice are elongated in one direction, and fluctuations about the average are greater at higher temperature.

in one direction. Figure 5.13 also shows that fluctuations about the average are greater at higher temperature.

The principal axes of inertia reveal in which direction clusters are longer. The relevant eigenvector is $\mathbf{v}_-$, the eigenvector corresponding to the direction in which the cluster is the longest. Table 5.3 shows that on the hexagonal lattice, clusters are elongated in the c

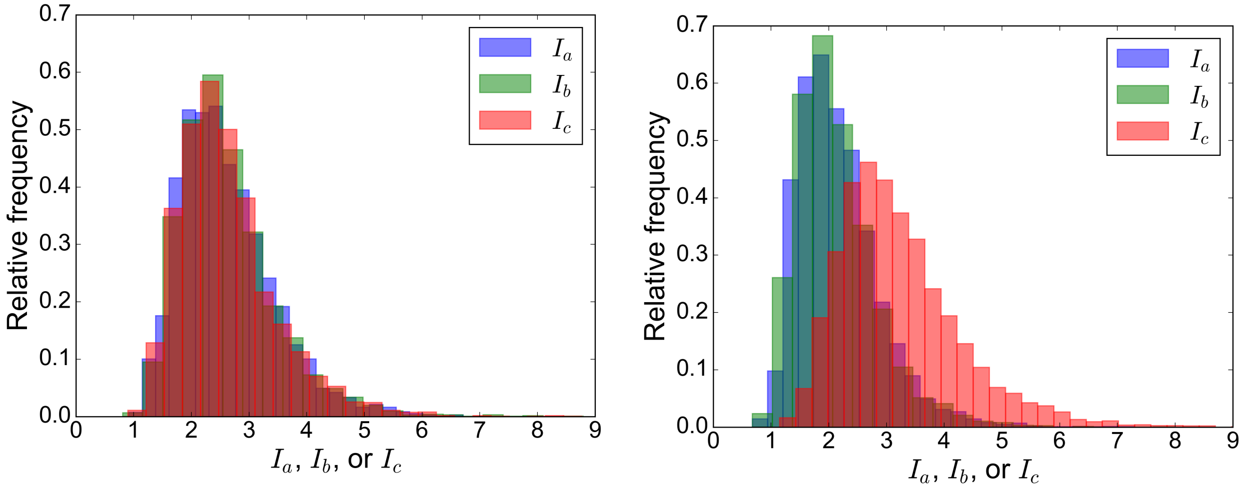

(a)

(b)

Figure 5.14: Histograms of I_a, I_b, and I_c for critical clusters on the a) cubic and b) hexagonal lattices at 60% of critical temperature. On the hexagonal lattice, critical clusters are elongated in the c direction.

direction, since the average c component of $\mathbf{v}_-$ is greater than the other two components.

	$T = 0.6T_\mathrm{c}$	$T = 0.3T_\mathrm{c}$
Cubic lattice	$\langle \mathbf{v}_- \rangle = (0.58, 0.57, 0.58)$	$\langle \mathbf{v}_- \rangle = (0.58, 0.58, 0.57)$
Hexagonal lattice	$\langle \mathbf{v}_- \rangle = (0.43, 0.43, 0.79)$	$\langle \mathbf{v}_- \rangle = (0.18, 0.18, 0.97)$

Table 5.3: Average $\mathbf{v}_-$, the eigenvectors corresponding to direction of elongation. Eigenvectors are normalized and each component is the absolute value. Clusters on hexagonal lattice are elongated in the c-direction.

Cluster shape was characterized quantitatively using a second measure, the quantities I_a, I_b, and I_c described in the Methods section. Histograms of these quantities clearly show that critical clusters on the hexagonal lattice are elongated in the c direction (Figure 5.14).

These measures have the downside of not being “coordinate-free”: they are defined based on the underlying lattice. However, this allows a comparison to classical nucleation theory (CNT). In particular, we compared simulation results for critical cluster aspect ratio and free-energy barrier height to predictions from CNT. To obtain the CNT predictions, a cluster on the hexagonal lattice is represented as a cylinder with length in the c direction (Figure 5.15).

The CNT prediction for cluster ratio can be determined by expressing the cluster free energy as follows:

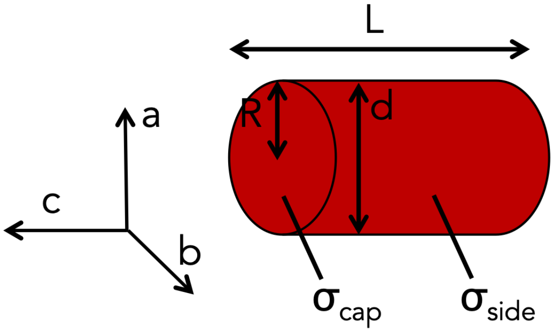

Figure 5.15: Representation of a cluster on the hexagonal lattice for use in classical nucleation theory (CNT) estimates. The surface tension energy of the different surfaces of the cluster is estimated by assuming flat surfaces and determining the density of broken bonds on interface planes in the hexagonal lattice.

$$\Delta G(R, L) = -\Delta g \pi R^2 L + \sigma_{\text{side}} 2\pi R L + 2\sigma_{\text{cap}} \pi R^2 \tag{5.17}$$

This free energy is maximized with respect to R and L in order to find the aspect ratio L^*/d^* of a critical cluster:

$$\begin{aligned} \frac{\delta \Delta G}{\delta R} &= 0 = \frac{\delta \Delta G}{\delta L} \\ \frac{L^*}{R^*} &= \frac{2\sigma_{\text{cap}}}{\sigma_{\text{side}}} \\ \frac{L^*}{d^*} = \frac{\sigma_{\text{cap}}}{\sigma_{\text{side}}} &= \frac{1.54J}{1.33J} \approx 1.2 \end{aligned} \tag{5.18}$$

As seen above, the CNT expression for aspect ratio depends on the surface areas of the different surfaces of the cluster. The aspect ratio is also obtained from simulation:

$$\frac{L^*}{d^*} = \sqrt{\left\langle \frac{I_c}{I_a} \right\rangle} \approx 1.3 \tag{5.19}$$

The simulation result and CNT prediction for aspect ratio agree closely. The CNT-derived expression for aspect ratio depends on the surface tensions of the two surfaces. Thus there is a thermodynamic reason for elongation of clusters in the c direction: different surface tension energies of the surfaces.

We performed a similar analysis to compare simulation results for free-energy barrier height to CNT predictions, representing a cluster on the cubic lattice as a sphere. The following CNT prediction for barrier height ratio is obtained:

$$\frac{\Delta G^{\text{max}}_{\text{cylinder}}}{\Delta G^{\text{max}}_{\text{sphere}}} = \frac{3\sigma^2_{\text{side}}\sigma_{\text{cap}}\Delta g^2_{\text{sphere}}}{2\sigma^3_{\text{sphere}}\Delta g^2_{\text{cylinder}}} = 0.88 \tag{5.20}$$

The corresponding simulation result is:

$$\frac{\Delta G^{\text{max}}_{\text{hexagonal}}}{\Delta G^{\text{max}}_{\text{cubic}}} = 0.91 \tag{5.21}$$

The close agreement between simulation and theory indicates that the simulation results are logical and provides further vindication of the validity of using CNT to argue that different surface tension energies of the different cluster surfaces constitutes a thermodynamic reason for elongation of clusters in the c direction.

5.4 Conclusion

In conclusion, we have investigated the assembly process of MOF-74, representing the MOF with a simple lattice model and modeling nucleation using the Ising model and Monte Carlo simulations. The thermodynamic assembly pathway has been mapped out by generating free-energy barriers to nucleation, and fluctuations in cluster shape have been investigated. Nucleating clusters are elongated along the crystallographic c axis, the direction of elongation of experimentally observed crystals, due to different surface tension energies of the cluster surfaces.

These insights contribute to an understanding of the assembly process of MOFs, a better understanding of which is necessary to synthesize MOFs with crystals of the desired morphology and to grow defect-free films of MOFs on surfaces.

An instructive extension of this project is to examine the use of different reaction coordinates other than cluster size, such as surface area, to help determine what other factors are important in the assembly process of MOF-74. A next step would be to compare structures formed from near-equilibrium vs. growth-dominated assembly pathways, which is relevant not only to MOF formation, but also in a more general context for nucleating systems.

Another interesting way in which to extend this project is to make the model more physically realistic. Instead of a one-component model, a two-component model could be developed, with different linker and metal components. Alternatively, complexity could be introduced by developing a model with multiple possible states per site, with different states reflecting how many bonds are formed from each site. Such a model could give a more detailed and more realistic depiction of the assembly process. Additionally, parameters representing interaction energies between components, and with solvent, could be incorporated from molecular simulation and/or experiment. Interaction energies in different planes would likely be different. This model could be used to examine the effect of changing the framework metal and the solvent, thereby facilitating comparison with experimental results and potentially providing useful information for favorable synthesis conditions. Finally, the model could be modified to describe other MOFs in order to obtain a broader picture of MOF assembly.

Chapter 6

Conclusions and outlook

In conclusion, we have carried out computational studies using three different approaches towards advancing nanoporous materials for clean energy applications.

In Chapters 2 and 3, we screen databases of tens of thousands and hundreds of thousands of nanoporous materials for carbon capture and hydrogen storage, respectively. Top candidates, both hypothetical and already-synthesized, are identified for these applications, and the top-performing materials' common characteristics are analyzed. It is demonstrated that it is appropriate to use CO_2 Henry coefficient as a pre-screening variable for carbon capture; this can be utilized in future studies. We have also shown that covalent-organic frameworks (COFs), which have been understudied for carbon capture, have potential as efficient materials for this application, and we recommend further investigation of these materials, including functionalized COFs (e.g. [222, 223]). More generally, future screening studies of nanoporous materials will utilize the emerging and rapidly-advancing technique of machine learning, with input from molecular simulation [224–226]. As this and related techniques are developed, there should be great potential for screening ever greater numbers of materials while gaining deeper insights. One goal of computational screening studies is to identify top-performing materials, which can then be synthesized, (hopefully) demonstrated to perform well in real life, and be implemented in real applications. However, better techniques are needed to predict how synthesizable a material is. This is an important field of future study.

In Chapter 4, we study in depth a novel biporous metal-organic framework (MOF) for CO_2/CH_4 separation, which is relevant in natural gas processing. We elucidate the molecular interactions responsible for this MOF's separation performance under different activation states. This work demonstrates a way to harness the biporosity of a MOF in order to tune its CO_2/CH_4 separation performance. This helps to motivate the development of new biporous MOFs, not just for natural gas processing, but for any gas separation. More generally, this work contributes fundamental understanding of molecular-level interactions that are responsible for a MOF's macroscopic separation performance.

In Chapter 5, we investigate the assembly process of MOF-74, using a statistical mechanical lattice model to isolate the effects of framework geometry and surface tensions on the nucleation of MOF crystals. It is demonstrated that different surface tension energies of different cluster surfaces leads to nucleating clusters that are elongated in the same direction as the macroscopic crystals. These findings help to shed light on the thermodynamic assembly pathway of MOF-74 and contribute understanding of how different factors affect the final crystal shape. The assembly process is not established for most MOFs, and if this process can be better understood, there is enormous potential impact: the ability to rationally design a material and determine a priori what reaction conditions are needed to synthesize a crystal of given morphology would greatly advance the development of nanoporous materials for any application. Greater understanding of nucleation and nonequilibrium events, not just in MOFs but in any of the plethora of systems where nucleation and crystallization occur, will help work towards a greater understanding of the MOF assembly process [227]. Studies involving collaboration among experiment, molecular simulation, and ab initio methods will be especially helpful in gaining insight into the assembly process.

References

1. Zhou, H.-C., Long, J. R. & Yaghi, O. M. Introduction to Metal–Organic Frameworks. *Chemical Reviews* **112,** 673–674. ISSN: 0009-2665 (Feb. 2012).
2. Waller, P. J., Gándara, F. & Yaghi, O. M. Chemistry of Covalent Organic Frameworks. *Accounts of Chemical Research* **48,** 3053–3063. ISSN: 0001-4842 (Dec. 2015).
3. Morris, R. E. & Wheatley, P. S. Gas Storage in Nanoporous Materials. *Angewandte Chemie International Edition* **47,** 4966–4981. ISSN: 14337851 (June 2008).
4. Gottardi, G. & Galli, E. *Natural Zeolites* (Springer-Verlag, Berlin, 1985).
5. U.S. Geological Survey. *Mineral Commodity Summaries, Zeolites (Natural)* 2018.
6. Weitkamp, J. Zeolites and catalysis. *Solid State Ionics* **131,** 175–188. ISSN: 01672738 (June 2000).
7. *Functional Metal-Organic Frameworks: Gas Storage, Separation and Catalysis* (ed Schröder, M.) (Springer-Verlag, Berlin, 2010).
8. Smit, B. & Maesen, T. L. M. Molecular Simulations of Zeolites: Adsorption, Diffusion, and Shape Selectivity. *Chemical Reviews* **108,** 4125–4184. ISSN: 0009-2665 (Oct. 2008).
9. Yang, H. *et al.* Progress in carbon dioxide separation and capture: A review. *Journal of Environmental Sciences* **20,** 14–27. ISSN: 10010742 (Jan. 2008).
10. Kosinov, N., Gascon, J., Kapteijn, F. & Hensen, E. J. Recent developments in zeolite membranes for gas separation. *Journal of Membrane Science* **499,** 65–79. ISSN: 03767388 (Feb. 2016).
11. Farha, O. K. *et al.* Metal–Organic Framework Materials with Ultrahigh Surface Areas: Is the Sky the Limit? *Journal of the American Chemical Society* **134,** 15016–15021. ISSN: 0002-7863 (Sept. 2012).
12. Zhou, H.-C. & Kitagawa, S. Metal–Organic Frameworks (MOFs). *Chem. Soc. Rev.* **43,** 5415–5418. ISSN: 0306-0012 (July 2014).
13. Furukawa, H., Cordova, K. E., O'Keeffe, M. & Yaghi, O. M. The Chemistry and Applications of Metal-Organic Frameworks. *Science* **341,** 1230444–1230444. ISSN: 0036-8075 (Aug. 2013).

14. Li, H., Eddaoudi, M., O'Keeffe, M. & Yaghi, O. M. Design and synthesis of an exceptionally stable and highly porous metal-organic framework. *Nature* **402,** 276–279. ISSN: 0028-0836 (Nov. 1999).
15. Mason, J. A., Veenstra, M. & Long, J. R. Evaluating metal–organic frameworks for natural gas storage. *Chem. Sci.* **5,** 32–51. ISSN: 2041-6520 (2014).
16. Langmi, H. W., Ren, J., North, B., Mathe, M. & Bessarabov, D. Hydrogen Storage in Metal-Organic Frameworks: A Review. *Electrochimica Acta* **128,** 368–392. ISSN: 00134686 (May 2014).
17. Sumida, K. *et al.* Carbon Dioxide Capture in Metal–Organic Frameworks. *Chemical Reviews* **112,** 724–781. ISSN: 0009-2665 (Feb. 2012).
18. Li, J.-R., Kuppler, R. J. & Zhou, H.-C. Selective gas adsorption and separation in metal–organic frameworks. *Chemical Society Reviews* **38,** 1477. ISSN: 0306-0012 (2009).
19. Denny, M. S., Moreton, J. C., Benz, L. & Cohen, S. M. Metal–organic frameworks for membrane-based separations. *Nature Reviews Materials* **1,** 16078. ISSN: 2058-8437 (Dec. 2016).
20. Jacoby, M. *Materials Chemistry: Metal-Organic Frameworks Go Commercial* 2013. <`https://cen.acs.org/articles/91/i51/Materials-Chemistry-Metal-Organic-Frameworks.html`>.
21. Frameworks for commercial success. *Nature Chemistry* **8,** 987–987. ISSN: 1755-4330 (Oct. 2016).
22. Chen, B., Yang, Z., Zhu, Y. & Xia, Y. Zeolitic imidazolate framework materials: recent progress in synthesis and applications. *J. Mater. Chem. A* **2,** 16811–16831. ISSN: 2050-7488 (2014).
23. Feng, X., Ding, X. & Jiang, D. Covalent organic frameworks. *Chemical Society Reviews* **41,** 6010. ISSN: 0306-0012 (2012).
24. Ding, S.-Y. & Wang, W. Covalent organic frameworks (COFs): from design to applications. *Chem. Soc. Rev.* **42,** 548–568. ISSN: 0306-0012 (2013).
25. Mercado, R. *et al.* In Silico Design of 2D and 3D Covalent Organic Frameworks for Methane Storage Applications. *Chemistry of Materials* **30,** 5069–5086. ISSN: 0897-4756 (Aug. 2018).
26. Furukawa, H. & Yaghi, O. M. Storage of Hydrogen, Methane, and Carbon Dioxide in Highly Porous Covalent Organic Frameworks for Clean Energy Applications. *Journal of the American Chemical Society* **131,** 8875–8883. ISSN: 0002-7863 (July 2009).
27. Zeng, Y., Zou, R. & Zhao, Y. Covalent Organic Frameworks for CO_2 Capture. *Advanced Materials* **28,** 2855–2873. ISSN: 09359648 (Apr. 2016).
28. Cote, A. P. Porous, Crystalline, Covalent Organic Frameworks. *Science* **310,** 1166–1170. ISSN: 0036-8075 (Nov. 2005).

29. Smit, B., Reimer, J. A., Oldenburg, C. M. & Bourg, I. C. *Introduction to Carbon Capture and Sequestration* ISBN: 978-1-78326-327-1. doi:`10.1142/p911`. <`http://www.worldscientific.com/worldscibooks/10.1142/p911`> (Imperial College Press, London, 2014).

30. Bui, M. *et al.* Carbon capture and storage (CCS): the way forward. *Energy & Environmental Science* **11,** 1062–1176. ISSN: 1754-5692 (2018).

31. Intergovernmental Panel on Climate Change. *Global warming of 1.5°C. An IPCC Special Report on the impacts of global warming of 1.5°C above pre-industrial levels and related global greenhouse gas emission pathways, in the context of strengthening the global response to the threat of climate change,* tech. rep. (2018).

32. International Energy Agency. 20 Years of Carbon Capture and Storage: Accelerating Future Deployment (2016).

33. Global CCS Institute. The Global Status of CCS (2018).

34. Jackson, R. B. *et al.* Global energy growth is outpacing decarbonization. *Environmental Research Letters* **13,** 120401. ISSN: 1748-9326 (Dec. 2018).

35. Vitillo, J. G., Smit, B. & Gagliardi, L. Introduction: Carbon Capture and Separation. *Chemical Reviews* **117,** 9521–9523. ISSN: 0009-2665 (July 2017).

36. Haszeldine, R. S. Carbon Capture and Storage: How Green Can Black Be? *Science* **325,** 1647–1652. ISSN: 0036-8075 (Sept. 2009).

37. Rochelle, G. T. Amine Scrubbing for CO_2 Capture. *Science* **325,** 1652–1654. ISSN: 0036-8075 (Sept. 2009).

38. Heldebrant, D. J. *et al.* Water-Lean Solvents for Post-Combustion CO_2 Capture: Fundamentals, Uncertainties, Opportunities, and Outlook. *Chemical Reviews* **117,** 9594–9624. ISSN: 0009-2665 (July 2017).

39. Blamey, J., Anthony, E., Wang, J. & Fennell, P. The calcium looping cycle for large-scale CO_2 capture. *Progress in Energy and Combustion Science* **36,** 260–279. ISSN: 03601285 (Apr. 2010).

40. Khalilpour, R. *et al.* Membrane-based carbon capture from flue gas: a review. *Journal of Cleaner Production* **103,** 286–300. ISSN: 09596526 (Sept. 2015).

41. Ben-Mansour, R. *et al.* Carbon capture by physical adsorption: Materials, experimental investigations and numerical modeling and simulations - A review. *Applied Energy* **161,** 225–255. ISSN: 03062619 (Jan. 2016).

42. Lee, S.-Y. & Park, S.-J. A review on solid adsorbents for carbon dioxide capture. *Journal of Industrial and Engineering Chemistry* **23,** 1–11. ISSN: 1226086X (Mar. 2015).

43. Figueroa, J. D., Fout, T., Plasynski, S., McIlvried, H. & Srivastava, R. D. Advances in CO_2 capture technology—The U.S. Department of Energy's Carbon Sequestration Program. *International Journal of Greenhouse Gas Control* **2,** 9–20. ISSN: 17505836 (Jan. 2008).
44. Alonso, A. *et al.* Critical review of existing nanomaterial adsorbents to capture carbon dioxide and methane. *Science of The Total Environment* **595,** 51–62. ISSN: 00489697 (Oct. 2017).
45. Yu, J. *et al.* CO_2 Capture and Separations Using MOFs: Computational and Experimental Studies. *Chemical Reviews* **117,** 9674–9754. ISSN: 0009-2665 (July 2017).
46. International Energy Agency. *World Energy Outlook 2017* tech. rep. (2017).
47. Cano, Z. P. *et al.* Batteries and fuel cells for emerging electric vehicle markets. *Nature Energy* **3,** 279–289. ISSN: 2058-7546 (Apr. 2018).
48. International Energy Agency. Technology Roadmap: Hydrogen and Fuel Cells (2015).
49. U.S. Department of Energy - Energy Efficiency and Renewable Energy. *Hydrogen Basics* <`https://afdc.energy.gov/fuels/hydrogen%7B%5C_%7Dbasics.html`> (visited on 03/12/2019).
50. U.S. Department of Energy - Energy Efficiency and Renewable Energy. *Hydrogen Storage* tech. rep. (2017).
51. Wilberforce, T. *et al.* Developments of electric cars and fuel cell hydrogen electric cars. *International Journal of Hydrogen Energy* **42,** 25695–25734. ISSN: 03603199 (Oct. 2017).
52. Office of Energy Efficiency & Renewable Energy. *Hydrogen Storage Challenges* <`https://www.energy.gov/eere/fuelcells/hydrogen-storage-challenges`> (visited on 06/27/2019).
53. Abdalla, A. M. *et al.* Hydrogen production, storage, transportation and key challenges with applications: A review. *Energy Conversion and Management* **165,** 602–627. ISSN: 01968904 (June 2018).
54. Yu, X., Tang, Z., Sun, D., Ouyang, L. & Zhu, M. Recent advances and remaining challenges of nanostructured materials for hydrogen storage applications. *Progress in Materials Science* **88,** 1–48. ISSN: 00796425 (July 2017).
55. International Energy Agency. *Natural gas* <`https://www.iea.org/topics/naturalgas/`> (visited on 03/13/2019).
56. International Energy Agency. *Natural Gas Statistics* <`https://www.iea.org/statistics/naturalgas/`> (visited on 03/13/2019).
57. International Energy Agency. *Gas 2018: Analysis and Forecasts to 2023* tech. rep. (2018).

58. Mokhatab, S., Poe, W. A. & Mak, J. Y. *Handbook of Natural Gas Transmission and Processing: Principles and Practices* Fourth (Elsevier, 2019).
59. Baker, R. W. & Lokhandwala, K. Natural Gas Processing with Membranes: An Overview. *Industrial & Engineering Chemistry Research* **47,** 2109–2121. ISSN: 0888-5885 (Apr. 2008).
60. Faramawy, S., Zaki, T. & Sakr, A.-E. Natural gas origin, composition, and processing: A review. *Journal of Natural Gas Science and Engineering* **34,** 34–54. ISSN: 18755100 (Aug. 2016).
61. Ullah Khan, I. *et al.* Biogas as a renewable energy fuel – A review of biogas upgrading, utilisation and storage. *Energy Conversion and Management* **150,** 277–294. ISSN: 01968904 (Oct. 2017).
62. Alcheikhhamdon, Y. & Hoorfar, M. Natural gas purification from acid gases using membranes: A review of the history, features, techno-commercial challenges, and process intensification of commercial membranes. *Chemical Engineering and Processing - Process Intensification* **120,** 105–113. ISSN: 02552701 (Oct. 2017).
63. Shimekit, B. & Mukhtar, H. in *Advances in Natural Gas Technology* 235–270 (InTech, Apr. 2012). doi:`10.5772/38656`. <`http://www.intechopen.com/books/advances-in-natural-gas-technology/natural-gas-purification-technologies-major-advances-for-co2-separation-and-future-directions`>.
64. Chaemchuen, S., Kabir, N. A., Zhou, K. & Verpoort, F. Metal–organic frameworks for upgrading biogas via CO_2 adsorption to biogas green energy. *Chemical Society Reviews* **42,** 9304. ISSN: 0306-0012 (2013).
65. Braun, E. *et al.* High-throughput computational screening of nanoporous adsorbents for CO_2 capture from natural gas. *Molecular Systems Design & Engineering* **1,** 175–188. ISSN: 2058-9689 (2016).
66. Britt, D., Furukawa, H., Wang, B., Glover, T. G. & Yaghi, O. M. Highly efficient separation of carbon dioxide by a metal-organic framework replete with open metal sites. *Proceedings of the National Academy of Sciences* **106,** 20637–20640. ISSN: 0027-8424 (Dec. 2009).
67. Sarkisov, L., Martin, R. L., Haranczyk, M. & Smit, B. On the Flexibility of Metal-Organic Frameworks. *Journal of the American Chemical Society* **136,** 2228–2231. ISSN: 0002-7863 (Feb. 2014).
68. Witman, M. *et al.* The Influence of Intrinsic Framework Flexibility on Adsorption in Nanoporous Materials. *Journal of the American Chemical Society* **139,** 5547–5557. ISSN: 0002-7863 (Apr. 2017).
69. Frenkel, D. & Smit, B. *Understanding Molecular Simulation: From Algorithms to Applications* Second (Elsevier, 2002).

70. Wells, B. A. & Chaffee, A. L. Ewald Summation for Molecular Simulations. *Journal of Chemical Theory and Computation* **11,** 3684–3695. ISSN: 1549-9618 (Aug. 2015).
71. Chen, Z.-M., Çağin, T. & Goddard, W. A. Fast Ewald sums for general van der Waals potentials. *Journal of Computational Chemistry* **18,** 1365–1370. ISSN: 0192-8651 (Aug. 1997).
72. Buch, V. Path integral simulations of mixed para-D_2 and ortho-D_2 clusters: The orientational effects. *The Journal of Chemical Physics* **100,** 7610–7629. ISSN: 0021-9606 (May 1994).
73. Harris, J. G. & Yung, K. H. Carbon Dioxide's Liquid-Vapor Coexistence Curve And Critical Properties as Predicted by a Simple Molecular Model. *The Journal of Physical Chemistry* **99,** 12021–12024. ISSN: 0022-3654 (Aug. 1995).
74. García-Sánchez, A. *et al.* Transferable Force Field for Carbon Dioxide Adsorption in Zeolites. *The Journal of Physical Chemistry C* **113,** 8814–8820. ISSN: 1932-7447 (May 2009).
75. Deeg, K. S. *et al.* Insights on the Molecular Mechanisms of Hydrogen Adsorption in Zeolites. *The Journal of Physical Chemistry C* **117,** 14374–14380. ISSN: 1932-7447 (July 2013).
76. Dzubak, A. L. *et al.* Ab initio carbon capture in open-site metal–organic frameworks. *Nature Chemistry* **4,** 810–816. ISSN: 1755-4330 (Oct. 2012).
77. Mercado, R. *et al.* Force Field Development from Periodic Density Functional Theory Calculations for Gas Separation Applications Using Metal–Organic Frameworks. *The Journal of Physical Chemistry C* **120,** 12590–12604. ISSN: 1932-7447 (June 2016).
78. Rappe, A. K., Casewit, C. J., Colwell, K. S., Goddard, W. A. & Skiff, W. M. UFF, a full periodic table force field for molecular mechanics and molecular dynamics simulations. *Journal of the American Chemical Society* **114,** 10024–10035. ISSN: 0002-7863 (Dec. 1992).
79. Mayo, S. L., Olafson, B. D. & Goddard, W. A. DREIDING: a generic force field for molecular simulations. *The Journal of Physical Chemistry* **94,** 8897–8909. ISSN: 0022-3654 (Dec. 1990).
80. Martin, M. G. & Siepmann, J. I. Transferable Potentials for Phase Equilibria. 1. United-Atom Description of n-Alkanes. *J. Phys. Chem. B* **102,** 2569–2577 (1998).
81. Mulliken, R. S. Electronic Population Analysis on LCAO–MO Molecular Wave Functions. I. *The Journal of Chemical Physics* **23,** 1833–1840. ISSN: 0021-9606 (Oct. 1955).
82. Campañá, C., Mussard, B. & Woo, T. K. Electrostatic Potential Derived Atomic Charges for Periodic Systems Using a Modified Error Functional. *Journal of Chemical Theory and Computation* **5,** 2866–2878. ISSN: 1549-9618 (Oct. 2009).

83. Manz, T. A. & Sholl, D. S. Chemically Meaningful Atomic Charges That Reproduce the Electrostatic Potential in Periodic and Nonperiodic Materials. *Journal of Chemical Theory and Computation* **6,** 2455–2468. ISSN: 1549-9618 (Aug. 2010).

84. Ongari, D. *et al.* Evaluating Charge Equilibration Methods To Generate Electrostatic Fields in Nanoporous Materials. *Journal of Chemical Theory and Computation* **15,** 382–401. ISSN: 1549-9618 (Jan. 2019).

85. Chandler, D. *Introduction to Modern Statistical Mechanics* (Oxford University Press, Inc., New York, 1987).

86. Lin, Y., Kong, C., Zhang, Q. & Chen, L. Metal-Organic Frameworks for Carbon Dioxide Capture and Methane Storage. *Advanced Energy Materials* **7,** 1601296. ISSN: 16146832 (Feb. 2017).

87. Choi, S., Drese, J. H. & Jones, C. W. Adsorbent Materials for Carbon Dioxide Capture from Large Anthropogenic Point Sources. *ChemSusChem* **2,** 796–854. ISSN: 18645631 (Sept. 2009).

88. D'Alessandro, D. M., Smit, B. & Long, J. R. Carbon Dioxide Capture: Prospects for New Materials. *Angewandte Chemie International Edition* **49,** 6058–6082. ISSN: 14337851 (Aug. 2010).

89. Trickett, C. A. *et al.* The chemistry of metal–organic frameworks for CO_2 capture, regeneration and conversion. *Nature Reviews Materials* **2,** 17045. ISSN: 2058-8437 (Aug. 2017).

90. Mason, J. A., Sumida, K., Herm, Z. R., Krishna, R. & Long, J. R. Evaluating metal–organic frameworks for post-combustion carbon dioxide capture via temperature swing adsorption. *Energy & Environmental Science* **4,** 3030. ISSN: 1754-5692 (2011).

91. Ben, T. *et al.* Targeted Synthesis of a Porous Aromatic Framework with High Stability and Exceptionally High Surface Area. *Angewandte Chemie International Edition* **48,** 9457–9460. ISSN: 14337851 (Dec. 2009).

92. Babarao, R. & Jiang, J. Molecular Screening of Metal-Organic Frameworks for CO_2 Storage. *Langmuir* **24,** 6270–6278. ISSN: 0743-7463 (June 2008).

93. Babarao, R. & Jiang, J. Exceptionally high CO_2 storage in covalent-organic frameworks: Atomistic simulation study. *Energy & Environmental Science* **1,** 139. ISSN: 1754-5692 (2008).

94. Choi, Y. J., Choi, J. H., Choi, K. M. & Kang, J. K. Covalent organic frameworks for extremely high reversible CO_2 uptake capacity: a theoretical approach. *J. Mater. Chem.* **21,** 1073–1078. ISSN: 0959-9428 (2011).

95. Tong, M., Yang, Q., Xiao, Y. & Zhong, C. Revealing the structure–property relationship of covalent organic frameworks for CO_2 capture from postcombustion gas: a multi-scale computational study. *Phys. Chem. Chem. Phys.* **16,** 15189–15198. ISSN: 1463-9076 (2014).

96. Zhao, Y., Yao, K. X., Teng, B., Zhang, T. & Han, Y. A perfluorinated covalent triazine-based framework for highly selective and water-tolerant CO_2 capture. *Energy & Environmental Science* **6,** 3684. ISSN: 1754-5692 (2013).

97. Lin, L.-C. *et al.* In silico screening of carbon-capture materials. *Nature Materials* **11,** 633–641. ISSN: 1476-1122 (July 2012).

98. Huck, J. M. *et al.* Evaluating different classes of porous materials for carbon capture. *Energy Environ. Sci.* **7,** 4132–4146. ISSN: 1754-5692 (2014).

99. Martin, R. L., Smit, B. & Haranczyk, M. Addressing Challenges of Identifying Geometrically Diverse Sets of Crystalline Porous Materials. *Journal of Chemical Information and Modeling* **52,** 308–318. ISSN: 1549-9596 (Feb. 2012).

100. Willems, T. F., Rycroft, C. H., Kazi, M., Meza, J. C. & Haranczyk, M. Algorithms and tools for high-throughput geometry-based analysis of crystalline porous materials. *Microporous and Mesoporous Materials* **149,** 134–141. ISSN: 13871811 (Feb. 2012).

101. Ongari, D. *et al.* Accurate Characterization of the Pore Volume in Microporous Crystalline Materials. *Langmuir* **33,** 14529–14538. ISSN: 0743-7463 (Dec. 2017).

102. Potoff, J. J. & Siepmann, J. I. Vapor-liquid equilibria of mixtures containing alkanes, carbon dioxide, and nitrogen. *AIChE Journal* **47,** 1676–1682. ISSN: 00011541 (July 2001).

103. *Personal communication with Daniele Ongari, March 2019*

104. Dubbeldam, D., Calero, S., Ellis, D. E. & Snurr, R. Q. RASPA: molecular simulation software for adsorption and diffusion in flexible nanoporous materials. *Molecular Simulation* **42,** 81–101. ISSN: 0892-7022 (Jan. 2016).

105. Vlugt, T. J. H., García-Pérez, E., Dubbeldam, D., Ban, S. & Calero, S. Computing the Heat of Adsorption using Molecular Simulations: The Effect of Strong Coulombic Interactions. *Journal of Chemical Theory and Computation* **4,** 1107–1118. ISSN: 1549-9618 (July 2008).

106. Myers, A. L. & Prausnitz, J. M. Thermodynamics of mixed-gas adsorption. *AIChE Journal* **11,** 121–127. ISSN: 0001-1541 (Jan. 1965).

107. Simon, C. M., Smit, B. & Haranczyk, M. pyIAST: Ideal adsorbed solution theory (IAST) Python package. *Computer Physics Communications* **200,** 364–380. ISSN: 00104655 (Mar. 2016).

108. Pizzi, G., Cepellotti, A., Sabatini, R., Marzari, N. & Kozinsky, B. AiiDA: automated interactive infrastructure and database for computational science. *Computational Materials Science* **111,** 218–230. ISSN: 09270256 (Jan. 2016).

109. The World Bank. *CO_2 emissions from transport (% of total fuel combustion)* (visited on 03/13/2019).

110. Broom, D. P. *et al.* Outlook and challenges for hydrogen storage in nanoporous materials. *Applied Physics A* **122,** 151. ISSN: 0947-8396 (Mar. 2016).

111. Furukawa, H. *et al.* Ultrahigh Porosity in Metal-Organic Frameworks. *Science* **329,** 424–428. ISSN: 0036-8075 (July 2010).

112. Farha, O. K. *et al.* De novo synthesis of a metal–organic framework material featuring ultrahigh surface area and gas storage capacities. *Nature Chemistry* **2,** 944–948. ISSN: 1755-4330 (Nov. 2010).

113. U.S. Department of Energy - Energy Efficiency and Renewable Energy. *DOE Technical Targets for Onboard Hydrogen Storage for Light-Duty Vehicles* <`https://www.energy.gov/eere/fuelcells/doe-technical-targets-onboard-hydrogen-storage-light-duty-vehicles`> (visited on 03/13/2019).

114. Wilmer, C. E. *et al.* Large-scale screening of hypothetical metal–organic frameworks. *Nature Chemistry* **4,** 83–89. ISSN: 1755-4330 (Feb. 2012).

115. Chung, Y. G. *et al.* Computation-Ready, Experimental Metal–Organic Frameworks: A Tool To Enable High-Throughput Screening of Nanoporous Crystals. *Chemistry of Materials* **26,** 6185–6192. ISSN: 0897-4756 (Nov. 2014).

116. Deem, M. W., Pophale, R., Cheeseman, P. A. & Earl, D. J. Computational Discovery of New Zeolite-Like Materials. *The Journal of Physical Chemistry C* **113,** 21353–21360. ISSN: 1932-7447 (Dec. 2009).

117. Structure Commission of the International Zeolite Association. *Database of Zeolite Structures* 2017. <`http://www.iza-structure.org/databases/`> (visited on 03/14/2019).

118. Martin, R. L. *et al.* In Silico Design of Three-Dimensional Porous Covalent Organic Frameworks via Known Synthesis Routes and Commercially Available Species. *The Journal of Physical Chemistry C* **118,** 23790–23802. ISSN: 1932-7447 (Oct. 2014).

119. Martin, R. L., Simon, C. M., Smit, B. & Haranczyk, M. In silico Design of Porous Polymer Networks: High-Throughput Screening for Methane Storage Materials. *Journal of the American Chemical Society* **136,** 5006–5022. ISSN: 0002-7863 (Apr. 2014).

120. Thornton, A. W. *et al.* Materials Genome in Action: Identifying the Performance Limits of Physical Hydrogen Storage. *Chemistry of Materials* **29,** 2844–2854. ISSN: 0897-4756 (Apr. 2017).

121. Lee, T. B. *et al.* Molecular dynamics simulation study on the hydrogen adsorption and diffusion in non-interpenetrating and interpenetrating IRMOFs. *Catalysis Today* **146,** 216–222. ISSN: 09205861 (Aug. 2009).

122. Fischer, M., Hoffmann, F. & Fröba, M. Preferred Hydrogen Adsorption Sites in Various MOFs-A Comparative Computational Study. *ChemPhysChem* **10,** 2647–2657. ISSN: 14394235 (Oct. 2009).

123. Getman, R. B., Bae, Y.-S., Wilmer, C. E. & Snurr, R. Q. Review and Analysis of Molecular Simulations of Methane, Hydrogen, and Acetylene Storage in Metal-Organic Frameworks. *Chemical Reviews* **112,** 703–723. ISSN: 0009-2665 (Feb. 2012).

124. Basdogan, Y. & Keskin, S. Simulation and modelling of MOFs for hydrogen storage. *CrystEngComm* **17,** 261–275. ISSN: 1466-8033 (2015).

125. Sesé, L. M. Study of the Feynman-Hibbs effective potential against the path-integral formalism for Monte Carlo simulations of quantum many-body Lennard-Jones systems. *Molecular Physics* **81,** 1297–1312. ISSN: 0026-8976 (Apr. 1994).

126. Pantatosaki, E. & Papadopoulos, G. K. On the computation of long-range interactions in fluids under confinement: Application to pore systems with various types of spatial periodicity. *The Journal of Chemical Physics* **127,** 164723. ISSN: 0021-9606 (Oct. 2007).

127. Kumar, A. V. A., Jobic, H. & Bhatia, S. K. Quantum Effects on Adsorption and Diffusion of Hydrogen and Deuterium in Microporous Materials. *The Journal of Physical Chemistry B* **110,** 16666–16671. ISSN: 1520-6106 (Aug. 2006).

128. Tanaka, H., Kanoh, H., Yudasaka, M., Iijima, S. & Kaneko, K. Quantum Effects on Hydrogen Isotope Adsorption on Single-Wall Carbon Nanohorns. *Journal of the American Chemical Society* **127,** 7511–7516. ISSN: 0002-7863 (May 2005).

129. Wang, Q. & Johnson, J. K. Molecular simulation of hydrogen adsorption in single-walled carbon nanotubes and idealized carbon slit pores. *The Journal of Chemical Physics* **110,** 577–586. ISSN: 0021-9606 (Jan. 1999).

130. Jhung, S. H., Yoon, J. W., Lee, J. S. & Chang, J.-S. Low-Temperature Adsorption/Storage of Hydrogen on FAU, MFI, and MOR Zeolites with Various Si/Al Ratios: Effect of Electrostatic Fields and Pore Structures. *Chemistry - A European Journal* **13,** 6502–6507. ISSN: 09476539 (July 2007).

131. Van den Berg, A. W., Bromley, S. T., Wojdel, J. C. & Jansen, J. C. Adsorption isotherms of H_2 in microporous materials with the SOD structure: A grand canonical Monte Carlo study. *Microporous and Mesoporous Materials* **87,** 235–242. ISSN: 13871811 (Jan. 2006).

132. Rahmati, M. & Modarress, H. Grand canonical Monte Carlo simulation of isotherm for hydrogen adsorption on nanoporous siliceous zeolites at room temperature. *Applied Surface Science* **255,** 4773–4778. ISSN: 01694332 (Feb. 2009).

133. Fuchs, A. H. & Cheetham, A. K. Adsorption of Guest Molecules in Zeolitic Materials: Computational Aspects. *The Journal of Physical Chemistry B* **105,** 7375–7383. ISSN: 1520-6106 (Aug. 2001).

134. Smit, B. & Maesen, T. L. M. Commensurate 'freezing' of alkanes in the channels of a zeolite. *Nature* **374,** 42–44. ISSN: 0028-0836 (Mar. 1995).

135. Martin, R. L. *et al.* Similarity-Driven Discovery of Zeolite Materials for Adsorption-Based Separations. *ChemPhysChem* **13,** 3595–3597. ISSN: 14394235 (Nov. 2012).

136. Frost, H., Düren, T. & Snurr, R. Q. Effects of Surface Area, Free Volume, and Heat of Adsorption on Hydrogen Uptake in MetalOrganic Frameworks. *J. Phys. Chem. B* **110,** 9565–9570 (2006).

137. Simon, C. M. *et al.* Optimizing nanoporous materials for gas storage. *Physical Chemistry Chemical Physics* **16,** 5499. ISSN: 1463-9076 (2014).

138. Sculley, J., Yuan, D. & Zhou, H.-C. The current status of hydrogen storage in metal–organic frameworks—updated. *Energy & Environmental Science* **4,** 2721. ISSN: 1754-5692 (2011).

139. Suh, M. P., Park, H. J., Prasad, T. K. & Lim, D.-W. Hydrogen Storage in Metal–Organic Frameworks. *Chemical Reviews* **112,** 782–835. ISSN: 0009-2665 (Feb. 2012).

140. Yang, J., Sudik, A., Wolverton, C. & Siegel, D. J. High capacity hydrogen storage materials: attributes for automotive applications and techniques for materials discovery. *Chem. Soc. Rev.* **39,** 656–675. ISSN: 0306-0012 (2010).

141. Hu, Y. H. & Zhang, L. Hydrogen Storage in Metal-Organic Frameworks. *Advanced Materials* **22,** E117–E130. ISSN: 09359648 (May 2010).

142. Lai, Q. *et al.* Hydrogen Storage Materials for Mobile and Stationary Applications: Current State of the Art. *ChemSusChem* **8,** 2789–2825. ISSN: 18645631 (Sept. 2015).

143. Murray, L. J., Dincă, M. & Long, J. R. Hydrogen storage in metal–organic frameworks. *Chemical Society Reviews* **38,** 1294. ISSN: 0306-0012 (2009).

144. Ibarra, I. A. *et al.* Highly porous and robust scandium-based metal-organic frameworks for hydrogen storage. *Chemical Communications* **47,** 8304. ISSN: 1359-7345 (2011).

145. Yuan, D., Zhao, D., Sun, D. & Zhou, H.-C. An Isoreticular Series of Metal-Organic Frameworks with Dendritic Hexacarboxylate Ligands and Exceptionally High Gas-Uptake Capacity. *Angewandte Chemie International Edition* **49,** 5357–5361. ISSN: 14337851 (June 2010).

146. Park, K. S. *et al.* Exceptional chemical and thermal stability of zeolitic imidazolate frameworks. *Proceedings of the National Academy of Sciences* **103,** 10186–10191. ISSN: 0027-8424 (July 2006).

147. Fairen-Jimenez, D. *et al.* Opening the Gate: Framework Flexibility in ZIF-8 Explored by Experiments and Simulations. *Journal of the American Chemical Society* **133,** 8900–8902. ISSN: 0002-7863 (June 2011).

148. Abrahams, B. F., Hoskins, B. F., Liu, J. & Robson, R. The archetype for a new class of simple extended 3D honeycomb frameworks. The synthesis and x-ray crystal structures of Cd(CN)5/3(OH)1/3.1/3(C6H12N4), Cd(CN)2.1/3(C6H12N4), and Cd(Cn)2.2/3H_2O.tBuOH (C6H12N4 = hexamethylenetetramine) revealing two topologi. *Journal of the American Chemical Society* **113,** 3045–3051. ISSN: 0002-7863 (Apr. 1991).

149. Andrés, R. *et al.* Rational Design of Three-Dimensional (3D) Optically Active Molecule-Based Magnets: Synthesis, Structure, Optical and Magnetic Properties of {[Ru(bpy)3]2+, ClO4-, [Mn II Cr III (ox)3]-}n and {[Ru(bpy)2ppy]+, [M II Cr III (ox)3]-}n. *Inorganic Chemistry* **40,** 4633–4640. ISSN: 0020-1669 (Aug. 2001).

150. Felderhoff, M., Weidenthaler, C., von Helmolt, R. & Eberle, U. Hydrogen storage: the remaining scientific and technological challenges. *Physical Chemistry Chemical Physics* **9,** 2643. ISSN: 1463-9076 (2007).

151. Mazyan, W., Ahmadi, A., Ahmed, H. & Hoorfar, M. Market and technology assessment of natural gas processing: A review. *Journal of Natural Gas Science and Engineering* **30,** 487–514. ISSN: 18755100 (Mar. 2016).

152. Millward, A. R. & Yaghi, O. M. Metal-Organic Frameworks with Exceptionally High Capacity for Storage of Carbon Dioxide at Room Temperature. *Journal of the American Chemical Society* **127,** 17998–17999. ISSN: 0002-7863 (Dec. 2005).

153. Cavenati, S., Grande, C. A., Rodrigues, A. E., Kiener, C. & Müller, U. Metal Organic Framework Adsorbent for Biogas Upgrading. *Industrial & Engineering Chemistry Research* **47,** 6333–6335. ISSN: 0888-5885 (Aug. 2008).

154. Wilmer, C. E., Farha, O. K., Bae, Y.-S., Hupp, J. T. & Snurr, R. Q. Structure–property relationships of porous materials for carbon dioxide separation and capture. *Energy & Environmental Science* **5,** 9849. ISSN: 1754-5692 (2012).

155. Kanoo, P., Gurunatha, K. L. & Maji, T. K. Versatile functionalities in MOFs assembled from the same building units: interplay of structural flexibility, rigidity and regularity. *J. Mater. Chem.* **20,** 1322–1331. ISSN: 0959-9428 (2010).

156. Stylianou, K. C., Bacsa, J., Bradshaw, D. & Rosseinsky, M. J. A 3D Porous Metal Organic Framework Based on Infinite 1D Nickel(II) Chains with Rutile Topology Displaying Open Metal Sites. *Zeitschrift für anorganische und allgemeine Chemie* **640,** 2123–2131. ISSN: 00442313 (Sept. 2014).

157. Zang, S. *et al.* Coexistence of chiral hydrophilic and achiral hydrophobic channels in one multi-helical-array metal–organic framework incorporating helical water cluster chains. *Chem. Commun.* 4997–4999. ISSN: 1359-7345 (2006).

158. Chaudhari, A. K., Mukherjee, S., Nagarkar, S. S., Joarder, B. & Ghosh, S. K. Bi-porous metal–organic framework with hydrophilic and hydrophobic channels: selective gas sorption and reversible iodine uptake studies. *CrystEngComm* **15,** 9465. ISSN: 1466-8033 (2013).

159. Sapchenko, S. A., Samsonenko, D. G., Dybtsev, D. N. & Fedin, V. P. Hierarchical Guest Exchange and Step-by-Step Activation of a Biporous Coordination Framework. *Inorganic Chemistry* **52,** 9702–9704. ISSN: 0020-1669 (Sept. 2013).

160. Ohmori, O., Kawano, M. & Fujita, M. A Two-in-One Crystal: Uptake of Two Different Guests into Two Distinct Channels of a Biporous Coordination Network. *Angewandte Chemie International Edition* **44,** 1962–1964. ISSN: 1433-7851 (Mar. 2005).

161. Abrahams, B. F., Moylan, M., Orchard, S. D. & Robson, R. Zinc Saccharate: A Robust, 3D Coordination Network with Two Types of Isolated, Parallel Channels, One Hydrophilic and the Other Hydrophobic. *Angewandte Chemie* **115,** 1892–1895 (2003).

162. Kawano, M., Kawamichi, T., Haneda, T., Kojima, T. & Fujita, M. The Modular Synthesis of Functional Porous Coordination Networks. *Journal of the American Chemical Society* **129,** 15418–15419. ISSN: 0002-7863 (Dec. 2007).

163. Mohideen, M. I. H. *et al.* Protecting group and switchable pore-discriminating adsorption properties of a hydrophilic–hydrophobic metal–organic framework. *Nature Chemistry* **3,** 304–310. ISSN: 1755-4330 (Apr. 2011).

164. Jiao, J. *et al.* An aminopyrimidine-functionalized cage-based metal-organic framework exhibiting highly selective adsorption of C_2H_2 and CO_2 over CH_4. *Dalton Transactions* **45,** 13373–13382. ISSN: 1477-9226 (2016).

165. Chen, F., Bai, D., Wang, Y., Jiang, D. & He, Y. A family of ssa-type copper-based MOFs constructed from unsymmetrical diisophthalates: synthesis, characterization and selective gas adsorption. *Materials Chemistry Frontiers* **1,** 2283–2291. ISSN: 2052-1537 (2017).

166. Giannozzi, P. *et al.* QUANTUM ESPRESSO: a modular and open-source software project for quantum simulations of materials. *Journal of Physics: Condensed Matter* **21,** 395502. ISSN: 0953-8984 (Sept. 2009).

167. Perdew, J. P., Burke, K. & Ernzerhof, M. Generalized Gradient Approximation Made Simple. *Physical Review Letters* **77,** 3865–3868. ISSN: 0031-9007 (Oct. 1996).

168. Grimme, S. Semiempirical GGA-type density functional constructed with a long-range dispersion correction. *Journal of Computational Chemistry* **27,** 1787–1799. ISSN: 0192-8651 (Nov. 2006).

169. Blöchl, P. E. Projector augmented-wave method. *Physical Review B* **50,** 17953–17979. ISSN: 0163-1829 (Dec. 1994).

170. Sarkisov, L. Molecular simulation of low temperature argon adsorption in several models of IRMOF-1 with defects and structural disorder. *Dalton Transactions* **45,** 4203–4212. ISSN: 1477-9226 (2016).

171. Vasudevan, V. & Mushrif, S. H. Force field parameters for N,N-Dimethylformamide (DMF) revisited: Improved prediction of bulk properties and complete miscibility in water. *Journal of Molecular Liquids* **206,** 338–342. ISSN: 01677322 (June 2015).

172. Wu, X., Huang, J., Cai, W. & Jaroniec, M. Force field for ZIF-8 flexible frameworks: atomistic simulation of adsorption, diffusion of pure gases as CH_4, H_2, CO_2 and N_2. *RSC Adv.* **4,** 16503–16511. ISSN: 2046-2069 (2014).

173. Horn, H. W. *et al.* Development of an improved four-site water model for biomolecular simulations: TIP4P-Ew. *The Journal of Chemical Physics* **120,** 9665–9678. ISSN: 0021-9606 (May 2004).

174. Gładysiak, A. *et al.* Biporous Metal–Organic Framework with Tunable CO_2/CH_4 Separation Performance Facilitated by Intrinsic Flexibility. *ACS Applied Materials & Interfaces* **10,** 36144–36156. ISSN: 1944-8244 (Oct. 2018).

175. Spek, A. L. PLATON SQUEEZE: a tool for the calculation of the disordered solvent contribution to the calculated structure factors. *Acta Crystallographica Section C Structural Chemistry* **71,** 9–18. ISSN: 2053-2296 (Jan. 2015).

176. Nye, J. F. & Lindsay, R. B. Physical Properties of Crystals: Their Representation by Tensors and Matrices. *Physics Today* **10,** 26–26. ISSN: 0031-9228 (Dec. 1957).

177. Rogge, S. M. J., Waroquier, M. & Van Speybroeck, V. Reliably Modeling the Mechanical Stability of Rigid and Flexible Metal–Organic Frameworks. *Accounts of Chemical Research* **51,** 138–148. ISSN: 0001-4842 (Jan. 2018).

178. Mason, J. A. *et al.* Methane storage in flexible metal–organic frameworks with intrinsic thermal management. *Nature* **527,** 357–361. ISSN: 0028-0836 (Nov. 2015).

179. Serre, C. *et al.* An Explanation for the Very Large Breathing Effect of a Metal–Organic Framework during CO_2 Adsorption. *Advanced Materials* **19,** 2246–2251. ISSN: 09359648 (Sept. 2007).

180. Addicoat, M. A., Vankova, N., Akter, I. F. & Heine, T. Extension of the Universal Force Field to Metal–Organic Frameworks. *Journal of Chemical Theory and Computation* **10,** 880–891. ISSN: 1549-9618 (Feb. 2014).

181. Yazaydın, A. Ö. *et al.* Screening of MetalOrganic Frameworks for Carbon Dioxide Capture from Flue Gas Using a Combined Experimental and Modeling Approach. *Journal of the American Chemical Society* **131,** 18198–18199. ISSN: 0002-7863 (Dec. 2009).

182. Kim, J., Lin, L.-C., Lee, K., Neaton, J. B. & Smit, B. Efficient Determination of Accurate Force Fields for Porous Materials Using ab Initio Total Energy Calculations. *The Journal of Physical Chemistry C* **118,** 2693–2701. ISSN: 1932-7447 (Feb. 2014).

183. Serra-Crespo, P., Ramos-Fernandez, E. V., Gascon, J. & Kapteijn, F. Synthesis and Characterization of an Amino Functionalized MIL-101(Al): Separation and Catalytic Properties. *Chemistry of Materials* **23,** 2565–2572. ISSN: 0897-4756 (May 2011).

184. Couck, S. *et al.* Adsorption and Separation of Light Gases on an Amino-Functionalized Metal-Organic Framework: An Adsorption and In Situ XRD Study. *ChemSusChem* **5,** 740–750. ISSN: 18645631 (Apr. 2012).

185. Giménez-Marqués, M. *et al.* Gas confinement in compartmentalized coordination polymers for highly selective sorption. *Chemical Science* **8,** 3109–3120. ISSN: 2041-6520 (2017).

186. Bastin, L. *et al.* A Microporous MetalOrganic Framework for Separation of CO_2/N_2 and CO_2/CH_4 by Fixed-Bed Adsorption. *The Journal of Physical Chemistry C* **112,** 1575–1581. ISSN: 1932-7447 (Feb. 2008).

187. Xian, S. *et al.* Highly enhanced and weakened adsorption properties of two MOFs by water vapor for separation of CO_2/CH_4 and CO_2/N_2 binary mixtures. *Chemical Engineering Journal* **270,** 385–392. ISSN: 13858947 (June 2015).

188. Nugent, P. *et al.* Porous materials with optimal adsorption thermodynamics and kinetics for CO_2 separation. *Nature* **495,** 80–84. ISSN: 0028-0836 (Mar. 2013).

189. Lee, Y.-R., Kim, J. & Ahn, W.-S. Synthesis of metal-organic frameworks: A mini review. *Korean Journal of Chemical Engineering* **30,** 1667–1680. ISSN: 0256-1115 (Sept. 2013).

190. Howarth, A. J. *et al.* Best Practices for the Synthesis, Activation, and Characterization of Metal-Organic Frameworks. *Chemistry of Materials* **29,** 26–39. ISSN: 0897-4756 (Jan. 2017).

191. Rosi, N. L. *et al.* Rod Packings and MetalOrganic Frameworks Constructed from Rod-Shaped Secondary Building Units. *Journal of the American Chemical Society* **127,** 1504–1518. ISSN: 0002-7863 (Feb. 2005).

192. McDonald, T. M. *et al.* Capture of Carbon Dioxide from Air and Flue Gas in the Alkylamine-Appended Metal-Organic Framework mmen-Mg 2 (dobpdc). *Journal of the American Chemical Society* **134,** 7056–7065. ISSN: 0002-7863 (Apr. 2012).

193. Bae, T.-H. & Long, J. R. CO_2/N_2 separations with mixed-matrix membranes containing Mg2(dobdc) nanocrystals. *Energy & Environmental Science* **6,** 3565. ISSN: 1754-5692 (2013).

194. Van Vleet, M. J., Weng, T., Li, X. & Schmidt, J. In Situ, Time-Resolved, and Mechanistic Studies of Metal–Organic Framework Nucleation and Growth. *Chemical Reviews* **118,** 3681–3721. ISSN: 0009-2665 (Apr. 2018).

195. Rimer, J. D. & Tsapatsis, M. Nucleation of open framework materials: Navigating the voids. *MRS Bulletin* **41,** 393–398. ISSN: 0883-7694 (May 2016).

196. Hermes, S. *et al.* Trapping Metal-Organic Framework Nanocrystals: An in-Situ Time-Resolved Light Scattering Study on the Crystal Growth of MOF-5 in Solution. *Journal of the American Chemical Society* **129,** 5324–5325. ISSN: 0002-7863 (May 2007).

197. McKinstry, C., Cussen, E. J., Fletcher, A. J., Patwardhan, S. V. & Sefcik, J. Effect of Synthesis Conditions on Formation Pathways of Metal Organic Framework (MOF-5) Crystals. *Crystal Growth & Design* **13,** 5481–5486. ISSN: 1528-7483 (Dec. 2013).

198. Goesten, M. G. *et al.* Molecular Promoting of Aluminum Metal-Organic Framework Topology MIL-101 by N , N -Dimethylformamide. *Inorganic Chemistry* **53,** 882–887. ISSN: 0020-1669 (Jan. 2014).

199. Yang, X. & Clark, A. E. Preferential Solvation of Metastable Phases Relevant to Topological Control Within the Synthesis of Metal–Organic Frameworks. *Inorganic Chemistry* **53,** 8930–8940. ISSN: 0020-1669 (Sept. 2014).

200. Amirjalayer, S., Tafipolsky, M. & Schmid, R. Surface Termination of the Metal-Organic Framework HKUST-1: A Theoretical Investigation. *The Journal of Physical Chemistry Letters* **5,** 3206–3210. ISSN: 1948-7185 (Sept. 2014).

201. Anderson, M. W. *et al.* Predicting crystal growth via a unified kinetic three-dimensional partition model. *Nature* **544,** 456–459. ISSN: 0028-0836 (Apr. 2017).

202. Cantu, D. C., McGrail, B. P. & Glezakou, V.-A. Formation Mechanism of the Secondary Building Unit in a Chromium Terephthalate Metal–Organic Framework. *Chemistry of Materials* **26,** 6401–6409. ISSN: 0897-4756 (Nov. 2014).

203. Umemura, A. *et al.* Morphology Design of Porous Coordination Polymer Crystals by Coordination Modulation. *Journal of the American Chemical Society* **133,** 15506–15513. ISSN: 0002-7863 (Oct. 2011).

204. Sear, R. P. The non-classical nucleation of crystals: microscopic mechanisms and applications to molecular crystals, ice and calcium carbonate. *International Materials Reviews* **57,** 328–356. ISSN: 0950-6608 (Nov. 2012).

205. Whitelam, S. & Jack, R. L. The Statistical Mechanics of Dynamic Pathways to Self-Assembly. *Annual Review of Physical Chemistry* **66,** 143–163. ISSN: 0066-426X (Apr. 2015).

206. Valeriani, C., Sanz, E. & Frenkel, D. Rate of homogeneous crystal nucleation in molten NaCl. *The Journal of Chemical Physics* **122,** 194501. ISSN: 0021-9606 (May 2005).

207. Zhang, F., Zocher, G., Sauter, A., Stehle, T. & Schreiber, F. Novel approach to controlled protein crystallization through ligandation of yttrium cations. *Journal of Applied Crystallography* **44,** 755–762. ISSN: 0021-8898 (Aug. 2011).

208. Lu, P. J. *et al.* Gelation of particles with short-range attraction. *Nature* **453,** 499–503. ISSN: 0028-0836 (May 2008).

209. Meakin, P. Formation of Fractal Clusters and Networks by Irreversible Diffusion-Limited Aggregation. *Physical Review Letters* **51,** 1119–1122. ISSN: 0031-9007 (Sept. 1983).

210. Weeks, J. D., Gilmer, G. H. & Jackson, K. A. Analytical theory of crystal growth. *The Journal of Chemical Physics* **65,** 712–720. ISSN: 0021-9606 (July 1976).

211. Stauffer, D., Coniglio, A. & Heermann, D. W. Monte Carlo Experiment for Nucleation Rate in the Three-Dimensional Ising Model. *Physical Review Letters* **49,** 1299–1302. ISSN: 0031-9007 (Nov. 1982).

212. Acharyya, M. & Stauffer, D. Nucleation and hysteresis in Ising model: classical theory versus computer simulation. *The European Physical Journal B* **5,** 571–575. ISSN: 1434-6028 (Oct. 1998).

213. Brendel, K., Barkema, G. T. & van Beijeren, H. Nucleation times in the two-dimensional Ising model. *Physical Review E* **71,** 031601. ISSN: 1539-3755 (Mar. 2005).

214. Pan, A. C. & Chandler, D. Dynamics of Nucleation in the Ising Model. *The Journal of Physical Chemistry B* **108,** 19681–19686. ISSN: 1520-6106 (Dec. 2004).

215. Hedges, L. O. & Whitelam, S. Patterning a surface so as to speed nucleation from solution. *Soft Matter* **8,** 8624. ISSN: 1744-683X (2012).

216. Ferrenberg, A. M. & Swendsen, R. H. Optimized Monte Carlo data analysis. *Physical Review Letters* **63,** 1195–1198. ISSN: 0031-9007 (Sept. 1989).

217. Sonsin, A. F., Cortes, M. R., Nunes, D. R., Gomes, J. V. & Costa, R. S. Computational Analysis of 3D Ising Model Using Metropolis Algorithms. *Journal of Physics: Conference Series* **630,** 012057. ISSN: 1742-6588 (July 2015).

218. Heuer, H.-O. Critical dynamics of the three-dimensional Ising model: A Monte Carlo study. *Journal of Statistical Physics* **72,** 789–827. ISSN: 0022-4715 (Aug. 1993).

219. Oxtoby, D. W. Nucleation of First-Order Phase Transitions. *Accounts of Chemical Research* **31,** 91–97. ISSN: 0001-4842 (Feb. 1998).

220. Onsager, L. Crystal Statistics. I. A Two-Dimensional Model with an Order-Disorder Transition. *Physical Review* **65,** 117–149. ISSN: 0031-899X (Feb. 1944).

221. Fisher, M. E. & Ferdinand, A. E. Interfacial, Boundary, and Size Effects at Critical Points. *Physical Review Letters* **19,** 169–172. ISSN: 0031-9007 (July 1967).

222. Lee, G.-Y. *et al.* Amine-Functionalized Covalent Organic Framework for Efficient SO_2 Capture with High Reversibility. *Scientific Reports* **7,** 557. ISSN: 2045-2322 (Dec. 2017).

223. Romero, J. *et al.* Metal-functionalized covalent organic frameworks as precursors of supercapacitive porous N-doped graphene. *Journal of Materials Chemistry A* **5,** 4343–4351. ISSN: 2050-7488 (2017).

224. Borboudakis, G. *et al.* Author Correction: Chemically intuited, large-scale screening of MOFs by machine learning techniques. *npj Computational Materials* **3,** 47. ISSN: 2057-3960 (Dec. 2017).

225. Boyd, P. G., Lee, Y. & Smit, B. Computational development of the nanoporous materials genome. *Nature Reviews Materials* **2,** 17037. ISSN: 2058-8437 (July 2017).

226. Evans, J. D. & Coudert, F.-X. Predicting the Mechanical Properties of Zeolite Frameworks by Machine Learning. *Chemistry of Materials* **29,** 7833–7839. ISSN: 0897-4756 (Sept. 2017).

227. Karthika, S., Radhakrishnan, T. K. & Kalaichelvi, P. A Review of Classical and Nonclassical Nucleation Theories. *Crystal Growth & Design* **16,** 6663–6681. ISSN: 1528-7483 (Nov. 2016).